UNIVERSITÀ DEGLI STUDI DI PAVIA
DOTTORATO DI RICERCA IN FISICA – XXIX CICLO

Light scattering in Disordered Textures with Self-Similarity and High Aspect-Ratio

Salvatore Del Sorbo

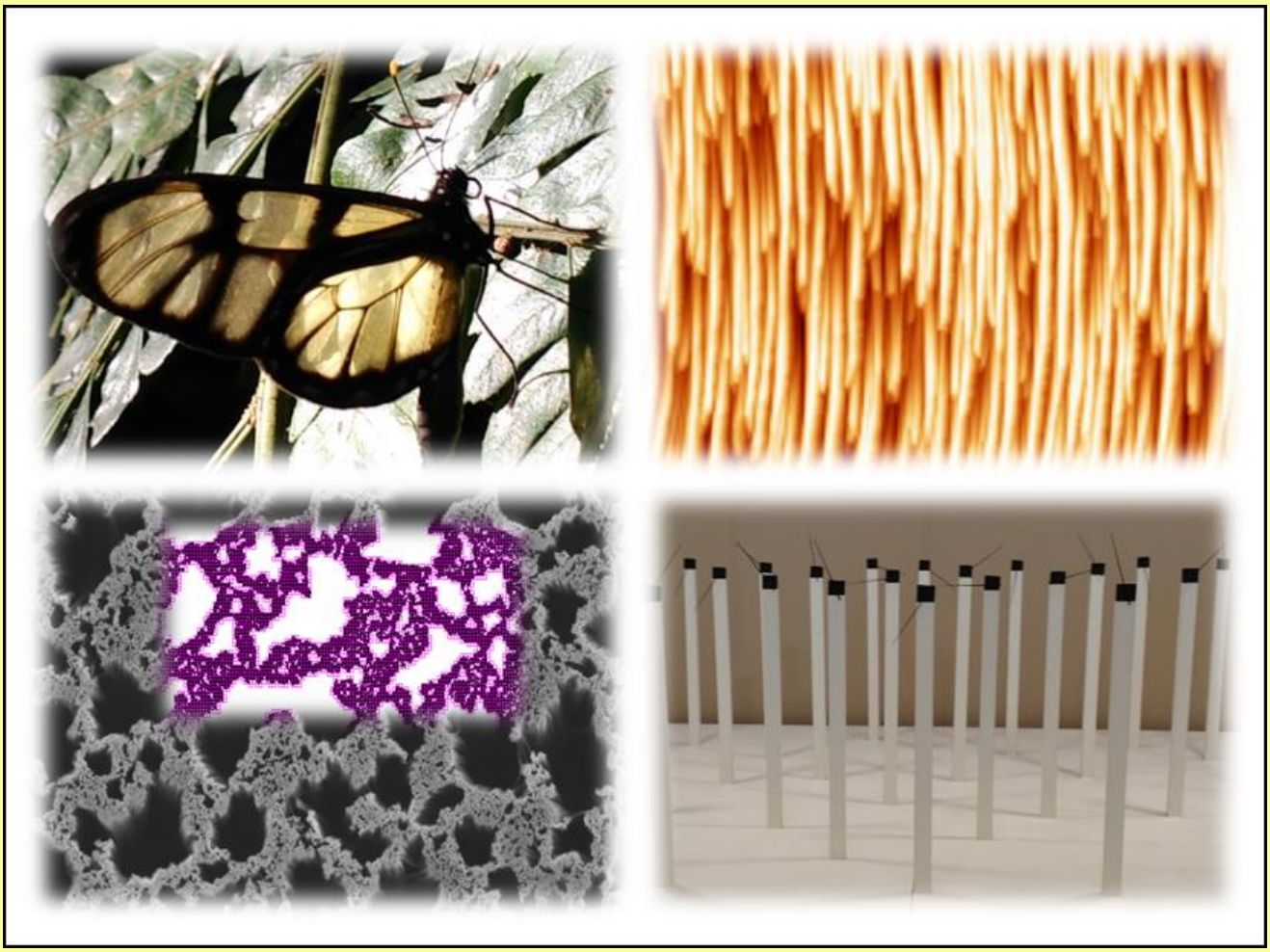

Tesi per il conseguimento del titolo

Università degli Studi di Pavia
Dipartimento di Fisica

DOTTORATO DI RICERCA IN FISICA – XXIX CICLO

Light scattering in Disordered Textures with Self-Similarity and High Aspect-Ratio

Salvatore Del Sorbo

Submitted to the Graduate School of Physics in partial fulfillment of the requirements for the degree of

DOTTORE DI RICERCA IN FISICA

DOCTOR OF PHILOSOPHY IN PHYSICS

at the

University of Pavia

Supervisors: Prof. Lucio Claudio Andreani
Prof. Matteo Galli

Cover:
Top-left, picture of a glasswing butterfly (*Greta oto*).
Top-right, AFM image of a borosilicate glass nanostructured by defocused ion beam sputtering.
Bottom-left, SEM image of a silicon nanowires random array.
Bottom-right, picture of *Potent Impotency* by Ivan Kafka (Czech artist).

Light scattering in Disordered Textures with Self-Similarity and High Aspect-Ratio

Salvatore Del Sorbo
PhD thesis - University of Pavia
Pavia, Italy, November 2017

Dedico questo traguardo, sommo coronamento del percorso d'istruzione,
ai *miei familiari*, che hanno sempre creduto in me,
ai *docenti*, tutti, che hanno ispirato il mio impegno,
a *Emilia*, con la quale ho condiviso la forza di questi anni.

Salvatore

Contents

Chapter 1

Introduction

The target of this Ph.D. thesis is the study of *light scattering* and *light trapping* in complex photonic structures. To this purpose, the new phenomena emerging from the optical investigation of fabricated structures have been interpreted by the theoretical frame of multiple-scattering of light. These issues are important for the understanding of general properties of light propagation and light-matter interaction, and for developing structures that are suitable for the harvesting of light in photovoltaic (PV) devices. Thus, the present work has both fundamental and application-oriented aspects.

This chapter illustrate the general overview of the thesis. In the first section we describe the interest for studying light scattering in disordered media. Moreover, we discuss fundamental problems of coherence and localization effects in disordered photonic structures. In the second section we discuss the organization of the topics in the next chapters.

1.1 General overview

In the last decades, the interest for light scattering in complex structure has increased rapidly, together with the development of photonics as a new branch of applied optics [1, 2, 3, 4, 5, 6]. Nowadays, computer simulations for the design of increasingly complex photonic structures allow to reach very high performances both for optical mode coupling between different materials and for enhanced light-matter interaction related to the confinement of light [7, 8]. On the other hand, unavoidable fabrication defects limit the efficiency of

photonic structures [9, 10, 11, 12, 13]. This becomes a real impediment to large scale applications, because fabrication costs do not allow to realize elaborate wavelength-scale architectures with the same quality that is achievable at laboratory scale [14, 15].

A crucial research area from this point of view is the implementation of photonic solutions in PV devices. In fact, the simultaneous requirements to achieve a complete harvesting of sunlight and to use the minimum amount of absorber material in fabrication processes lead to hard technological challenges. In all PV technologies considered so far, the main challenge is to increase the light harvesting and the overall conversion efficiency, while reducing the fabrication costs [16].

The studies shown in this thesis originate from the aforementioned considerations and focus the attention on photonic structures suitable to enhance light-trapping in thin-film silicon solar cells (SCs). During the evolution of this research field, the different solutions proposed by the scientific community were based on two different approaches [5], i.e. the diffractive coupling or the diffusive scattering [17]. The first solution is achieved by means of ordered photonic structures [18, 19, 20]. These photonic crystals couple efficiently the external radiation into the SC, but the few modes that are activated by a diffraction resonance [21, 22] are not sufficient to cover the whole spectrum of interest. The second approach requires simply a random disordered texture, which typically results from the native morphology of deposited thin layers (as in the case of a rough transparent electrode) or from the chemical/physical erosion of the SC surface [23]. The random surface roughness scatters sunlight incoherently over a broad spectrum [24, 25], however the optical coupling may be weak if the level of roughness is not high enough.

In the last years both theoretical and experimental evidences suggest that the best results in light-trapping for SCs are achieved by combining the two approaches [22, 26, 27, 28]. Actually, aperiodic structures and spatially-correlated roughness scatter sunlight more efficiently than strictly periodic or fully random textures. An aperiodic structure is realized by avoiding a regular repetition in ordering dielectric elements. The lack of a periodic lattice increases the number of coupled modes but makes the fabrications process more difficult [29]. On the other hand, the realization of a spatially-correlated randomness is

quite natural in self-organized processes, which are driven by thermodynamic forces [30]. This is the case of clusters formation by thin-film deposition of a metal. Moreover, disorder-based structures show optical properties that are very stable against fabrication defects [6, 31].

The presence of spatially-correlated features in the disordered texture allows the occurrence of coherent light scattering from the diffusive one. The result is an enhancement of light scattering, which could even lead to light localization. The study of light propagation in such systems has to consider the mechanisms for multiple scattering of the electromagnetic waves [32]. The investigation of these scattering mechanisms elucidates the various regimes for light propagation and helps understanding the basic properties of the interaction between light and complex dielectric media.

1.2 Goal of the thesis

The samples investigated in this thesis are: **(1)** a rough glass substrate for the growth of thin-film SCs; **(2)** a forest of silicon nanowires (NWs). In both of them, light scattering is enhanced by the high aspect ratio of the random texture, whose correlation lengths at the wavelength scale result in the coexistence of diffusive and coherent scattering of light.

The topics dealt with in this thesis are organized as follows:

- In the second chapter, the scattering theory of light is introduced with particular attention to multiple scattering theory and to localization effects. We give the theoretical instruments to understand the phenomenology of wave scattering in turbid media. The phenomenon of weak localization of light in disordered media is explained and is put in relation with the observation of Coherent Back-Scattering (CBS) of light. We introduce the theoretical formalism of average Green's propagator and the concept of bi-static coefficient to explain the enhancement factor of CBS.

- The third chapter contains the description of experimental techniques used for this research activity to perform optical investigation of the proposed textures. Since the main goal is to look for evidences of photon

scattering events which increase the optical path along a thin layer, we perform optical characterization of the samples by means of total transmission and reflection spectroscopy and by the angular intensity distribution of scattered light, also called angle-resolved scattering (ARS). These two techniques are basic research methods for light scattering investigations and they are commonly used in the field of photovoltaics. Moreover, we investigate the coherent features of light propagation of silicon NW samples by means of coherent back-scattering of light. The home-made apparatus employed to perform ARS and CBS measurements is described in detail.

- The fourth chapter reports on the investigations of light-scattering properties of a self-assembled nanotexture fabricated by defocused ion-beam sputtering at the University of Genova. The experimental characterizations of the diffused light measured in transmission are shown. We compare the results obtained for our nanotexture with those from the Asahi-U glass, which is a fabrication standard of growth substrates for thin-film silicon SCs. We discuss the features arising from angle-resolved scattering, linking them to the statistical properties of the morphology of the nanotexture, which exhibits both a random roughness and pseudo-periodic patterns.

- In the fifth chapter, we present the anti-reflection properties of ultra-thin and vertically aligned silicon NWs arranged in dense 2D fractal arrays. These NW samples were produced at the CNR-IMM institute in Catania and Messina. We investigate the absorbance of these Si NW forests across the entire visible and near-IR range. Very low values of total reflectance are measured. We relate the remarkable optical properties of NW forest to the randomness in the fractal structure, whose refractive index fluctuations trap the photons by strong in-plane multiple scattering.

- Coherent back-scattering experiments performed on the silicon NW forest are reported in the sixth chapter. We characterize the strength of light scattering by fitting the CBS data with a theoretical model. Experimental evidences of far-field coherence are found in the angular-dependence of backscattering enhancement for Raman light. We in-

terpret these results within a simple model of mixed Rayleigh-Raman random walks. Moreover, an original theoretical model - developed in collaboration with the University of Florence - that accounts for CBS dephasing of the Raman signal is shown. Finally, this new theoretical model is validated by extrapolating the Stokes shift of Raman light from data-analysis.

- In the last chapter we summarize the main results of the thesis and conclude the work by discussing the prospects for further investigations.

Chapter 2

Light scattering in nanostructures

The study of light scattering in optical nanostructures is of great interest, because of the enhancement of optical phenomena arising from light-matter interaction. In general, light-matter interaction can cause both elastic and inelastic scattering as well as absorption of radiation. The latter simply reduces the intensity of light along its path. The *elastic scattering* alters the propagation direction leaving the energy of photons unchanged. The *inelastic scattering* changes both the propagation direction and the wave frequency, as in the case of *Raman scattering*. The coexistence of both nanometric and micrometric features in nanostructures is the cause of an intensive scattering of light at the wavelength scale. The radiation may preserve a strong coherence even after many scattering events.

The effects of coherent scattering of light emerge clearly in a photonic crystal with defects. In fact, an ideal photonic crystal is an ordered arrangement of dielectric elements where the light propagates only in electromagnetic eigenmodes, which are determined theoretically by solving Maxwell equations in the periodic lattice. This periodicity causes the absence of modes in some regions of the energy-wavevector space. These regions are known as *photonic bandgaps* (PBGs) [3, 4, 33]. The presence of local defects in the dielectric periodicity may introduce local electromagnetic modes inside the PBG. In these local modes, the light is spatially confined like in a cavity [34]. However, if the number of defects increases too much the phenomenon of light localization in

the ordered structure can get lost, because the optical losses prevail over the enhancement. On the other hand, coherent scattering of light can lead to a confined electromagnetic field in a totally disordered structure. In agreement with Anderson's localization theory, a very intense wave scattering caused by disorder produces non-propagating waves [35]. More precisely, wave localization can happen when the average distance between two consecutive scattering events is comparable with the wavelength [32].

The textures studied here for this purpose are disordered and endowed with high aspect ratio (see sections 4.2 and 5.1). In these structures, light scattering takes place at all length scales. Therefore we recall in this chapter the light scattering theory that is required in order to interpret the fascinating optical phenomena observed on our experiments.

2.1 Elastic scattering of light

The elastic scattering of light is generically distinguished by the relation between the involved length scales, i.e., the wavelength of light λ and the size of the obstacle (scatterer) a the light scatters on. Usually, light scattering is described by means of the *scattering cross section* σ defined via the ratio of scattered power P_s over the incident intensity I_0. When the light scatters on a macroscopic obstacle (i.e., in the limit $\lambda \ll a$), the scattering is a simple refraction or specular reflection and ray-optics theory is sufficient to describe light propagation by means of *Snell law* and the *Fresnel equations* [36]. In the opposite limit $\lambda \gg a$, elastic scattering of light is well described by *Rayleigh theory*, which explains the λ^{-4} trend in strength of light scattering[1] In the intermediate regime, the *Mie theory* describes rigorously the scattering problem of light in the case $\lambda \sim a$ [37, 38].

Since a small dielectric particle spreads the incident light over all directions, the scattering event is describe by means of *differential scattering cross section*

[1]Rayleigh scattering accounts for the blue colour of sky in sunny days. In fact the scattering by air particles is greater for shorter wavelengths of the visible spectrum, which become widely diffused in all directions. On the other hand the longer wavelengths (corresponding to warm colors) propagate longer into the atmosphere without an appreciable scattering. This is also the explanation for the red colour of sunset.

$$\frac{d\sigma}{d\Omega}(\vec{k}_0, \vec{\epsilon}_0; \vec{k}, \vec{\epsilon}) = \frac{r^2 I_s(\vec{k}, \vec{\epsilon})}{I_0(\vec{k}_0, \vec{\epsilon}_0)}, \tag{2.1}$$

where $\vec{\epsilon}_0$, $\vec{\epsilon}$ and $\vec{k}_0$, $\vec{k}$ are the polarization vector and the wave vector, respectively, of the incident and of the scattered radiation. The latter have a modulus defined by the relation $k = 2\pi/\lambda$ and are oriented as the Poynting unitary vector $\vec{n}$. The differential scattering cross section has dimensions of area per unit solid angle and represents the power radiated in the direction $\vec{k}$ with polarization $\vec{\epsilon}$, per unit solid angle, per unit incident flux (power per unit area) in the direction $\vec{k}_0$ with polarization $\vec{\epsilon}_0$ [39]. The *total scattering cross section* is obtained by integrating the equation 2.1 on the whole solid angle.

The calculation of the explicit form of equation 2.1 can be done in a standard way by the Mie theory. However, the Mie theory reduces to the Rayleigh scattering by using the *Born approximation* in the limit $\lambda \gg a$ [39]. Therefore the equation 2.1 becomes

$$\frac{d\sigma}{d\Omega}(\theta) = \frac{k^4 a^6}{2} \left|\frac{\epsilon_r - 1}{\epsilon_r + 2}\right|^2 \left(1 + \cos^2\theta\right), \tag{2.2}$$

where we have considered a single dielectric sphere with $\mu_r = 1$ and isotropic dielectric constant ϵ_r. The angle θ is the *scattering angle* formed by $\vec{k}$ with $\vec{k}_0$, while the factor $(1 + \cos^2\theta)$ comes from the summation over the scattered polarizations[2].

Now we consider the scattering from a system of small scatterers equal to the aforementioned dielectric particle and separated by a fixed length. The incident radiation induces the same dipole on each of the small scatterers, which, therefore, scatter the radiative field with the same strength. Since the field scattered by the j-th scatterer has a phase factor $e^{i\vec{q}\cdot\vec{x}_j}$ depending on the position $\vec{x}_j$ and on the exchange scattering momentum $\vec{q} = (\vec{k}_0 - \vec{k})$, the scattered light results from the coherent superposition of the individual scattered fields. In this case, the scattering cross section is generally the product of the cross section for a single particle (equation 2.2) times the square modulus of

[2]Actually θ comes from the scalar product between $\vec{\epsilon}$ and $\vec{\epsilon}_0$, i.e. the polarization vectors of the scattered and of the incident radiation, respectively.

the summation of phase factors $\Gamma(\vec{q}) = \left|\sum_j e^{i\vec{q}\cdot\vec{x}_j}\right|^2$. The dependence of scattered field on the spatial positions of scatterers becomes explicit by rewriting $\Gamma(\vec{q})$ in the form

$$\Gamma(\vec{q}) = \sum_j \sum_{j'} e^{i\vec{q}\cdot\left(\vec{x}_j - \vec{x}_{j'}\right)}. \tag{2.3}$$

The equation 2.3 carries the information about the spatial distribution of scatterers and, for this reason, it is named the *structure factor*. Notice that the terms with $j \neq j'$ give a considerable contribution only if the array of dielectric particles exhibits structural correlations (i.e., if the scatterers are numerous and ordered in the space). In this case the structure factor gives a significant contribution only in the forward direction ($\vec{k} = \vec{k}_0$), or possibly in the directions of diffracted beams that are determined by constructive interference of all terms. On the contrary, if the scatterers are randomly distributed, only the terms with $j = j'$ are relevant and the value of Γ reduce to total number of the scatterers N with no angular dependence. So the scattering cross section of many scatterers is just N times the scattering cross section of a single one. In this case, the scattering is like an incoherent superposition of individual contributions and is simply called *incoherent scattering*. In this treatment we follow Ref. [39] and we are neglecting up to now the effects of multiple scattering, which we discuss in Sec. 2.3.

2.2 Scattering from a rough surface

The goal of studying light-trapping in this work is to achieve the highest concentration of incoming radiation into a physically thin region. By this latter expression we mean a space region whose size is comparable with the wavelength of incident radiation, but smaller than the characteristic length scale of light-matter interaction. A disordered nanotexture endowed with high aspect-ratio features (like a rough surface) could be suitable for this purpose. In fact the features of a rough dielectric surface scatter the light at all relative length scales, enabling the coexistence of anti-reflection effects and of diffractive and diffusive scattering. The light-scattering properties of a texture are usually related to the *lateral correlation length* and the *root-mean-square* (RMS) vari-

ation of roughness, which are the two statistical parameters describing the *height distribution* of the surface features.

The lateral correlation length describes statistically the periodicity of the texture, or anyway its spatial correlation along the surface plane. In fact, the correlation length is easy to observe in the height profile of an ordered structure (like for photonic crystal textures), which are made of a periodic repetition of a unit cell profile. However for a texture made by roughness, the height profile $h(x)$ looks as a random repetition of features, which are different from each other. In this case, information on the spatial profile of the texture comes from the spectral analysis of the height profile in the reciprocal space. The latter is given by the Fourier series representation of the height profile of the texture, whose dependence on the position takes the form

$$h(x) = \sum_{m=-N}^{N} h_m \exp\left(\frac{2\pi i x}{T_m}\right). \tag{2.4}$$

where x represents the coordinate along the texture profile, $T_m = T_0/m$ (with m belongs to the range $[-N, N]$) are the spatial wavelengths of Fourier harmonics, T_0 is the length of unidimensional profile of texture, and h_m are the strengths of the corresponding spatial harmonics [40]. We defer the definition of the lateral correlation length to section 4.2, where we shall give its explicit form from the operational definition. We limit ourselves here to the form of the RMS roughness, because it is the most important parameter used to evaluate the specular reflectance and transmittance in scalar scattering theory [40, 41, 42]. The RMS of roughness is commonly indicated with σ_r and is strictly related to the intensities of the Fourier harmonics h_m:

$$\sigma^2 = \sum_{n=-N}^{N} |h_m|^2 . \tag{2.5}$$

Notice that the value of RMS roughness could depend on the range of spatial wavelengths T_m we consider in the analysis of the height profile. On the other hand, the relative length scale $T_m \cdot k$ (where k is the wavevector of incident radiation) determines the mechanism of light scattering as discussed in section 2.1. For these reasons we treat separately the elastic scattering of light due to

a small-scale RMS roughness and a long-scale one.

The small-scale RMS roughness σ_s is calculated from the equation 2.5 taking into account only the contributions of the short Fourier harmonics, i.e., those having a spatial wavelength $T_m < \lambda$ [40]. This small-scale roughness enhances the coupling of the incident light into the substrate, as it makes the dielectric constant variate on a sub-wavelength scale. To explain this, we start by considering a value $\sigma_s \ll \lambda$. In this case there is an enhancement of scattered light in the forward direction as a result by Rayleigh theory (see final comments of section 2.1). On the other hand a value of $\sigma_s \simeq \lambda$ indicates a roughness that is high enough to behave optically as an intermediate layer between the two media. In this layer we can define an *effective refractive index* n_{eff} as follows:

$$n_{eff} = \sqrt{\phi n_{sub}^2 + (1-\phi) n_{air}^2}, \tag{2.6}$$

where ϕ is the *fill factor* of the roughness (i.e., the fraction of substrate material in the texture), while $(1-\phi)$ is the fraction of air. Since $n_{air} < n_{eff} < n_{sub}$, the presence of roughness smoothens the transition between the two refractive indices, and, therefore, the optical losses due to Fresnel reflection decreases. Moreover, if the width of the texture protrusions is not constant but decreases with the height (as for instance in a conical shape), the fill factor becomes a function of the texture hight $\phi(z)$. Therefore the value of refractive index changes gradually along the z direction of the textured layer. In this case the roughness works as an *optical impedance matching layer* between air and substrate, which makes Fresnel reflection vanish [40, 43]. In the natural world, similar morphologies confer some insect organs transparency and broadband anti-reflection functionality, as observed in the corneas of nocturnal moths [44]. On the contrary the evaluation of equation 2.5 based on the Fourier harmonics with long spatial period ($T_m > \lambda$) returns the value of the long-scale RMS σ_l. In other words, the value of σ_l concerns the long-scale periodicity of the texture. We want to highlight the role of Fourier harmonics with $T_m > \lambda$ for the coherent coupling of incident radiation in the texture: the larger σ_l, the stronger the scattering of light. Diffraction processes scatter the incident light at large scattering angles into the substrate, increasing the optical path at a

fixed thickness of the substrate. This appears as a reduction of both specular reflectance and specular transmittance, while the light diffused off the incident direction increases.

The above qualitative discussion about the role of RMS roughness in the scattering of light can be related to the results of the calculation of reflection (r) and transmission (t) coefficients by applying the electrodynamic theory. In fact the separation of roughness contributions according to short-scale and long-scale components allows to write the expressions of r and t, respectively, in the form [40]

$$\begin{cases} r = r_0(1 - 2k^2 n_1 n_2 \sigma_s^2) \\ t = t_0[1 + 0.5k^2(n_1 - n_2)^2 \sigma_s^2] \end{cases} \tag{2.7}$$

$$\begin{cases} r = r_0(1 - 2k^2 n_1 \sigma_l^2) \\ t = t_0[1 - 0.5k^2(n_1 - n_2)^2 \sigma_l^2] \end{cases} \tag{2.8}$$

where r_0 and t_0 are the amplitudes of Fresnel reflection and transmission coefficients, n_1 and n_2 are the refractive index of air and substrate, respectively.

The above discussion motivates the need for both short-scale and large-scale surface corrugations in the texture in order to achieve an effective scheme of light trapping.

2.3 Multiple scattering of light

The light scattered off a textured material with $h_m \geq \lambda$ has non-negligible probability to be scattered several times before leaving the material, since each scattering event randomizes the direction of light propagation. Therefore, the proper description of elastic light scattering on deep textures requires the theory of *multiple scattering* of light. The latter is typically used to treat the light propagation into turbid media, i.e. when the light propagates within a collection of transparent (or weakly absorbing) scatterers. Common examples of turbid media are dispersions of colloidal particles in a liquid or the water drops in the dense fog.

The relevance of multiple light scattering depends on the average distance between two scatterers, which is usually called the *mean free path* l^*. The classical ray propagation takes places for $\lambda \ll l^*$. On the other hand, when the scattering is weak and $\lambda \gg l^*$, the disordered medium appears as a homogeneous effective medium. However, over long distances (on the scale of many l^*) the scattering effect accumulates and the wave propagation direction can still be significantly randomized. For the case of $\lambda \leq l^*$, the effective medium approximation is no longer valid and the propagating waves rapidly loses the correlation with the incident direction after some scattering events. Therefore, because of multiple scattering the wave path results in a random walk [45], which is characterized by a mean-square displacement

$$\left\langle \Delta r^2 \right\rangle = \sum_{i=1}^{d} \left\langle x_i^2 \right\rangle, \tag{2.9}$$

where d is the system dimensionality. The Lambert-Beer law allows to write for the scattering paths with a length l:

$$\left\langle x_i^2 \right\rangle = \frac{2ls}{d} = \frac{2ns^2}{d}, \tag{2.10}$$

where n is the number of the scattering events along l, while the factor 2 comes from the statistical distribution of the step length s, which is the average distance separating two consecutive scattering events [46]. When the wave scattering is isotropic (Rayleigh scattering), s coincides with the *scattering mean free path*, which has the form

$$l_s = \frac{1}{\rho_N \sigma_s}, \tag{2.11}$$

where ρ_N is the number density of scatterers and σ_s is the cross section for the considered scattering process. Otherwise, the case of the anisotropic (Mie) scattering is described by introducing the typical distance on which the wave randomizes the direction of propagation. The latter is called *transport mean free path* l_t and is related to l_s:

$$l_t = \frac{l_s}{1 - \langle \cos\theta \rangle}, \tag{2.12}$$

where θ is the scattering angle with respect to the incident beam. Notice that if the scattering is isotropic $l_t = l_s$.

2.3.1 Diffusion

The random walks theory is useful to describes the wave propagation in random media when $\lambda \leq l^*$ and $n \gg 1$. However, the random walk approach becomes totally equivalent to the diffusion approximation yet for $n \geq 10$ because of the central limit theorem [32, 46].
In these hypothesis, l_t coincides with s and we can use the diffusion equation to describe the wave intensity propagation:

$$\frac{\partial I(\vec{r},t)}{\partial t} = D\nabla^2 I(\vec{r},t) - \frac{1}{\tau_{abs}} I(\vec{r},t), \tag{2.13}$$

where $D = vl_t/d$ and τ_{abs} are the *diffusion coefficient* (with the wave velocity v and the system dimensionality d) and the typical absorption time in the random medium, respectively. The latter term of equation 2.13 accounts for the absorption of wave intensity $I(\vec{r},t)$ We observe that the diffusion coefficient is related to the mean-square displacement by

$$\left\langle \Delta r^2 \right\rangle = 2dDt, \tag{2.14}$$

where t is the dwell time of wave in the random medium. Notice that the coherent nature of electromagnetic waves is not destroyed by the occurrence of multiple scattering, since elastically scattered waves actually preserve both the optical phase and polarization even after a very large number of scattering events. However, the scalar theory of light diffusion does not account for coherent phenomena. In fact, equation 2.13 treats the problem only in terms of light intensity, while the wave nature of electromagnetic field (phase and polarization) is completely overlooked.

2.3.2 Weak localization

During the last decades, the coherent propagation of light in disordered materials received a great interest within the scientific community because of the occurence of exciting fundamental effects, such as Anderson localization of light [32, 47, 48, 49] or random lasing [50]. Among these, one of the most striking phenomenon is the weak localization of light [51, 52], which has been observed and studied in a number of physical systems, ranging from high refractive index powders, to cold atom gases, liquid crystals and many other randomly textured materials.

Weak localization of light is due to the interference between reciprocal scattering paths, following from the theorem of reciprocity (as shown schematically in figure 2.1 a). The latter states that the scattering matrix of the reversed path is the transposed matrix of the direct path. Since this implies the full reversibility of the wave paths, the consequence is the constructive interference of multiply scattered waves in the exact backward direction, where the total phase difference between reciprocal paths is exactly zero (see figure 2.1 b). For this reason, more light is scattered back to the light source than expected by a simple scalar diffusion model, giving rise to a characteristic conical shape in the angle-dependent scattered intensity, which is named the backscattering cone (figure 2.1 c).

Therefore, the weak localization of light coincides with the occurrence of coherent backscattering (CBS) cone and causes a net reduction of light transport in the forward direction [47, 53]. This phenomenon is not restricted to light but may occur for any kind of waves. Actually, it is widely studied in other field of physics, as mechanical waves [54] and coherent atomic physics [55].

In addition to reveal the wave localization, the CBS cone manifests every time the multiple scattering of light takes place, allowing the characterization of diffusing media. In fact, it is closely related to the fact that wave paths are reversible taking in account also for the polarization [32, 45].

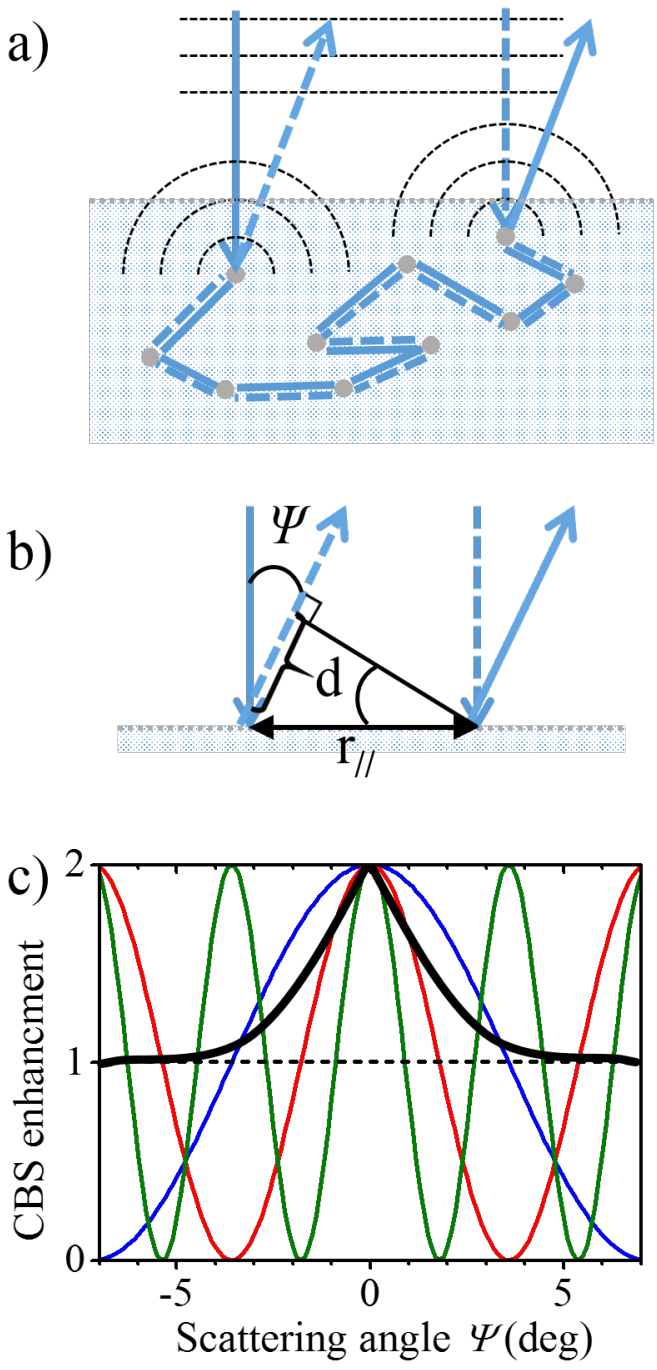

Figure 2.1: a) Reciprocal paths sketched in diffusing media. We use solid and dashed lines to represent direct and reverse path, respectively. b) Young's interference between two reciprocal paths: $r_{\parallel}$ is the displacement projected on surface; the difference of optical path d is function of the scattering angle ψ, taken with respect to the incident direction. c) The coherent backscattering enhancement (black line) built by overlapping all interference patterns (coloured lines). Here, the dashed line represents the incoherent background level.

Theory of coherent backscattering

The CBS of light is a consequence of reciprocity of Maxwell equations. Its theoretical description comes from the solution of Helmholtz equation for the electromagnetic field in diffusion approximation, written through the formalism of average Green's propagator.

In such a formalism the backscattered intensity of light, averaged over the disorder of the system, is proportional to:

$$\langle I(\vec{r})\rangle \propto \int d\vec{r}_1 \dots d\vec{r}_4 \, \langle G(\vec{r},\vec{r}_1)\rangle \, \langle G^*(\vec{r},\vec{r}_3)\rangle \, \Gamma\left(\vec{r}_1,\vec{r}_2;\vec{r}_3,\vec{r}_4\right) \langle E_{in}(\vec{r}_2)E^*_{in}(\vec{r}_4)\rangle \tag{2.15}$$

In this expression $\Gamma\left(\vec{r}_1,\vec{r}_2;\vec{r}_3,\vec{r}_4\right)$ represents the structure factor (or the total vertex) describing the multiple scattering inside the diffusing medium. The Green function $\langle G(\vec{r}_j,\vec{r}_i)\rangle$ describes the field generated at point $\vec{r}_j$ by a source at point $\vec{r}_i$. In the case of scalar waves, the Green function takes the form

$$\langle G(\vec{r}_j,\vec{r}_i)\rangle = \frac{e^{-iK|\vec{r}_j-\vec{r}_i|}}{4\pi\,|\vec{r}_j-\vec{r}_i|} \tag{2.16}$$

where $|K| = \sqrt{(\omega/c_0)^2 + nt}$ is the (complex) effective k-vector for the light inside the sample, with ω the frequency, n the density of scatterers and t the sum of all repeated scattering from one scatterer (t-matrix).

A rigorous treatment of the CBS theoretical problem is given by E. Akkermans in [56]. In this thesis, we restrict to show the quantity of interest to define the bi-static coefficient, which is the CBS observable and describes the shape of CBS cone. Therefore, we resort to the theoretical formalism of the diagrammatic expansion of Green functions developed by Diederik S. Wiersma in his Ph.D. thesis [46]. That allows a simplifying expression of backscattered intensity by separating total scattering in the diffuse background and the interference between reciprocal light paths, which are called *ladder* L and *most-crossed* C diagrams, respectively. In fact, when we deal with modestly scattering disordered systems, the calculation of the total vertex $\Gamma\left(\vec{r}_1,\vec{r}_2;\vec{r}_3,\vec{r}_4\right)$ is greatly simplified by means of the condition $kl_t \gg 1$ [57]:

$$\Gamma\left(\vec{r}_1,\vec{r}_2;\vec{r}_3,\vec{r}_4\right) = \langle L\left(\vec{r}_1,\vec{r}_2;\vec{r}_3,\vec{r}_4\right)\rangle + \langle C\left(\vec{r}_1,\vec{r}_2;\vec{r}_3,\vec{r}_4\right)\rangle \tag{2.17}$$

Figure 2.2 shows the averaged form of ladder $\langle L \rangle$ and most-crossed $\langle C \rangle$ diagrams. In this notation the cross $\times$ represents a single scattering event and is named *single scattering t-matrix* $t_\omega\left(\vec{r}_i, \vec{r}_{j+1}; \omega\right)$. The double lines represent the average Green's function $\langle G(\vec{r}_j, \vec{r}_{j+1}) \rangle$. Dotted lines connect identical scattering event. The most-crossed diagrams describe the interference between reciprocal light paths (leading to the cone of backscattering) while the ladder diagrams describe the diffuse background on which the coherent backscattering cone is superimposed.

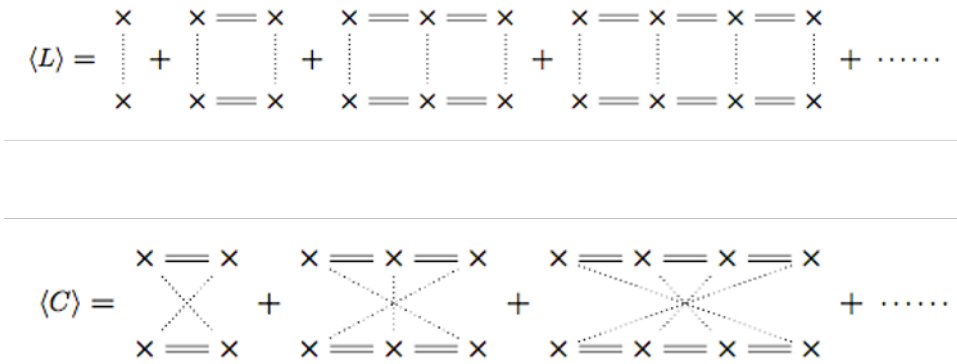

Figure 2.2: Averaged ladder $\langle L \rangle$ and most-crossed diagrams $\langle C \rangle$.

Chapter 3

Experimental characterization of light scattering

In this work we experimentally investigate the light scattering properties and multiple scattering propagation of light in disordered media. In particular, we focus on disordered nanostructures with a high aspect ratio morphology, which provide a strong absorption enhancement through light trapping over a broad wavelength range across the visible and near-infrared spectrum. These kind of nanostructured materials could be relevant for applications in Si photovoltaic devices suffering from poor absorption, such as for thin-film solar cells [19, 26, 27, 58]. Our main interest is to look for evidences of light scattering processes leading to an increased optical path for photons in a physically thin layer of absorbing material, and to correlate the light scattering properties to the physical features of the textured material.

Two different experimental techniques will be employed to study the light scattering properties of nanotextured materials: 1) the total transmission and reflection spectroscopy; 2) the angle-resolved scattering (ARS) spectroscopy [59]. These techniques are basic research methods in photovoltaics, and they are described in the following two sections. Finally, in last section of this chapter we present a modified version of the ARS technique, which is used to measure the coherent back scattering (CBS) effect arising from multiple scattering diffusion in our nanostructured materials.

3.1 Transmission and reflection spectroscopies

The total transmission and reflection spectroscopies are direct techniques to experimentally measure the total amount of light that is transmitted through or reflected off a diffusing material, which is usually shaped into a slab of finite thickness. The basic instrument for this purpose is a grating spectrometer equipped with an integrating sphere. This is essentially a hollow sphere (with a inner radius of 10 cm in our setup), whose the internal surface is covered with a material having a very high reflectivity (usually greater than 99 %) across the entire infrared (IR), visible (Vis) and ultra-violet (UV) spectral range. In our case the sphere is coated with a fine powder of barium sulphate ($BaSO_4$). The scattered light propagates into the sphere by reflecting on the inner surface until it reaches the detector window, where a phototube and a lead sulphate (PbS) detect the diffused radiation in UV and visible range and in IR range, respectively. The hollow sphere has an additional window for the reference beam and two holes for entrance and exit of the light beam (see figure 3.1). Measurements of the transmitted and reflected light are performed placing the sample at the entrance hole and at the exit one, respectively. The integrating sphere allows to discern on the diffused and specular transmission (reflection), which we indicate with T_{diff} (R_{diff}) and T_{spec} (R_{spec}), respectively. In fact, T_{spec} and R_{spec} are relative to light scattered from an optically flat interface according to the Fresnel equations[1], while T_{diff} R_{diff} are relative to light scattered by textured interface (in all directions) away from the specular one. The total transmission T_{tot} and reflection R_{tot} are given by the following equations [59]:

$$T_{tot}(\lambda) = T_{spec}(\lambda) + T_{diff}(\lambda), \tag{3.1}$$

$$R_{tot}(\lambda) = R_{spec}(\lambda) + R_{diff}(\lambda), \tag{3.2}$$

where these physical quantity are functions of the wavelength λ.

The values of $T_{tot}(\lambda)$ and $T_{diff}(\lambda)$ ($R_{tot}(\lambda)$ and $R_{diff}(\lambda)$) are calculated as the ratio of the total and diffused light intensity in transmission[2] (reflection) over the light intensity measured from the reference beam, respectively.

[1] Optically flat means that the interface defects have typical size $a \ll \lambda$.
[2] Figure 3.1 depicts the schemes for measuring these quantity.

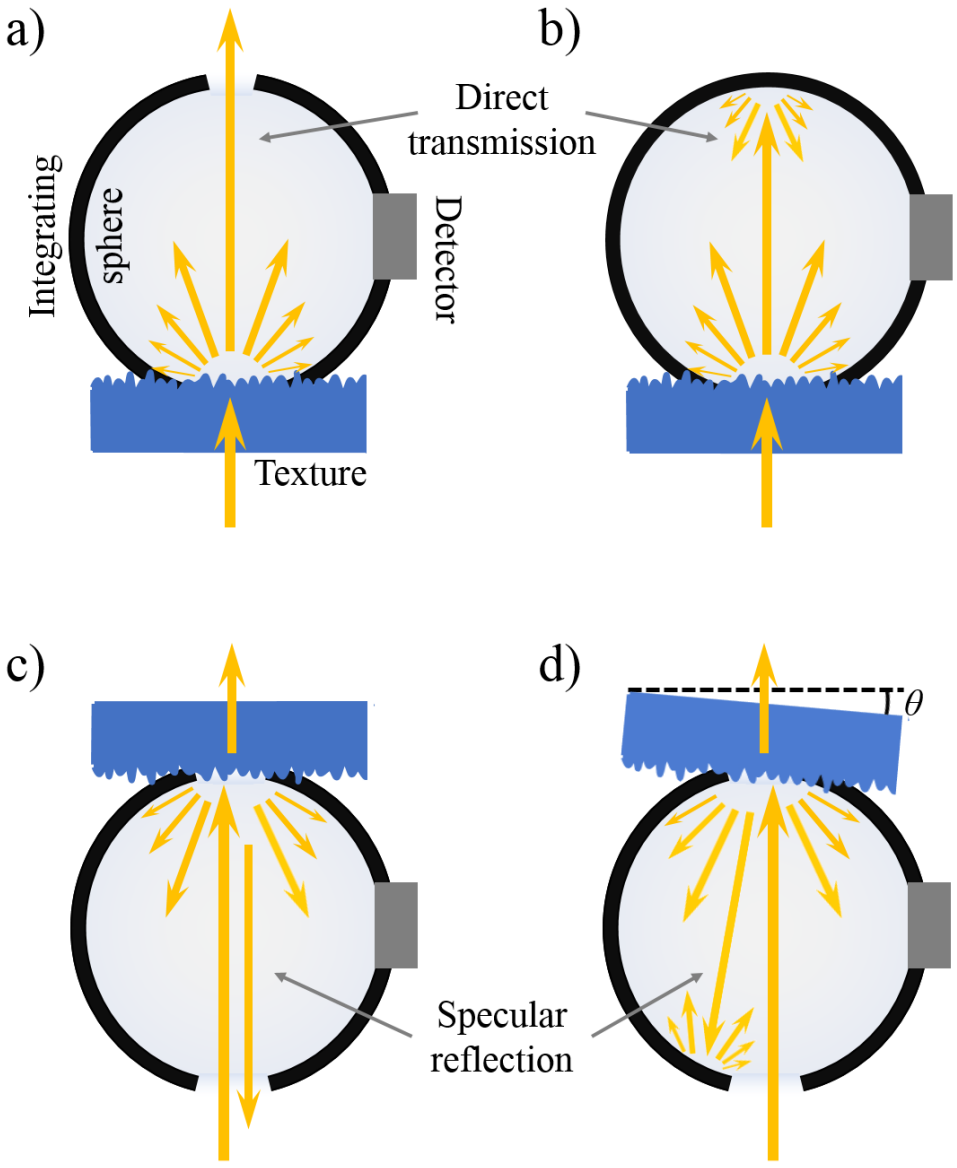

Figure 3.1: Operating scheme of the integrating sphere. The scattered light is collected on the detector by multiple reflections (here the reference beam window is not represented). Top, transmission configurations. Bottom, reflection configurations. On the left, the measurement of only diffused light. Here the specular component leaves the integrating sphere passing through the a) exit, c) entrance hole. On the other hand, the whole diffused radiation is collected on detector window by b) closing, d) tilting the exit hole.

Haze

The haze is an interesting physical quantity that can be calculated from the measurement of the total transmission and reflection spectra by normalizing the value of the diffuse transmitted $T_{diff}(\lambda)$ light to the total one $T_{tot}(\lambda)$:

$$\text{haze}_T(\lambda) = \frac{T_{diff}(\lambda)}{T_{tot}(\lambda)} \tag{3.3}$$

Hence, the haze gives the information on the fraction of the incident light which is scattered out of the specular direction. We use this technique to characterize the global scattering power of the textured samples on all the transmission half-space, as shown in section 4.3.

3.2 Angle-resolved scattering of light

The haze integrates over the angular dependence of the scattered light, which is important for determining the photon path length enhancement in thin-film photovoltaic devices. However, a more detailed information about the scattering properties of a nanostructured material can be gained from a measurement of the angular intensity distribution of the scattered light. This is obtained by the angle-resolved scattering (ARS) technique. Note that we indicate both the measurement technique and the measurement result as the ARS. This technique is also known in literature with other names, as for example the *angular intensity distribution* (AID) [60, 61] and the *angular distribution function* (ADF) [62]. Formally we define the ARS function as the ratio of scattered light power per unit of solid angle $P_s(\lambda, \theta, \phi)$ to incident power $P_i(\lambda)$:

$$\text{ARS}(\lambda, \theta, \phi) = \frac{P_s(\lambda, \theta, \phi)}{P_i(\lambda)} \tag{3.4}$$

Therefore, the $\text{ARS}(\lambda, \theta, \phi)$ is function of the light wavelength λ and of the spherical coordinates θ and ϕ, which indicate the angular direction of scattering. It indicates how strong a texture scatters into different angles as shown in figure 4.7 and 4.8, in which we report some results of ARS measurements taken in transmission configuration.

The scheme of ARS measurements is displayed in figure 3.2. It consists of a light source, whose un-polarized beam shines normally to the flat side of the substrate under investigation, and a collection arm rotating around the sample holder. A set of lenses located on the collection arm focuses the scattered light signal onto an optical fiber that brings it to the detector. The measurement is performed automatically at several collecting angles by an angular step scanning procedure.

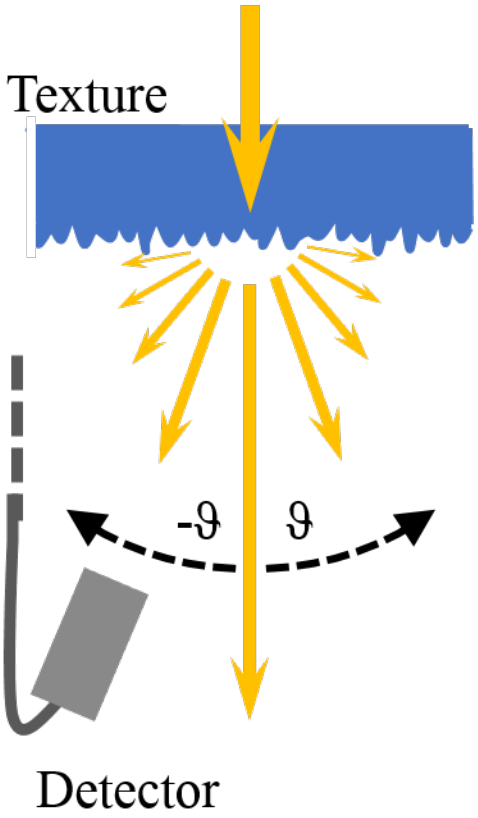

Figure 3.2: Scheme of the ARS experiment. The transparent textured substrate is placed in the rotation center of the collection arm. An unpolarized light beam shines normally on the flat side of sample and is scattered by the texture present on the other interface. The transmitted light is collected at various scattering angles by the detection system, which is placed on a rotating arm.

ARS setup

We have performed the ARS measurements using a home-made experimental setup (shown in figure 3.3 and 3.5). The light source for our experiment is a FIANIUM super-continuum laser, which provides a highly collimated white light beam (with a diameter of about 2 mm) across the range of wavelengths from 460 nm to above 1 μm. We use a power-meter to detect the intensity of the optical signal in combination with a pass-band filter (FWHM of 10 nm) to select the wavelength. The undesired IR components of the super-continuum spectrum are filtered out using a set of dichroic filters. Notice, the dynamic range of power-meter follows the optical signal over more than four orders of magnitude without changing the acquisition parameters. That allows a continuous acquisition of the ARS on all directions, including the specular one. The measurement is performed automatically by an angular step scanning procedure. A micro-step motor controlled by software rotates a goniometer on which is mounted the collecting arm.

We perform an operating test of our home-made setup by reproducing the ARS profile of the Asahi-U texture (SnO_2:F). Our results (not shown here) are in good agreement with one produced by ARTA system [59].

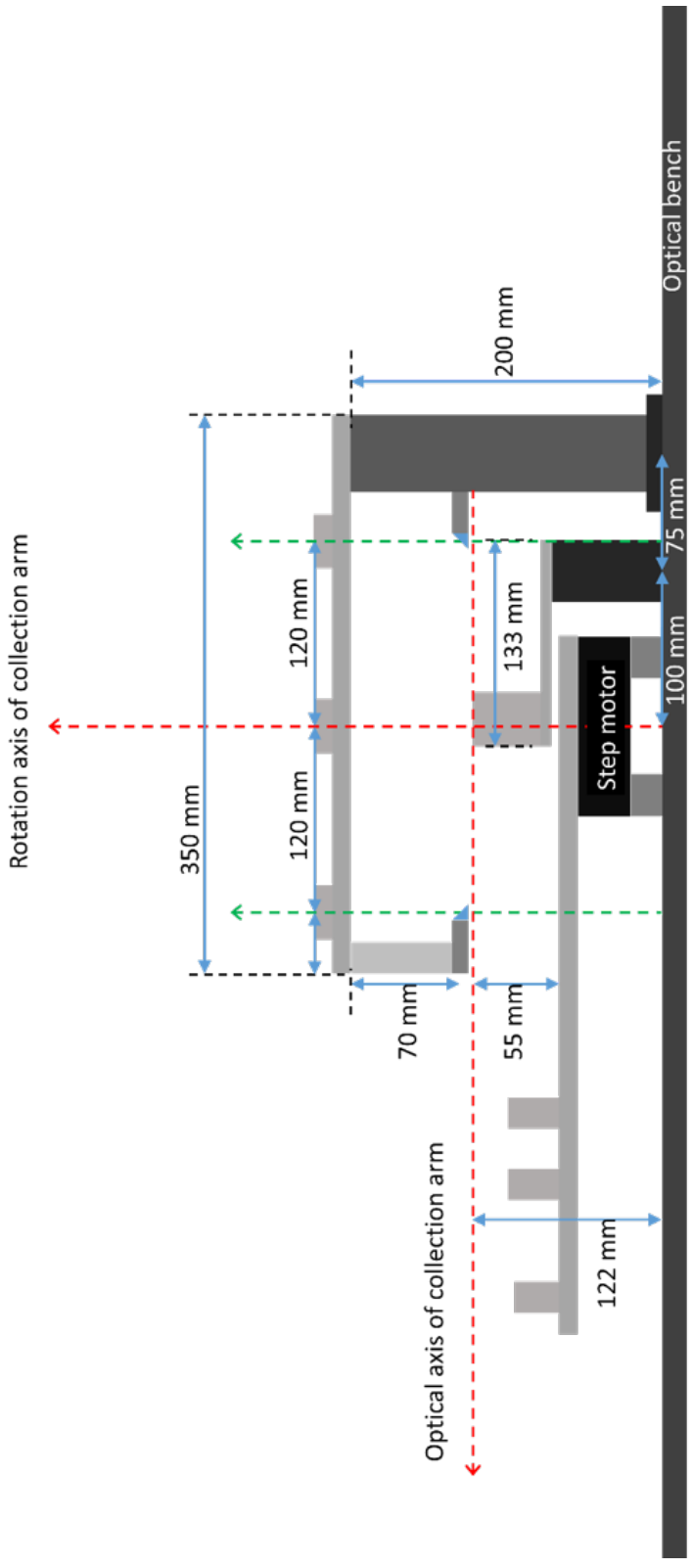

Figure 3.3: The project scheme of our home made ARS setup.

3.3 Coherent backscattering of light

Coherent backscattering (CBS) of light is a wave interference effect arising from the multiple scattering of light within a diffusing medium [56]. It manifests through an enhancement of the light scattered in the exact backward direction, which makes the measured ARS deviating from the Lambert's law[3]. This enhancement originates from constructive interference between any arbitrary multiple scattering path and its reverse, i.e. the same scattering path travelled in the opposite direction (see figure 2.1 a). In fact, the phase relation between two waves, each propagating along one of the two reciprocal paths, is preserved because the two paths travel equal optical lengths in the medium. Considering a semi-infinite diffusing medium, the last scattering point for one of the two reciprocal paths corresponds to the first one for the other path. Since any scattering event randomizes the direction of the wave propagation, these two points are sources of spherical waves and find an analogue in the slits of Young's experiment, their distance at surface represents the separation of the slits, which characterizes the angular period of the interference pattern (see figure 2.1, b). In such an intuitive explanation of the phenomenon, the CBS enhancement results from the constructive overlap of interference patterns relative to all possible reciprocal paths. Actually, this overlapping remains constructive just for angles slightly deviating from the backscattering direction, because the angular functions of interference patterns rapidly averages to one [45]. Therefore the backscattered intensity at large angle decreases to diffuse value given by the incoherent summation of all light paths (see figure 2.1, c).

The cone

The above interpretation of the CBS enhancement clarifies the typical conical shape of ARS from a diffusing medium, whose angular center does not depend on the orientation of the sample but rather on the direction of the incident light. This enhancement manifests only in the coherent part of backscattering light, which preserves the same polarization of the light beam, especially in the case of circular polarization, whereas a reflection would have the opposite circular polarization. This enhancement overcomes the incoherent background

[3]The Lambert's law describes the ARS of an ideal scatterer, which follows the cosine function where θ is the angle with respect to the normal of the surface.

even doubling the scattered intensity around the incident direction. We define the enhancement factor E of the CBS cone by the ratio of the total intensity γ_{tot} to the diffuse background intensity both at exact backscattering γ_d:

$$\mathrm{E} = \frac{\gamma_{tot}}{\gamma_d} = \left.\frac{\gamma_c + \gamma_d + \gamma_s}{\gamma_d}\right|_{\theta=0} \tag{3.5}$$

where γ_c and γ_s are the coherent component and single-scattering contribution of the intensity, respectively. The $\theta = 0$ indicates the backscattering direction [46, 63, 64]. The shape of the CBS cone reflects the path length distribution of the light inside the sample. In the ideal case of a non-absorbing semi-infinite slab, the top of the backscattering cone is a cusp. The contribution at the cusp of the CBS cone is mainly due to long scattering paths involving a large number of scattering events. An accurate determination of specific angular shape of the CBS cone also provides informations on the photonic strength of the material [46]. In fact, the FWHM of the CBS cone is proportional to the wavelength λ over the transport mean free path of light in the medium l_t (see section 2.3):

$$\mathrm{FWHM}_{CBS}(\lambda) \propto \frac{\lambda}{l_t}. \tag{3.6}$$

If absorption is present in the material, the contribution from the longer paths is strongly suppressed and consequently the cusp becomes rounded. A similar effect is due to the finite thickness of the diffusive medium and to the spot size of the light beam, which should be greater than $10l_t$ to avoid a significant rounding of the peak. Nevertheless, the presence of absorption and the finite size of sample modify the shape of the CBS cone without reducing its enhancement, because they limit the length of paths without destroying the optical coherence. To account for these effects, we fitted the experimental data using a finite-slab model for the CBS intensity including a characteristic inelastic mean free path l_i, as shown in section 3.4. On the contrary, the CBS enhancement can be reduced by dephasing effects (as for instance magneto-optical Faraday rotation) that invalidate the reciprocity hypothesis indispensable for the existence of the reciprocal paths. For the same reason, the coherence area of the light source is a key issue [45].

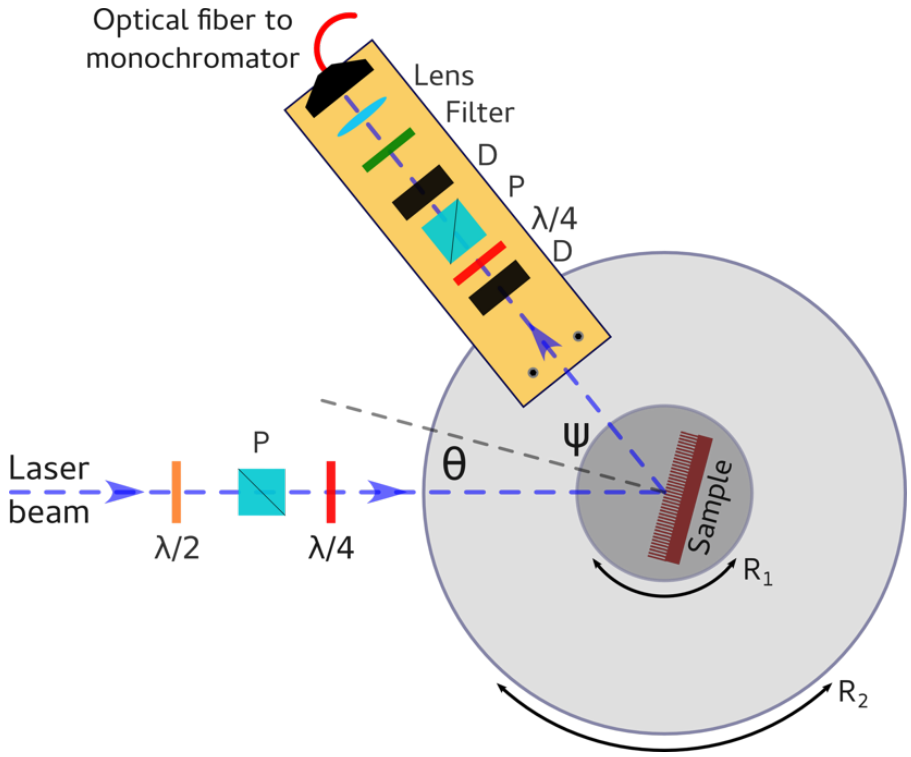

Figure 3.4: Scheme of the experimental setup for CBS measurements [65].

The setup

The CBS measurements consist in a modified ARS experiment with high angular resolution. Therefore we have modified our home-made ARS setup, by taking inspiration from the one described in [65], and programmed a LabView control software for semi-automation of the measurement [66]. The scheme of the experimental setup is sketched in figure 3.4, while figure 3.5 shows some pictures of this home-made setup.

The sample (a diffusing medium) is placed on the x-y-z-rotation stage shown in figure 3.5 b), which allows to position the sample surface in the exact rotation centre of the collection arm (yellow part in figure 3.4) in order to obtain symmetric and reliable measurements. If the sample is not liquid, the speckle patterns are averaged out by rotating the sample. The sample is excited with a polarized laser beam, usually at normal incidence. The intensity of the laser beam is controlled by a rotating $\lambda/2$-plate and a linear polarizer. Both linear and circular polarisations are used. The latter is realized by a $\lambda/4$-plate and is used to collect the coherent part of backscattered signal, since

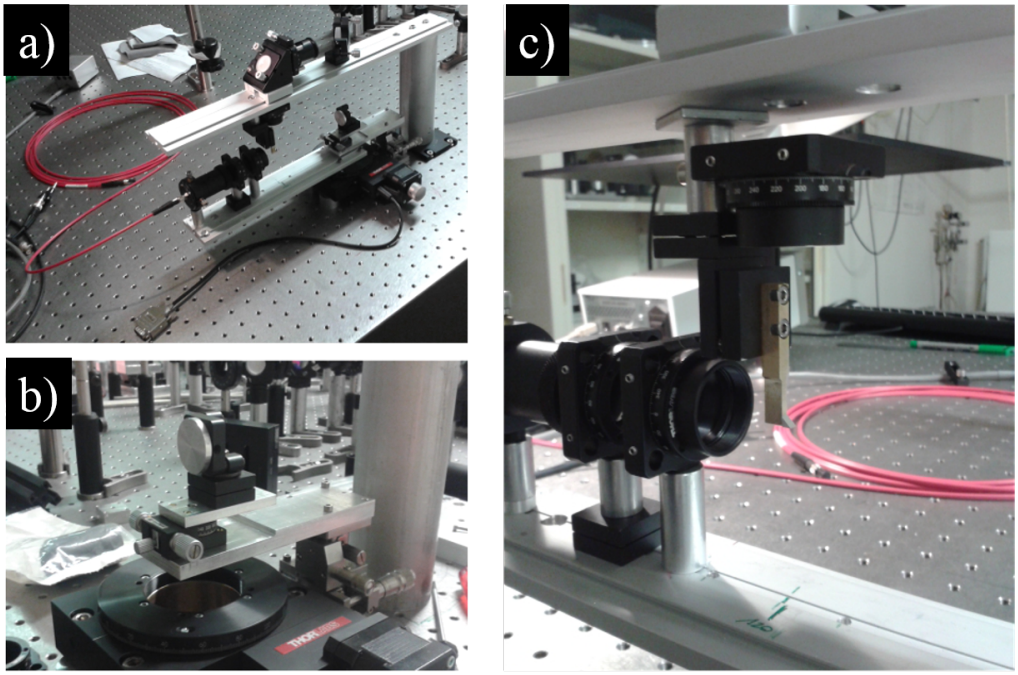

Figure 3.5: Some photos of the home made ARS-CBS setup [66].

the multiple scattered light preserves the polarization chirality while the single scattered light reverses it. Notice that the spatial coherence and homogeneity of the wave front are essential to avoid a reduction of the enhancement factor due to a difference in intensity at the beginning and the end point of a random walk. Therefore, we cut off the Gaussian beam profile by means of a diaphragm hole. The laser beam is driven on the sample by means of a semi-transparent mirror or a small 45° mirror. Using the semi-transparent mirror, the undeflected part of laser beam must be completely absorbed by a black filter or a beam damper. The 45° mirror is less critical than the semi-transparent mirror, which creates most of the experimental artifacts. However, the width of this cone is smaller than about one degree, in the majority of cases. Therefore, to avoid too much shadowing of the cone tip, the small mirror is useful just in the case of very strongly scattering samples with rather large cones, as in our cases (see chapter 6). The backscattered signal from the sample is filtered by a $\lambda/4$-plate and a linear polarizer, which works as analyser, placed on the collection arm. The coherent signal is selected by conserving the orientation of the polarization (helicity-conserving channel), while the only diffused (incoherent) background is collected by means of the analyser with the axis orthogonal to

the one of the polarizer (non-conserving channel) [45]. Then, the filtered signal is collected through an achromatic doublet lens mounted on the collection arm and focused on the core of a multi-mode optical fibre (a = 550 μm). The signal is finally analysed through a spectrometer (a monochromator Acton SP-2300 coupled to a liquid-nitrogen cooled Silicon CCD Spec 10 System, both made by Princeton Instruments). A powermeter used instead of the spectrometer can provide a higher dynamic range, but a lower spectral resolution. To ensure measuring the absolute intensity, a dark reference is subtracted from the sample measurement. The angular resolution can be selected by varying the aperture of one or more diaphragms mounted between the analyser and the lens. We achieve an angular resolution of about 0.1 deg without losing the quality of light signal.

In all our CBS experiments, we optically excite the sample by means of a laser (532 nm and 488 nm CW solid state lasers and a 785 nm diode laser) focused to a 1 mm diameter spot onto the sample surface. We collect the backscattered signal as a function of the scattering angle both in helicity-conserving channel, i.e. by selecting the same circular polarization of the pump beam, and in the two linear polarizations (non-conserving channel). While the first polarization allows also to collect the coherent component of backscattered signal, the collected signals in these two latter polarizations, which contain only the incoherent component for the backscattering light, are averaged to obtain the normalization of the signal from the conserving channel.

3.4 Fitting model for finite slab

Section 2.3 treats the CBS model for the semi-infinite diffusing medium. However, most of the samples that are investigated have a finite slab geometry. Therefore, in this section we give the stationary solution to the diffusion equation for such a geometry. The starting point is the diffusion equation 2.13 written in the stationary case, i.e.the time derivative on the left hand side is zero. We can account for an incoming intensity by adding a source function $S(\vec{r})$ on the right hand side, which for an incoming plane wave from the infinite takes the form $S(\vec{r}) = S_0 e^{-r\kappa_e}$, where $\kappa_e = l_e^{-1} = l_s^{-1} + l_i^{-1}$.

This yields:

$$\frac{1}{3}l^2\vec{\nabla}^2 I(\vec{r}) - l\kappa_i I(\vec{r}) + S(\vec{r}) = 0 \tag{3.7}$$

Notice that it is useful to solve the problem of light intensity propagation in the disordered media independently from the profile function of the incoming intensity $S(\vec{r})$, solving the equation

$$\frac{1}{3}l^2\vec{\nabla}^2 F(\vec{r}_1, \vec{r}_2) - l\kappa_i F(\vec{r}_1, \vec{r}_2) = -\delta(\vec{r}_1, \vec{r}_2) \tag{3.8}$$

where $F(\vec{r}_1, \vec{r}_2)$ is the intensity propagator, i.e. the Green function for the intensity in the medium, and it is related to the intensity function $I(\vec{r})$:

$$I(\vec{r}_1) = \int d\vec{r}_2 F(\vec{r}_1, \vec{r}_2) S(\vec{r}_2)\,. \tag{3.9}$$

Here the integration over $d\vec{r}_2$ is taken over the whole volume of the scattering medium (the sample). The intensity propagator $F(\vec{r}_1, \vec{r}_2)$ describes the propagation of the intensity in a disordered slab in the diffusion approximation. It is convenient to choose the orientation of the slab such that its interface is perpendicular to the z-axis. Then the system has translational invariance over the xy-plane and we can use the Fourier transform:

$$F(\vec{q}_\perp, z_1, z_2) = \int d\vec{r}_\perp F(\vec{r}_1, \vec{r}_2) e^{i\vec{r}_\perp \cdot \vec{q}_\perp} \tag{3.10}$$

where $\vec{r}_\perp = \vec{r}_{1\perp} - \vec{r}_{2\perp}$ and $\vec{q}_\perp = \vec{k}_{1\perp} - \vec{k}_{2\perp}$ are perpendicular to z. $\vec{k}_{2\perp}$ and $\vec{k}_{1\perp}$ are the perpendicular components of the incoming and outgoing wavevector, respectively [46, 67]. After Fourier transforming the equation 3.8, we obtain:

$$\frac{1}{3}l^2\left(\frac{\partial^2}{\partial z_1^2} - q_\perp^2\right) F(\vec{q}_\perp, z_1, z_2) - l\kappa_i F(\vec{q}_\perp, z_1, z_2) = -\delta(z_1 - z_2) \tag{3.11}$$

From radiative transfer theory, it is known that the diffusive intensity at the front and rear interface ($z = 0$ and $z = L$) of the sample is not zero. The appropriate boundary condition for a slab is found by taking the intensity zero at distance z_0 from the interface. The value of z_0 depends on the refractive index contrast between the sample and its surrounding medium. For an index matched sample interface it value is $z_0 \simeq 2/3l_t$. Solving equation 3.11 with this boundary condition, we find:

$$F(\vec{q}_\perp, z_1, z_2) = F(\vec{q}_\perp, z_s, z_d) = \frac{3\cosh[\alpha(L - z_s)] - 3\cosh[\alpha(L + 2z_0 - |z_d|)]}{2l^2\alpha\sinh[\alpha(L + 2z_0)]} \tag{3.12}$$

where $z_s = z_1 + z_2$, $z_d = z_1 - z_2$, L is the slab thickness and $\alpha = \sqrt{l_{abs}^{-2} + q_\perp^2}$ with $l_{abs} = \sqrt{l_t l_i/3}$ the absorption length in the medium.

We consider the backscattered intensity in terms of the bistatic coefficient γ, defined as the measured scattered flux per solid angle and per unit of the probed area, normalized to the incident flux. In particular the coherent intensity γ_c for a finite slab of thickness L can be modelled by the following expression [46, 68, 69]:

$$\begin{aligned}
\gamma_c(\psi) = \; & \frac{3e^{-uL}}{-2\alpha l_t^3 \sinh[\alpha(L+2z_0)]\left[(u^2+\eta^2-\alpha^2)^2+(2\alpha\eta)^2\right]} \times \\
& \left[2\left(-\alpha^2+u^2+\eta^2\right)\cosh\left(2\alpha z_0\right)\cos\left(L\eta\right)\right. \\
& +4\alpha\eta\sinh\left(2\alpha z_0\right)\sin\left(L\eta\right) \\
& +2\left(-\alpha^2-u^2-\eta^2\right)\cos\left(L\eta\right) \\
& -2\tfrac{\alpha}{u}\left(\alpha^2-u^2+\eta^2\right)\sinh\left[\alpha\left(L+2z_0\right)\right]\sinh\left(uL\right) \\
& +2\left(\alpha^2-u^2-\eta^2\right)\cosh\left[\alpha\left(L+2z_0\right)\right]\cosh\left(uL\right) \\
& -4\alpha u\sinh\left(\alpha L\right)\sinh\left(uL\right) \\
& \left.+2\left(\alpha^2+u^2+\eta^2\right)\cosh\left(\alpha L\right)\cosh\left(uL\right)\right]
\end{aligned} \tag{3.13}$$

where ψ is the angle formed between the incoming and the outgoing wavevectors. The $\gamma_c(\psi)$ expression is a function of the following parameters: $\eta \equiv k(1-\mu_s)$, $u \equiv \frac{1}{2}\kappa_{ext\_C}(1+\mu_s^{-1})$ and α. Here $k = \frac{2\pi}{\lambda}$ in the light wavevector, $\mu_s = \cos\psi$, $z_0 = al_t$ is the extrapolation length accounting for internal reflections at the boundaries ($z = 0$ and $z = L$) [70, 71], $\kappa_{ext\_C} = l_t^{-1} + l_i^{-1}$ is an effective extinction coefficient accounting for the attenuation of scattered intensity and $\alpha \equiv \sqrt{L_{abs}^{-2} + q_\perp^2}$ is the diffusive extinction coefficient, with $L_{abs} = \sqrt{\frac{l_t l_i}{3}}$ and $q_\perp = k\sin\psi$. For the expression describing the diffuse background γ_l we also introduce the parameter $\nu \equiv \frac{1}{2}\kappa_{ext\_D}(1-\mu_s^{-1})$. Since γ_l is evaluated at $q_\perp = 0$, as a direct consequence $\alpha \equiv \sqrt{L_{abs}^{-2}}$ and the bistatic coefficient representing the diffuse background contribution becomes:

$$\gamma_l(\psi) = \frac{3Z_1\left[\left(1+e^{-2L}\right) + Z_2\left(1-e^{-2L}\right) + Z_3 e^{-L(u+\nu)}\right]}{-2\alpha l_t^3 \sinh\left[\alpha\left(L+2z_0\right)\right] u\left[\left(u^2-\alpha^2\right)^2 + \nu^2\left(\nu^2-2\alpha^2-2u^2\right)\right]} \tag{3.14}$$

where,

$$\begin{aligned} Z_1 = \; & u(\nu^2-u^2+\alpha^2)\cosh\left[\alpha\left(L+2z_0\right)\right] + u\left(u^2-\nu^2+\alpha\right)\cosh\left(\alpha L\right) \\ & -2u\nu\alpha\sinh\left[\alpha\left(L+2z_0\right)\right] - u\nu\alpha\tfrac{\nu^2-\alpha^2-3u^2}{u^2-\alpha^2}\sinh\left(\alpha L\right) \end{aligned} \tag{3.15}$$

$$\begin{aligned} Z_2 = \; & \nu(u^2-\nu^2+\alpha^2)\cosh\left[\alpha\left(L+2z_0\right)\right] - 2u^2\alpha\cosh\left(\alpha L\right) \\ & +\alpha(u^2+\nu^2-\alpha^2)\sinh\left[\alpha\left(L+2z_0\right)\right] + u^2\nu\tfrac{\nu^2-u^2-3\alpha^2}{u^2-\alpha^2}\cosh\left(\alpha L\right) \end{aligned} \tag{3.16}$$

$$\begin{aligned} Z_3 = \; & 2u(\nu^2-u^2-\alpha^2) + 2u(u^2-\nu^2-\alpha^2)\cosh\left(2z_0\alpha\right) \\ & +4u\nu\alpha\sinh\left(2z_0\alpha\right) \end{aligned} \tag{3.17}$$

Finally, the fitting function of the coherent backscattering cone is defined as follows:

$$I(\psi) = 1 + \frac{\left(E_{exp}-1\right)\gamma_c}{\left(E-1\right)\gamma_l} \tag{3.18}$$

where E_{exp} is the experimental enhancement factor, which deviates from its theoretical value 2 due to residual of single scattering and the stray light, and $E = 1 + \frac{\gamma_c}{\gamma_l}$ is the theoretical enhancement factor. We observe that the occurrence of some dephasing effect in the multiple scattering medium can lower the enhancement factor E from its theoretical value [56]. Therefore, when this effect is expected, also E is set as a free fitting parameter. The other fitting parameters are the transport mean free path l_t and L. On the other hand, the inelastic scattering length l_i is a fixed parameter of fitting function, since its value is estimated by scaling the extinction length of the absorbing material to its percentage present in the diffusing medium.

The fitting model for the CBS cone shown above is developed in the hypothesis of isotropic diffusing medium. Nevertheless, CBS in highly anisotropic systems (such as our samples) can be anyway modelled within the diffusion approximation, if light scattering in the plane perpendicular to the backscattering direction can be considered isotropic. Actually, the CBS cone is related to the Fourier transform of the spatial distribution of scattered light intensity on the sample surface. Therefore, the in-plane horizontal scattering is the only responsible for the building up of the CBS cone, while the much higher (in our case) transport mean free path along the vertical direction may influence its angular width, together with the finite thickness of the NWs layer [56, 63, 64].

Chapter 4

Substrate for thin-film photovoltaic applications

The optimization of solar cells (SCs) architecture aims to maximize both light absorption and charge collection efficiencies, which jointly determine the SC conversion efficiency. To allow the almost complete absorption of the incident photons with energy greater than energy gap of active material, the thickness of absorber layer should be much greater than the optical extinction length, since the light absorption in dielectric medium follows the negative exponential trend with the length of photon path. On the other hand, the average distance from the creation to collection of photon-generated charges in the active medium has to be shorter than their diffusion length to avoid recombination losses. This requires the absorbing layer between the two electrodes to be electronically thin. The traditional planar SC architecture designs the two electrodes lying respectively on the opposite surfaces of the absorber layer. Therefore, the thickness value of this latter comes from a trade-off between the light absorption and the charge collection efficiency. The thin-film SC design benefits from the minimization of the absorber thickness reducing the recombination losses. Another advantage of thin-film SCs design comes from the less consumption of active medium in the absorber layer realization, which results in reduction of fabrication cost of the SC. However, in order to maintain a good value of conversion efficiency, the cell must be assisted by photonic structures that can enhance the absorption of incident light. These structures work as an antireflection layer and increase the mean photon path in the active material.

Their operating principle is based on the *light trapping* and on the radiation intensity enhancement showed by E. Yablonovitch for a textured optical sheets [72]. In the last years, the development of thin-film SCs challenges the photovoltaic research community to improve the light-trapping technologies.

The presence of sub-wavelength features on an optical interface perturbs the refractive propagation of light by Mie scattering, spreading the light beam in a way that increases at shorter wavelengths. Even sub-wavelength features with high aspect ratio allow a progressive transition between air and substrate matching the different refractive index values of two media, as illustrated in section 2.2. This works similarly to the bio-mimetic broadband anti-reflection observed in the corneas of nocturnal moths [43, 44]. Otherwise, surface corrugations with lateral size comparable or larger than the light wavelength scatter light at large angles, which can exceed the total internal reflection critical angle [40, 73].

The implementation of these two effects in the architecture for thin-film SCs appears as a promising approach for broadband light trapping and for effective photon harvesting [20, 74, 75]. In this context, nanofabrication techniques that ensure patterning of a broad range of materials over macroscopic areas in a cost effective way are required.

In this chapter we are going to present the study of light-scattering properties of a self-assembled nanotexture fabricated by defocused ion beam sputtering at the University of Genova. In particular, we show the characterization of the light diffused in transmission by means of measurements of the integrated intensity and the angular dependence of scattering [59]. Looking for advantages of the novel substrate, we discuss the experimental results benchmarking them with those obtained for the Asahi-U glass, which is the growth substrate commonly employed in the fabrication of thin-film silicon SCs. Also, we analyse the results in terms of the Lambertian trend (i.e., a cosine dependence on the scattering angle), which is considered to be the reference for light-trapping and photon harvesting in SCs [72], and can be treated theoretically by simple analytical models. Finally, we relate the peculiar features arising from angle-resolved scattering to the statistical properties of the morphology of the texture, which exhibits both a random roughness and pseudo-periodic patterns.

4.1 Sample preparation

The investigated texture is obtained on borosilicate glass by defocused ion beam sputtering (IBS) with the help of a self-assembled stencil mask. This is required to achieve high aspect ratio textured glass because of smoothing mechanisms activated in amorphous materials by ion irradiation. A predeposited metal film auto-organizes on the surface under the ion flux and drives the erosion shielding of the underlying substrate [76]. The IBS technique is employed in nanopatterning and in functionalizing materials over large areas [77]. The samples investigated here have been prepared following a new version of the IBS process. The life-cycle of the metallic mask is extended by a supplement deposition of metal atoms during the ion irradiation to furthering the vertical dynamics of the surface pattern [78].

The stencil mask

The aforementioned sacrificial metal stencil mask is prepared by depositing a 150 nm polycrystalline Au film under UHV conditions on glass substrates by thermal evaporation from an alumina crucible at a constant rate fixed at $6\text{nm} \cdot \text{min}^{-1}$ by means of a quartz microbalance. Subsequently, the defocused ion beam irradiation from a Ar^+ source (Tectra instruments) shoots the substrate under grazing incidence conditions ($\theta = 82°$) at a constant flux[1] of 4.9×10^{15} ions $\cdot$ cm^{-2} $\cdot$ s^{-1}. A tungsten filament supplies electrons via thermionic emission to avoid charge effects on surface.

Since ion induced roughening mechanisms favour erosion of regions with positive curvature, i.e., in correspondence to a trough [79, 80], an anisotropic pattern forms at the surface of the polycrystalline film. The metal auto-organizes in ripples elongating parallel to the ion beam projection for several micrometer (see sketch 1 in figure 4.1). The ripple amplitude increases with ion dose until an array of disconnected nanowires is formed (ion fluence of 8.9×10^{18} ions $\cdot$ cm^{-2}) and the underlying bare glass appears in-between. At this point, the stencil mask guides selectively the etching of the underlying substrate in correspondence to the metal disconnections.

The lifetime of the stencil mask under ion bombardment conditions is prolonged by reactivation metal deposition with a flux comparable to the metal

[1]The flux is measured in a plane orthogonal to the beam direction

erosion rate. Heating up the substrate to 700 K, the ripples incorporate the extra Au atom (figure 4.1 sketch 2). The Au flux is stopped after an ion fluence of 1.8×10^{19} ions $\cdot$ cm^{-2}. The ion beam continues to carve the glass surface, while the gold nanowires shrink. The fabrication process terminates with the complete etching of the gold. The final result of the IBS process is the textured glass into which the pattern of stencil mask should be propagated with a vertical amplification, as shown in sketch 3 of figure 4.1.
There are some imbalances between eroding and redepositing of gold mask due to the Gaussian profile of the Ar^+ ion beam intensity distribution on the large size of glass (2×3 cm^2), further amplified by the grazing incidence conditions employed for this experiment. This allows to obtain different morphologies to investigate on the same substrate.

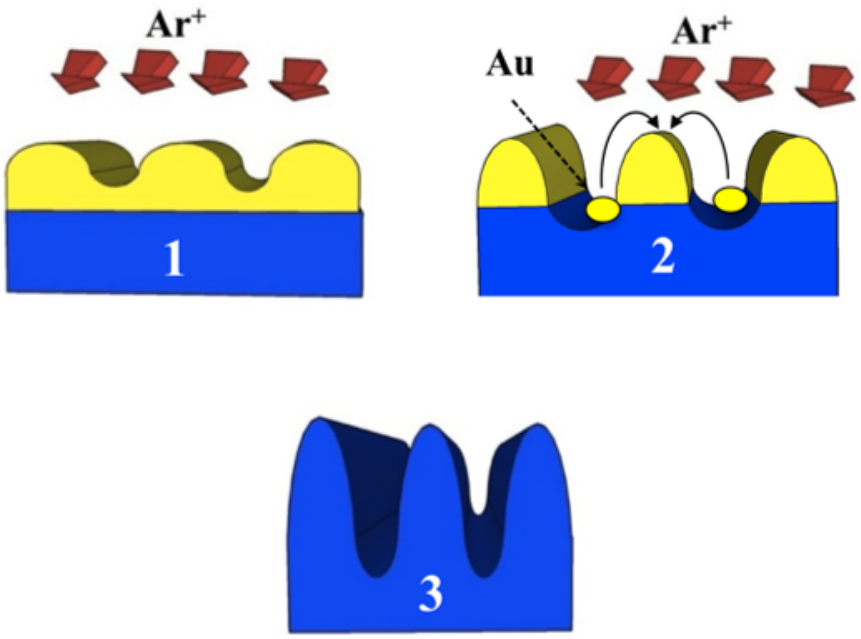

Figure 4.1: Sketches of the preparation process steps: 1) Au stencil mask formation, 2) deposition of Au atom and Ar ions on the heated sample, 3) final exposure to Ar ions to remove residual Au of the mask.

4.2 Morphological characterization

Light scattering and atomic force microscopy (AFM) studies are closely related in the reciprocal space, as it was already demonstrated by Dumié et al [81]. For this reason the morphological features of the textured glass are investigated ex-situ by AFM operating in intermittent-contact mode (ezAFM from Nanomagnetics Instruments and Nanosurf Mobile S) equipped with a high aspect ratio Si tip (ACLA by AppNano).

The topography images have been processed by using WSxM software [82], which allows to evaluate some statistical parameters of interest to correlate the scattering properties to the texture morphology, such as root-mean-square (RMS) roughness σ, autocorrelation functions, power spectral density. Actually, we find uniform morphology on a cm^2 scale and identify three main regions characterized by the presence of the lowest, the highest and medium value of RMS roughness σ, which we label hereafter by Zone 1, Zone 2 and Zone 3, respectively. Figures 4.2 a) and b) show the AFM images of Zone 2. We can see the dominant presence of elongated shapes characterized by regular alternation of heights and depressions on a vertical dynamic range around 700 nm. In figure 4.2 c) we report also the AFM topography of a reference Asahi-U substrate, which evidences the presence of pyramidal clusters with a vertical dynamic range around 100 nm and dominant lateral sizes in the range of 300 nm. In Zone 2 the RMS roughness has a value of $\sigma = 140$ nm. Here, in the middle of the sample, the Au atom dose and Ar^+ ion fluence are optimally matched. However, in the other two regions of the substrate located at the bottom edge, Zone 3, and at the top edge, Zone 1, the RMS roughness equals $\sigma = 100$ nm and $\sigma = 30$ nm, respectively. A RMS roughness of $\sigma = 36$ nm characterizes the Asahi-U substrate.

The analysis of the autocorrelation function (ACF) and of the 1-dimensional power spectral densities (1D-PSD) gives the quantitative information about size and periodicity distribution of the nanostructures [83, 84]. The ACF is a powerful tool since it allows to average out uncorrelated fluctuations and to extract the periodicity of the dominant spatial modulations. It can be calculated as a 2-dimensional image matrix $G(m, n)$ from the AFM data by the formula:

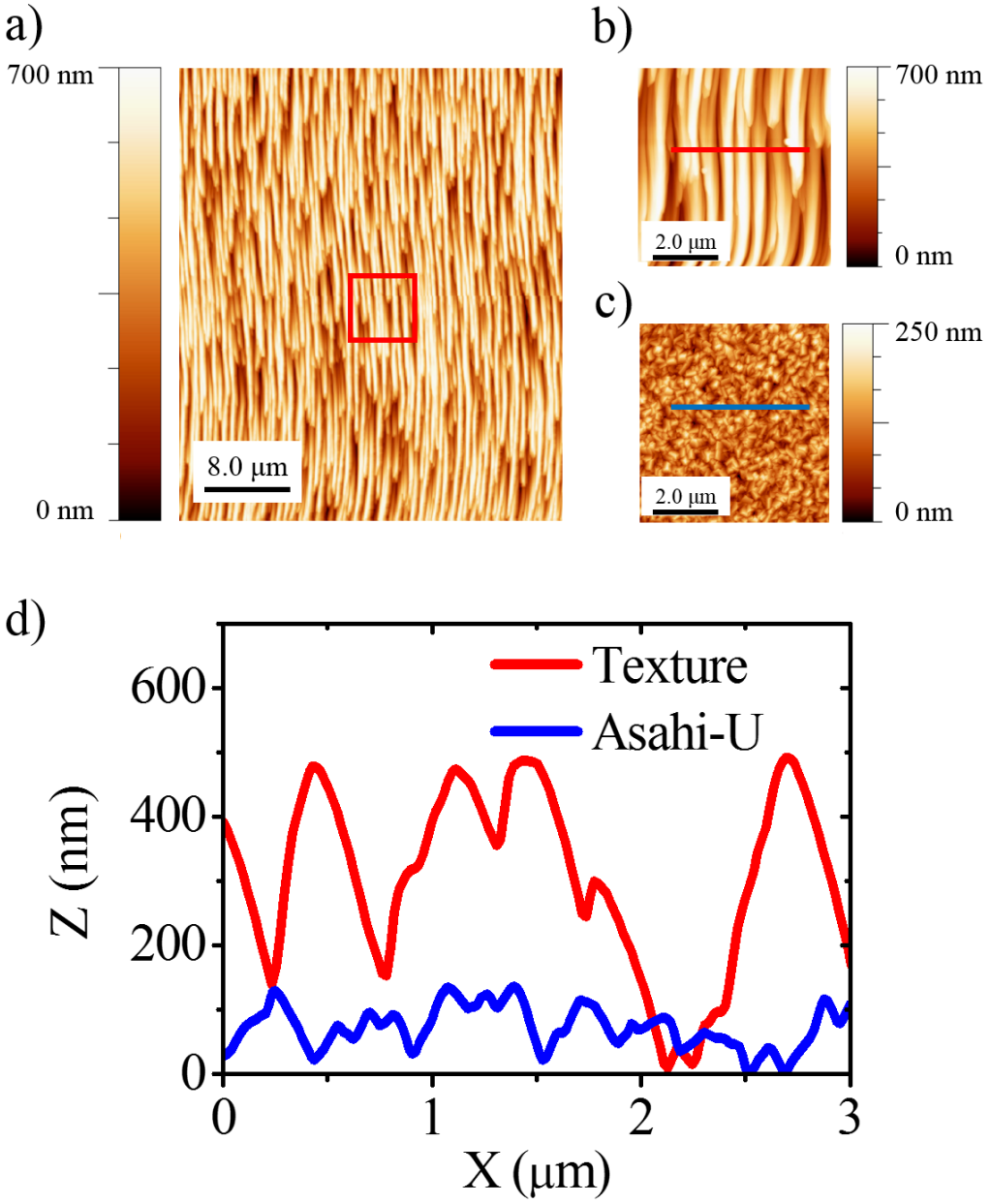

Figure 4.2: The AFM topographies acquired on the investigated samples. a) The Zone 2 of nanostructured glass: image size 40×40 μm^2, vertical range 700 nm. b) Zoom of the square region surrounded by red line in a): image size 6×6 μm^2. c) An Asahi-U SnO_2 film supported on glass: image size 6×6 μm^2, vertical range 250 nm. d) Topographic line profiles along the highlighted red and blue lines on nanostructured glass and Asahi-U, respectively.

$$G(m,n) = \frac{1}{(N-n)(M-m)} \sum_{l,k=1}^{N-n,M-m} Z_{l,k} Z_{l+n,k+m} \tag{4.1}$$

where $Z_{l,k}$ and $Z_{l+n,k+m}$ are the topographic images laterally shifted by n and m pixels, respectively, corresponding to a certain shifting length $r_{n,m}$. The ACF function has a maximum in the origin for $m = n = 0$ and, in the presence of a periodical pattern, it exhibits secondary maxima that define the auto-correlation length of the pattern.

Figure 4.3 shows line profiles of the ACF functions computed from AFM images of the Asahi-U sample and of three different patterns identified on regions Zone 1, Zone 2 and Zone 3 of the glass surface. The ACF line profiles are cut orthogonally to the ripple direction, across the central peak at $m = n = 0$, and are normalized and shifted vertically for a better comparison. Notice that the ACFs exhibit an oscillating pattern for large r values.

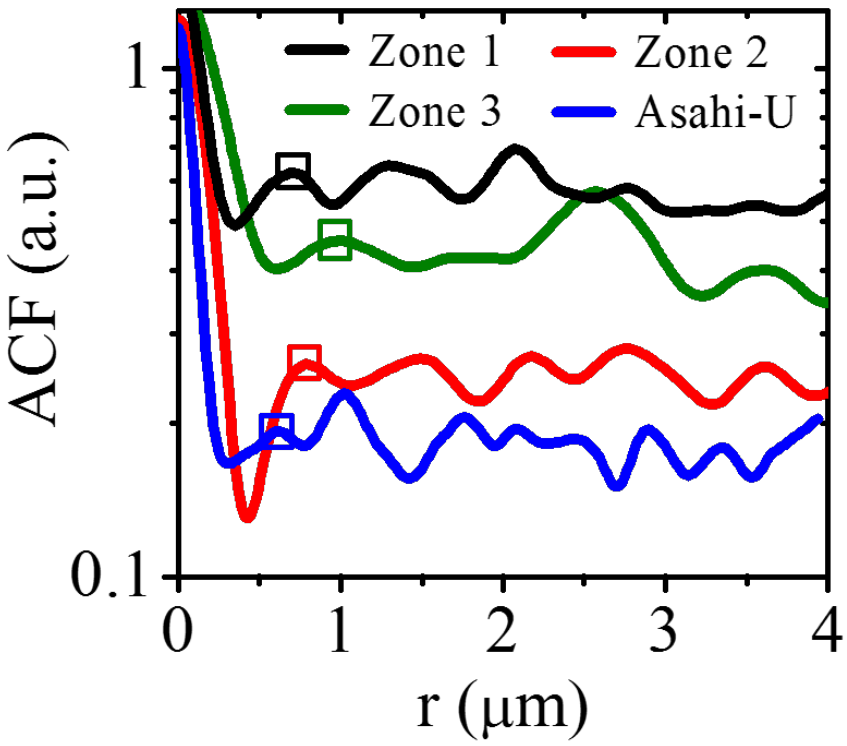

Figure 4.3: Log-log plot of autocorrelation function computed from AFM data, which are collected scanning the sample surfaces for a length of about 5 μm.

This indicates a pseudo-periodic nature of the ripples with some degree of correlation extending up to distances in the range of 10 μm. The autocorrelation lengths derived from the ACFs in Zone 1, Zone 2 and Zone 3 read $W_1 = 780 \pm 10$ nm, $W_2 = 800 \pm 10$ nm and $W_3 = 1000 \pm 10$ nm, respectively, as highlighted by the boxes drawn on the first order peaks of ACF curves (see figure 4.3). The 1-dimensional power spectral densities function has been calculated from the AFM data in order to better evidence the dominance of specific spatial components, see figure 4.4. The 1D-PSD function is derived from the 1-dimensional AFM line scans acquired along the fast scan direction according to a discrete Fourier transform procedure:

$$\text{1D-PSD}(q_x) \propto L \left[\frac{1}{N} \sum_{k=1}^{N} h_k \exp\left(2\pi i x_k q_k\right) \right]^2 \tag{4.2}$$

where $h_k = h(x_k)$ is the height sampled at the discrete position $x_k = k \cdot \frac{L}{N}$. In these formulas, N is the number of data-points sampled per line (generally $N =$ 512 or 1024), and the spatial frequency is calculated at discrete values $q_x = j\frac{1}{L}$, $j = 1, 2, ...\frac{N}{2}$. The 1D-PSD curve subtends an area, which is proportional to σ^2, so a comparison of the curves allows identifying how spatial modulations with different wave-vectors q_x contribute to the total RMS roughness. All curves shown in figure 4.4 present a flat response in the lower part of the spatial frequency spectrum and a power law roll-off with frequency in the upper part of the spectrum, which is compatible with a q_x^{-4} scaling. This indicates that the surface morphology scales self-similarly up to a critical lateral scale λ^* (critical wavevector $q^* = 1/\lambda^*$) determined by the range of the relaxation mechanisms, which are dominated by surface diffusion (either thermally activated or ion induced) [85, 86, 87]. For Zone 2 and Zone 1 the crossover is found in a range of $\lambda^* \approx 500$ nm. For the over-exposed region Zone 3 the crossover λ^* shifts to 1000 nm, due to the increased coarsening. The 1D-PSD curves also reveal that, in the range $q > q^*$, Zone 2 is characterized by harmonic components with higher amplitude. The role of surface morphology on the optical response of glass rough sample is highlighted in the next section.

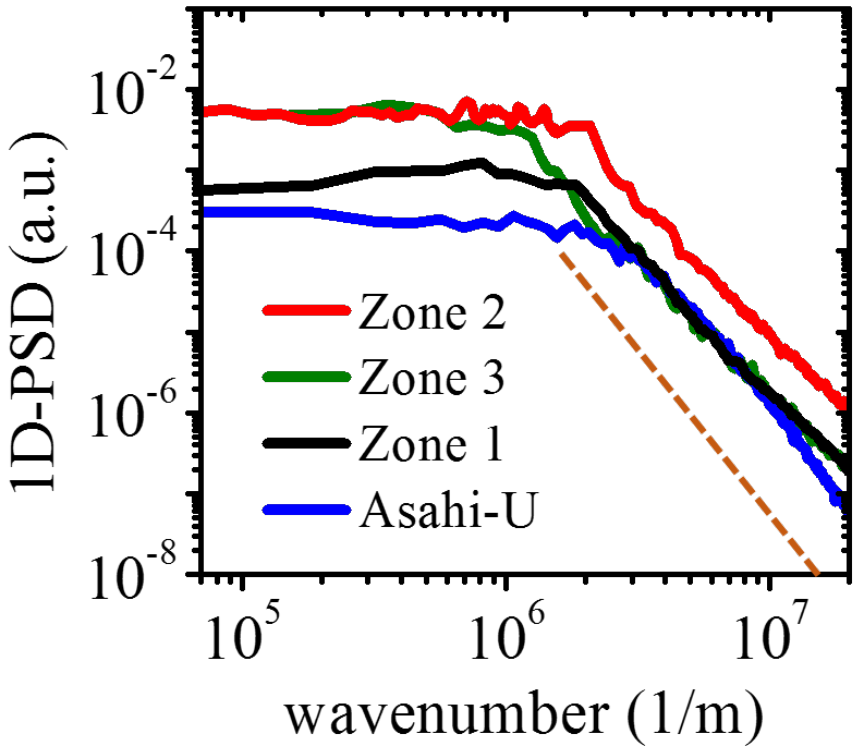

Figure 4.4: Log-log plot of 1-dimensional power spectral densities computed from AFM data. The dashed (dark-orange) line indicates the q^{-4} scaling that is expected for the experimental curves.

4.3 Optical properties

In this section, we present the experimental characterization of the spectral scattering efficiency of the textures shown above. Then, we compare these observations by taking into account the effect both of the RMS roughness and of the spatial correlation length of the surface features. This allows to rationalize the interplay between surface morphology and optical response of the textures.

The optical properties of the substrates have been investigated using the apparatus described in chapter 3 to calculate the haze and to measure the angle-resolved scattering. Since the interest is in the scattering properties in transmission configuration, we let the light beam pass through the sample from the flat surface to the textured one (see figures 3.1 a, b and figure 3.2).

Haze in transmission

The haze is the ratio of the diffuse scattered light intensity (i.e., excluding the direct component) to the total one. This physical quantity is measured by an integrating-sphere setup in a Cary 600i spectrometer, as described in section 3.1. In particular, we use the haze to get information about the fraction of transmitted light scattered off the incident direction, which has a higher probability to be trapped into the absorber layer of the SC by starting a longer optical path. The results for the haze in transmission are displayed in figure 4.5. The curve of the nanotextured glass (in red) is higher than the one of the Asahi-U reference (in blue). This indicates a strong improvement in scattering property on the whole wavelength range of interest for Si photovoltaic applications, i.e. from about 350 nm to 1000 nm. We find the reason for the increased scattering efficiency in the peculiar distribution of the morphological parameters of our textured interfaces shown in figure 4.4. Actually, the 1D-PSD curve relative to Zone 2 is characterized by surface features sized in the range of light wavelengths.

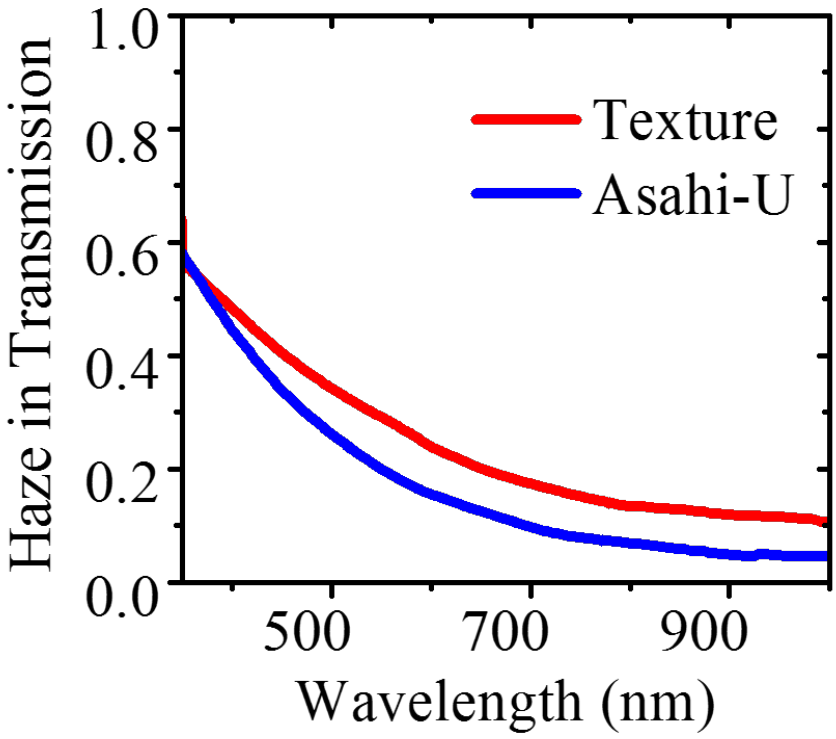

Figure 4.5: The haze in transmission measured on the our nanotextured substrate, in red, and on the Asahi-U sample, in blue.

Angle resolved scattering

The ARS measurements have been performed in transmission configuration using the home-made experimental setup described in 3.2. This allows a detailed examination of scattering properties for the different morphological regions of our sample. The orientation of the collection plane is not relevant for the Asahi-U sample, because of the isotropy of the texture. On the other hand, in the case of the self-organized nanopatterned substrate, we choose to collect light in the scattering plane orthogonal to the 1-dimensional ripple axis.

The graph of figure 4.6 shows the ARS data obtained in Zone 1, Zone 2 and Zone 3 of the nanotextured sample and on the reference Asahi-U texture using monochromatic light at 600 nm wavelength. The data are plotted by

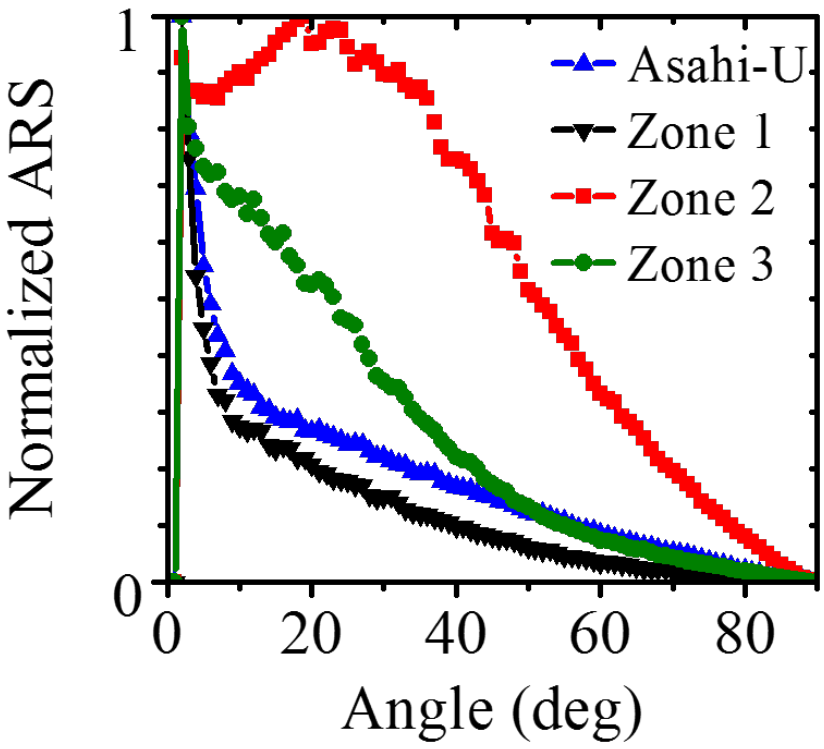

Figure 4.6: The ARS in transmission at a wavelength $\lambda = 600$ nm normalized at the maximum, discarding the specular direction. The normalized intensity of the scattered light is plotted as a function of the scattering angle. In the graph, 0 deg corresponds to the specular direction in transmission and 90 deg is the direction parallel to the scattering surface. The black, red and green dot-line correspond to the three different morphologies obtained in different regions named Zone 1, Zone 2 and Zone 3, respectively, of the investigated sample. The blue dot-line refers to the Asahi-U texture.

discarding the values measured at 0 degrees (placing them at zero) and each curve is normalized to the respective maximum value. The ARS curve of Zone 2 presents a smooth peak around 20 deg, which spreads in a wide angular range up to about 40 deg, and rapidly decreases at higher angles. For the other two morphologies of our sample, where the scattering efficiency is affected by the lower aspect ratio of the nanostructures, the ARS shows no maximum besides the one coming from specular direction and the relative curves (labelled Zone 1 and Zone 3 in figure 4.6) decay monotonically similarly to the Asahi-U ones.

These experimental results outline the superior scattering property of Zone 2 in transmission with respect to the Asahi-U reference substrate. For this reason, the interesting scattering property of Zone 2 are further investigated by measuring the full ARS in transmission at several wavelengths, see figure 4.7. The curves are plotted in logarithmic scale in order to display both the

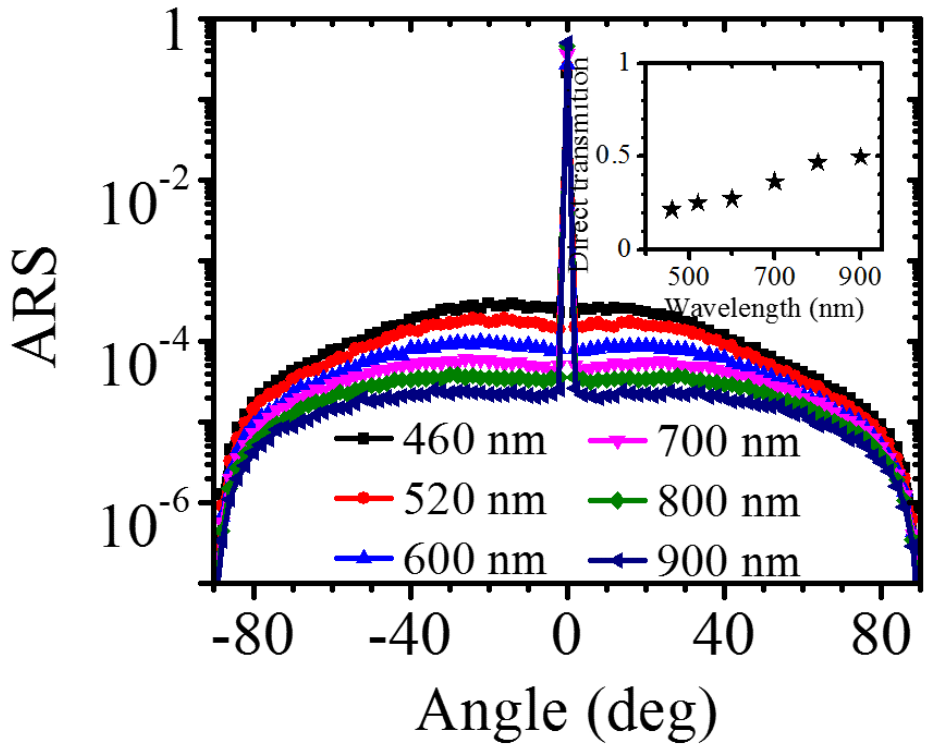

Figure 4.7: The ARS measured in transmission on Zone 2 at several wavelengths. The logarithmic scale allows to appreciate the spread between the specular component of the scattered light and the diffused one. In the inset, the transmitted intensity in the specular direction is plotted versus the wavelength.

specular and off-specular intensities. The latter decrease by almost one order of magnitude when the wavelength of detected light λ increases from 460 nm to 900 nm. At the same time, the transmitted intensity measured along the specular direction increases monotonically from about 0.22 to 0.5 times the incident intensity at $\lambda = 460$ nm and at $\lambda = 900$ nm, respectively. We interpret such a behaviour taking into account again the typical lateral scale of pattern corrugations λ^*, which reads approximately 500 nm in Zone 2 from 1D-PSD curve (see figure 4.4). So light wavelengths shorter than λ^* are more efficiently scattered, while for wavelengths exceeding λ^* the direct transmission becomes increasingly important.

The partial short-range ordering in the texture shown by the ACF profile of Zone 2 (see in figure 4.3) suggests that we should expect coherence phenomena in observing light scattering. Actually a sort of diffraction effect emerges along preferred angular scattering directions. This is highlighted by comparing the ARS curve on Zone 2 with the cosine function representing Lambertian diffusion, see figure 4.8. Notice the presence of two symmetrical lobes around 30° on top of the Lambertian background. In order to prove the coherent nature of these symmetrical lobes, in figure 4.9 we show the ARS curves measured on Zone 2 at different wavelengths. Each curve is normalized to its own maximum value discarding the specular point as in figure 4.6. Also in this case we notice the clear presence of the additional scattering lobes. The angular positions of the maxima are indicated by the black boxes. We notice the shift of the maxima toward larger angles on increasing wavelengths, which is compatible with a diffractive (coherent) effect in the scattering of light.

The angular positions of the scattered intensity peak can be simply understood in the framework of grating diffraction (without aiming at reproducing the intensity profile), as depicted in the sketch in figure 4.8. This is reasonable since the pseudo periodic nature of the ripple structures is confirmed by the secondary fringes in the ACF profile of figure 4.3, indicating that lateral coherence is strong even for distances exceeding several μm.

We recall that the autocorrelation length in Zone 2 reads W = 800 nm and, in a simplified representation, this can be considered as the pitch of a one dimensional diffraction grating with an associated wavenumber $G = W^{-1}$ lying in the plane of the grating. Therefore, light impinging at normal incidence

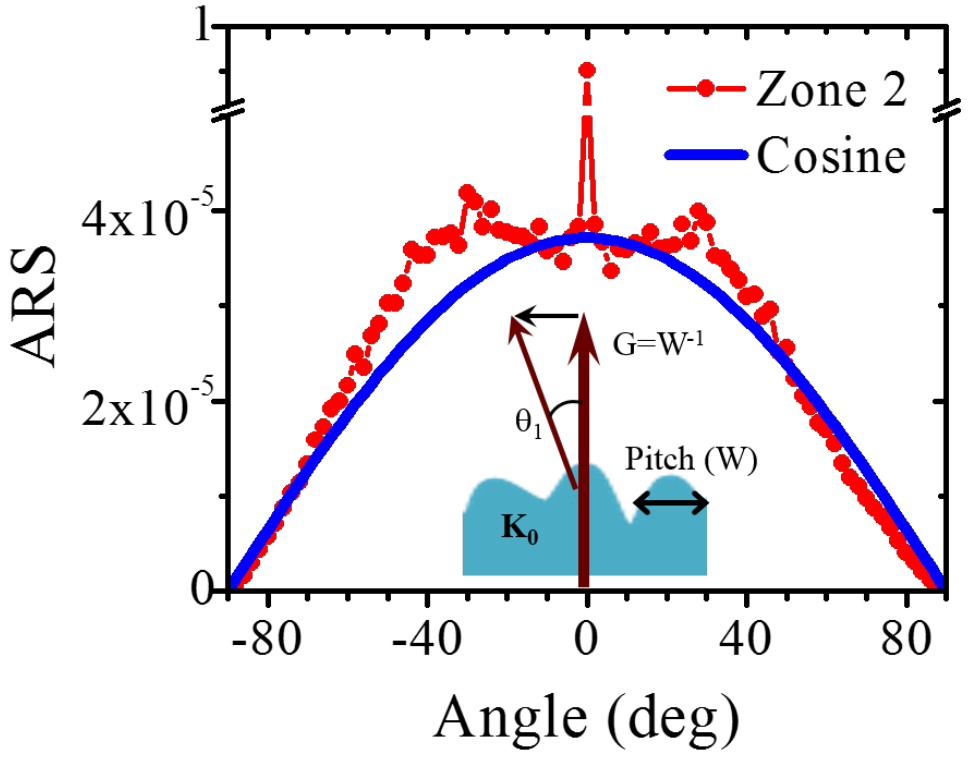

Figure 4.8: ARS curve measured on Zone 2 at $\lambda = 800$ nm (red dot-line) and the cosine function representing Lambertian diffusion (blue line). The latter is normalized in order to have the same scattered intensity for both curves. The sketch illustrates the diffraction mechanism giving rise to preferred spatial directions of the scattering pattern.

from the flat side travels into the glass slab with a refractive index of 1.5 and, after crossing the grating, exits at an angle θ_1 due to a momentum exchange G with the glass grating (first scattering order). The position of the dominant scattering peak can thus be calculated for different wavelengths according to the following relation:

$$\theta_1 = sin^{-1}\left(\frac{\mathrm{G}}{\mathbf{K}_1}\right) = sin^{-1}\left(\frac{\lambda}{\mathrm{W}_{n_{\mathrm{eff}}} \cdot n_{\mathrm{glass}}}\right) \tag{4.3}$$

where $\mathbf{K}_1 = n_{\mathrm{glass}} \cdot \mathbf{K}_0$, while $n_{\mathrm{eff}} = 1.2$ represents an air-glass effective medium, which accounts for the weighted average of the sub-wavelength structures with filling factor of 0.5 [88]. The predicted angular positions of the maxima indicated by boxes in figure 4.9 agree very well with the measured ARS maxima. Therefore, we can conclude that the angular distribution of

the scattered intensity measured on Zone 2 is a combination of an incoherent scattering background, which is related to the uncorrelated roughness, and a coherent component, that follows from the pseudo-periodic nature of the nanotextured surface. The resulting profile of ARS overcomes the Lambertian distribution (with the same fraction of diffused light) in a range of scattering angles. For this reason we may say that it follows a *super-Lambertian* behavior.

The observations of wavelength- and angle-dependence of scattering therefore reflects the morphological features of the textured substrate. This study is a good example of how the combination of randomness and order gives rise to peculiar features in the scattering properties of light that are of interest for light management and light trapping, especially for photovoltaic applications.

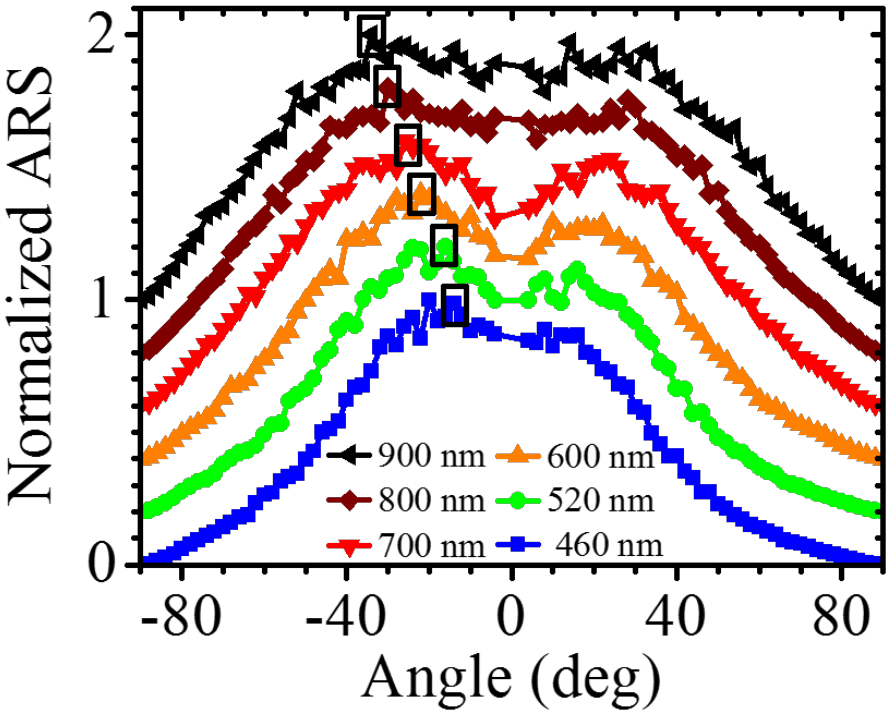

Figure 4.9: ARS curves measured on Zone 2 at different wavelengths without the specular point and normalized to their own maximum value. For the sake of clarity a vertical offset 0.2 is placed to stack the curves. The black boxes highlight the angular positions of the maxima of the scattering lobes calculated for the investigated wavelengths (as explained in the text).

Chapter 5

Vertically aligned silicon nanowires

Solar cells (SCs) are usually fabricated with the optical active layer embedded between the two electrodes according to a vertical scheme, where the photon absorption and the charge collection occur along the same axis (see figure 5.2 a). In this architecture, the thickness of the absorbing layer is a crucial parameter for the SC efficiency. In fact, the photon absorption increases with the thickness, because of the negative exponential trend of light intensity with the optical path. On the other hand, the charge collection efficiency decreases with the thickness, because the longer the path to reach the electrodes the greater the charge recombination probability. Therefore, a trade off between these two mechanisms results in search of the optimal thickness of the active layer. This concept is well resumed by the aphorism *electrically thin and optically thick*, which aims for the maximization of SC efficiency. In the previous chapter we have shown how a light-trapping scheme realized by means of a high aspect ratio and a spatial correlated texture allows one to reduce the minimal permitted thickness in this issue [19, 26]. However, a further reduction of the distance between electrodes may be possible by resorting to an alternative architecture, in which the optical axis does not lie on the same direction of the electrical one (see figure 5.2 b). This principle is shown in figure 5.1, where a prototype SC device exploits the radial collection in nanowire materials, whose unidimensional aspect ratio allows a fast charge harvesting, while the light is absorbed along the entire length of nanowires [58, 89].

Furthermore, the radiation propagates by multiple scattering into structure made of densely aggregated nanowires and an enhanced absorption of light can occur, as already demonstrated for carbon-nanotubes and black silicon [90, 91].

In this chapter, we report on the investigation of the strong light absorption and enhanced Raman emission of light in a nanostructured material made of ultra-thin and vertically aligned silicon nanowires (Si NWs) arranged in a 2D fractal array. The latter is obtained via auto-organized lithographic process [92]. Despite their ultra-small dimensions (only a few microns long with a diameter of few nanometers), the investigated NW samples show a very high light-trapping across the entire visible and near-IR range, which is driven by multiple scattering inside the structure. We demonstrate that the strong absorption of light and the enhanced Raman scattering are strictly correlated to the length scales at which the refractive index primarily fluctuates [63].

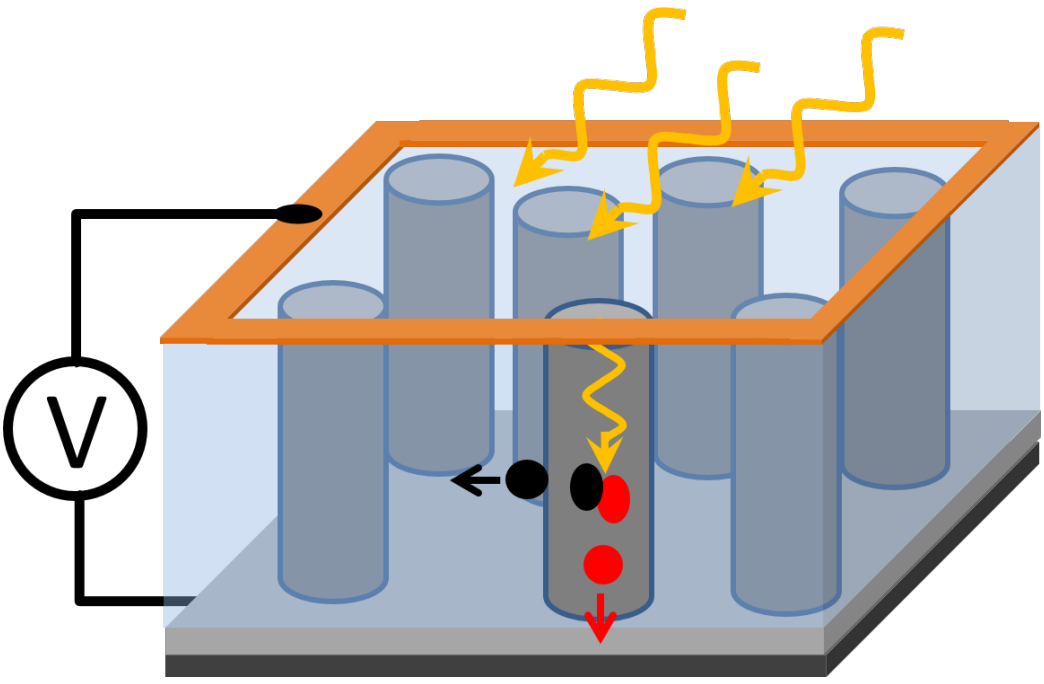

Figure 5.1: Schematic representation of charge radial collection in a prototype SC device based on nanowire materials.

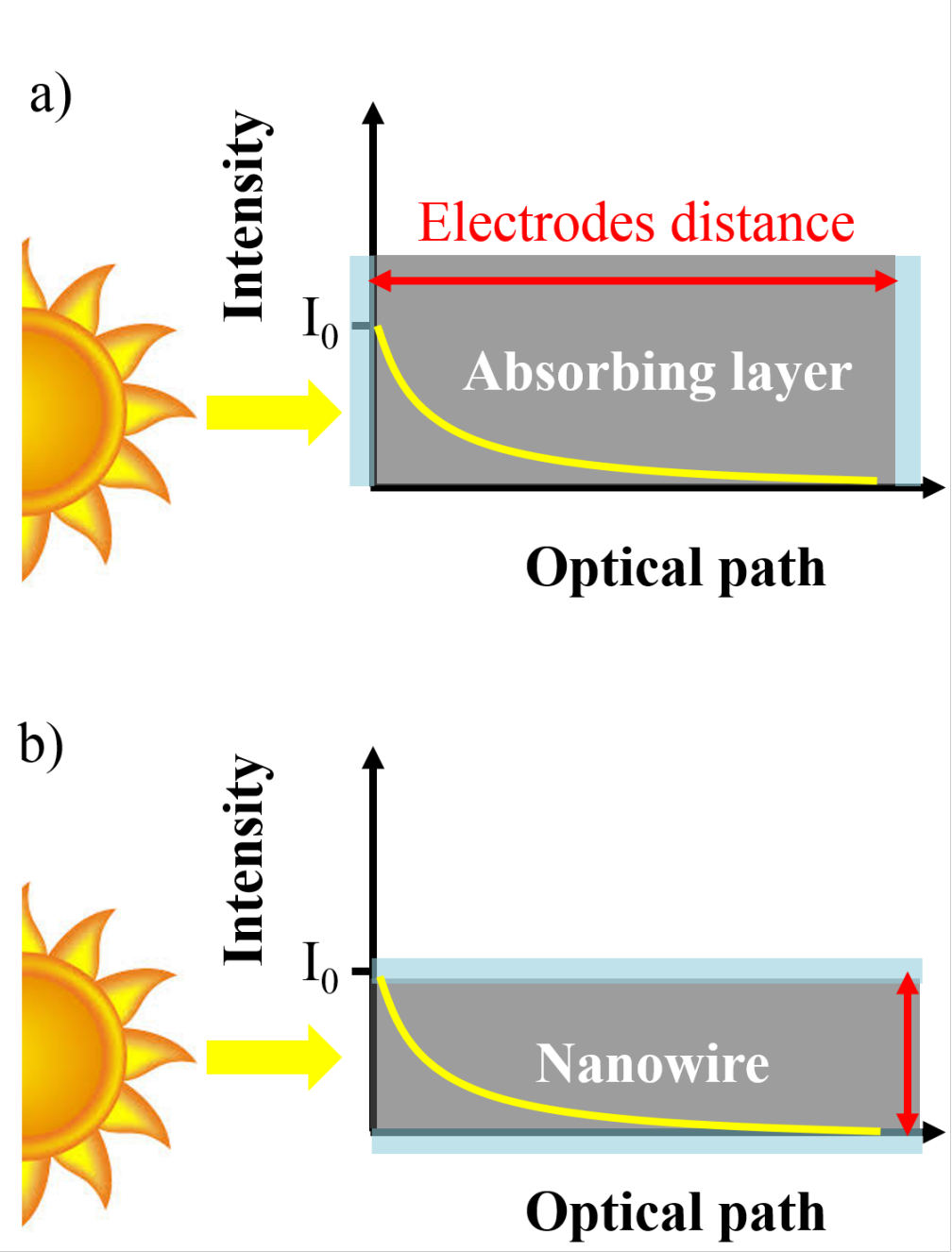

Figure 5.2: A schematic representation of the light intensity absorption into the absorber media of the solar cell. In a) the classic planar scheme and in b) the nanowire architecture. Notice how the distance between the electrodes is proportional to optical path in the first case, while it is independent in the second one.

5.1 Fabrication and morphology

The silicon NWs that have been studied in this work are fabricated by metal-assisted wet etching process, which is performed on Si substrates consisting in single crystal n-type doped wafers with orientation (111) and (100) for samples 1 and sample 2, respectively, and with resistivity of 1.5 Ω·cm and with thickness of 540 μm. To produce a clean and oxide-free Si surface, the wafer are oxidized by UV light exposure and then the oxide is removed by dipping them in solution of 5% hydrofluoric acid (HF). After this cleaning step, a thin gold layer with an equivalent thickness of 2 nm is deposited onto the Si substrates via electron beam evaporation (electron beam evaporator from Kenosistec s.r.l., Binasco MI, Italy) using high purity (99.9%) gold pellets. The final gold thickness measured by Rutherford backscattering spectrometry corresponds to a surface density of 10^{16} Au atoms per cm^2. The sample surface results with patches of uncovered silicon area surrounded by gold clusters. The Si NWs are obtained by etching samples in an aqueous solution of HF (5 M) and H_2O_2 (0.44 M). Notice, since the metal promotes the Si oxidation by injecting holes and the presence of HF determines SiO_2 removal, the Si NW formation occurs in the regions which are not covered by the metal (see figure 5.3). For this reason the metal deposition is made to achieve a discontinuous covering. Finally the residual Au is removed via a KI dip [63].

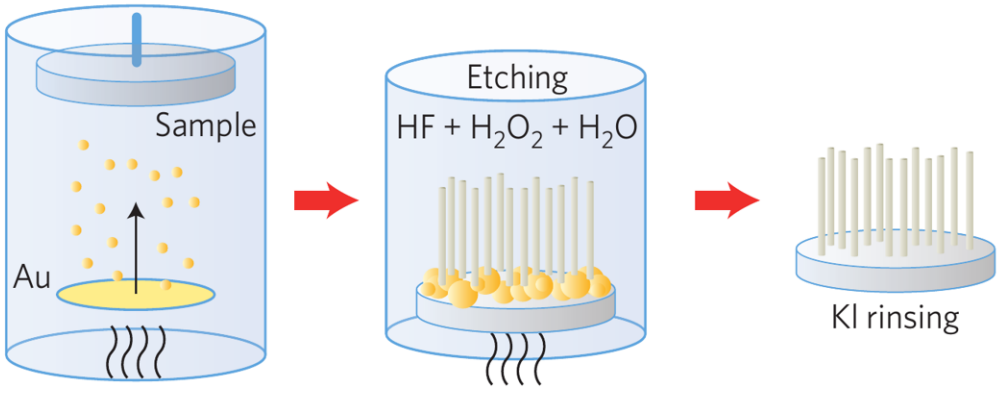

Figure 5.3: Sketches of preparation stages of the Si NW forests by means of the metal-assisted wet etching process. From left to right, the deposition of thin gold layer as metal precursor, the silicon erosion by wet etching and the final result of nanowires free from gold particles [5].

This new fabrication method proposed by Irrera [92] replaces the catalytic metal salt ($AgNO_3$) present in the etching solution avoiding the dendrite residues, whose removal could damage the NWs. Therefore morphology of the metal layer and the etching solution determine the formation of NWs.

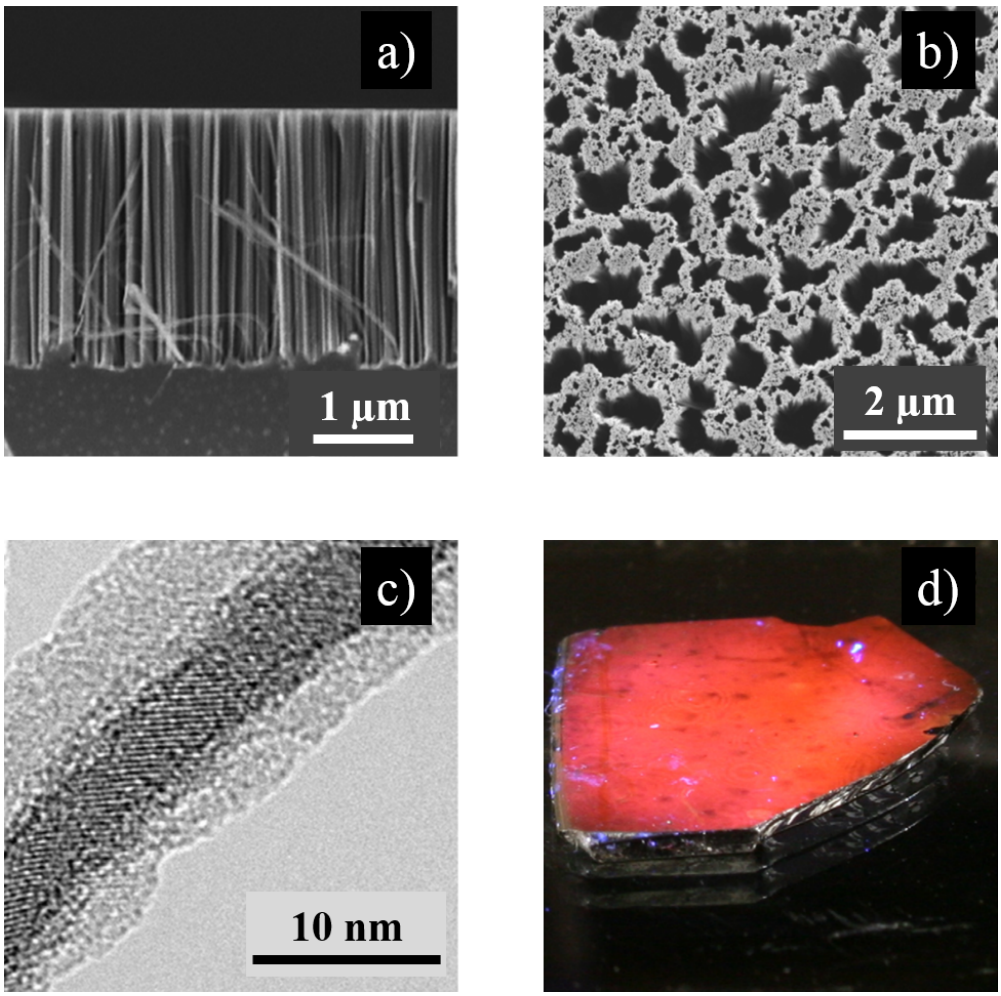

Figure 5.4: Si NWs obtained by the metal-assisted wet etching technique. The scanning electron microscopy, a), cross-section and, b), plan view SEM images of the Si NW array obtained using Zeiss Supra 25 (Oberkochen, Germany). c) The high resolution transmission electron microscopy image of a single NW, the Si core and the native silica shell are distinguishable. d) Photograph of a Si NW sample having an area of about 1 cm^2 excited by the 364 nm line of a fully defocused Ar^+ laser beam showing a bright red photo-luminescent emission clearly visible by the naked eye [92].

That allows an effective control of the structural properties obtaining the formation of very thin Si NWs. Moreover this top-down lithography is advantageous with respect to the vapour-liquid-solid (VLS) mechanism, because the lattice of crystal Si NWs is free from metal contaminations, which are typical of the bottom-up growth mechanisms. That opens new prospectives in terms of quantum confinement effects, such as the light emission at room temperature shown by our Si NW samples under both optical and electrical excitation (see figure 5.4 c and d) [92].

We characterize the structure and the morphology of the NW samples by means of scanning electron microscopy (SEM) and of transmission electron microscopy (TEM) techniques. From the latter we estimate a value of 7 ± 2 nm for the NWs diameter (see figure 5.4 c). From the cross-section SEM image (shown in figure 5.4 a) the sample appears as a dense forest of vertically aligned NWs, all having the same length (≈ 2.6 μm), while the analysis of the top-view SEM images at increasing magnifications reveal a surface coverage of $\approx 60\%$ for all of the three different magnifications in figures 5.5. That scalar invariance in the filling factor (NWs over air) is an interesting self-similarity properties in the planar morphology of NW forest [63, 92].

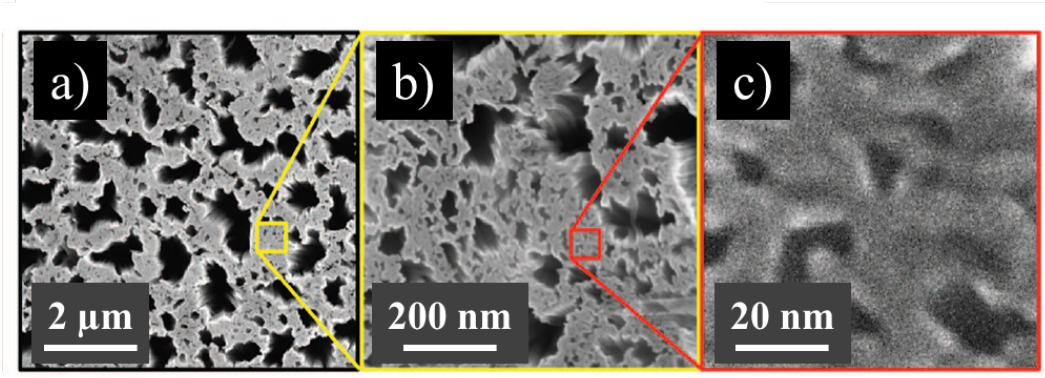

Figure 5.5: Plan view SEM images of a Si NW sample obtained at three different magnifications (25 k×, 250 k× and 2500 k×). Panel b) is the higher magnification of the sample area inside the yellow square in panel a), and panel c) is the higher magnification of the sample area inside the red square in panel b)[63].

5.2 Disorder and lacunarity

The scale invariance in the 2D arrangement of the Si NWs is due to the structure of thin gold layer, which is close to the percolation threshold because of the filling fraction of 54.6%. Since an infinite cluster close to the percolation threshold is a fractal object [93], we expect a fractal morphology for the gold layer. Infinite fractals have very interesting light scattering features, because they are characterized by the absence of a characteristic length for the inhomogeneities. In particular a random fractal pattern is characterized by a self-similarity for which the structural heterogeneities are correlated on all length scales. Moreover fractals are known as systems promoting electromagnetic field localizations because the lack of translational invariance leads the structure to spatially localize the running waves. An inhomogeneous localizations of the electromagnetic field can happen in these structures and both spatially delocalized and localized modes coexist. This is similar to the observation made in Refs. [94, 95], although in that case plasmonic effects should also play a role and lead to tighter localization. Therefore the intensity of the electromagnetic field can be enhanced with a fractal structure.

In other word, fractal textures are correlated on all length scales. Whatever the effective wavelength $\lambda_{eff} = \lambda/n_{eff}$ propagating inside them, there will always be the possibility to match the length scale where the refractive index fluctuates and thus the possibility to generate a stronger emission properties in the system [63]. Therefore the wavelength of incident radiation matchs always the inhomogeneity size. That enables strong light scattering as aforementioned in chapter 2 [96]. However, our sample deviates from the structural characteristics of a infinite fractal, having a cutoff value in the maxima dimensions of holes in the range of 1 μm, see figure 5.5. For this reason we expect to observe fascinating scattering properties in a finite range of wavelength.

Fractal dimension

The fractal arrangement of the Si NWs in our samples is also confirmed by calculating the fractal dimension of the structures D_F. We used a top-down approach to calculate D_F by sectioning in square boxes an highly resolved low-magnification SEM image of the planar arrangement of the NWs, as shown in the inset of figure 5.6 a).

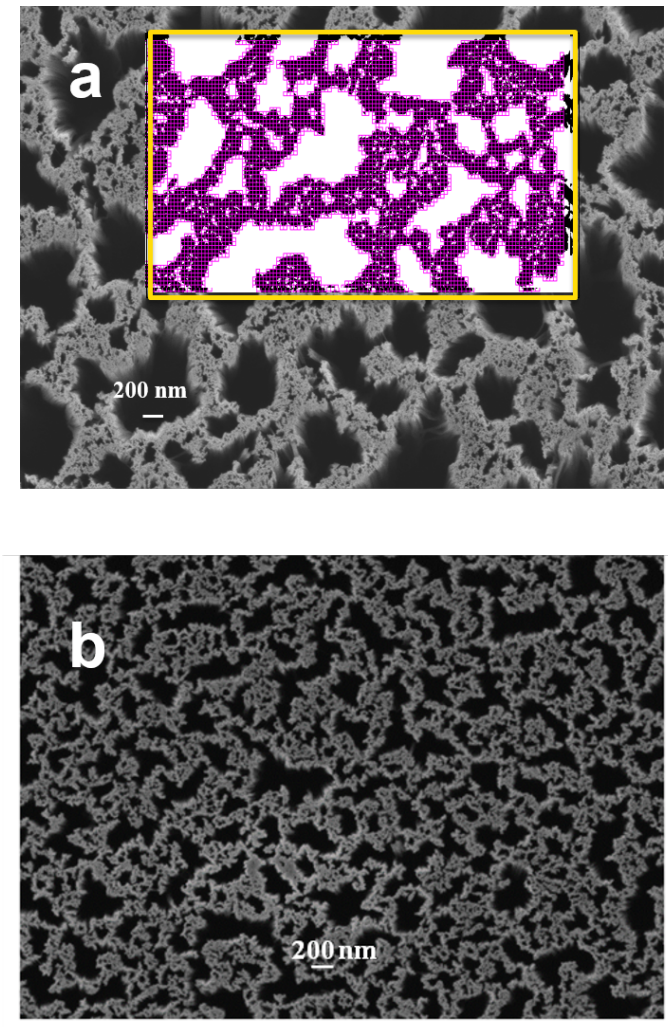

Figure 5.6: Characterization of 2D random fractal structures of Si NWs. Si NW samples 1 (a) and 2 (b) plan view SEM images used for Fraclac analysis. Details of the analysis with sectioning in square boxes in the reduced sample portion are shown in the inset of panel a. Note that the pixel size is 6.7 nm [63].

We evaluated the occupied pixel number N (the dark pixel of the inset of figure 5.6 a) as function of the square box dimension ϵ, according with the relation [63]

$$N \propto \epsilon^{D_F}. \tag{5.1}$$

The presented method yields the so-called *box-counting fractal dimension* [97]. The analysis was performed by using *ImageJ* software and the *Fraclac plugin* [98]. We obtained a value of fractal dimension $D_F = 1.87 \pm 0.02$ for sample

1 and $D_F = 1.92 \pm 0.02$ for sample 2 from the slope of the curve $ln(N) = -D_F \cdot ln(\epsilon) + C$ shown in figure 5.7 a). These values confirm the dense planar arrangement of the Si NW forest, as expected starting from a 2D percolation for an invasion cluster of gold [99].

Lacunarity

The gold layer morphology is imposed on the silicon substrate as a negative mask during the wet etching procedure. Therefore the empty spaces (gaps) in between of Si NWs are arranged with the same structure of the gold deposition morphology. The fractal parameter that takes into account both the gaps and the heterogeneity of the structure is the lacunarity. If there are large holes, the fractal has high lacunarity. Since the lacunarity is related to the deviation of fractal from translational invariance, it is expected to be high especially in random fractals. The calculus of lacunarity is based on variation in pixels[1] density at different box sizes of SEM images. The values of lacunarity λ are defined for each grid of dimension ϵ, by relation:

$$\lambda(\epsilon) = \left(\frac{\sigma(\epsilon)}{\mu(\epsilon)}\right)^2 + 1 \tag{5.2}$$

where $\sigma(\epsilon)$ and $\mu(\epsilon)$ are the standard deviation and the mean number of pixels, respectively, calculated on a series of grid of dimension ϵ. The values of $\lambda(\epsilon)$ calculated for both samples are plotted in figure 5.7 b). Sample 1 presents heterogeneities over a wide-length range, as pointed out by spreading of λ values at fixed ϵ. The maximum of lacunarity is revealed on the scale of $150 \div 200$ nm. That is the range with the strongest fluctuations of refractive index in the fractal structure and we expect exceptional scattering properties in this range of effective wavelength. For sample 2 the lacunarity increases at very small length scales following a monotonic trend. This is the result of a different morphology of the Au thin film probably due to the different crystallographic orientation of the silicon substrate (100) with respect to that of sample 1 (111).

[1]The black ones in the inset of figures 5.6 a).

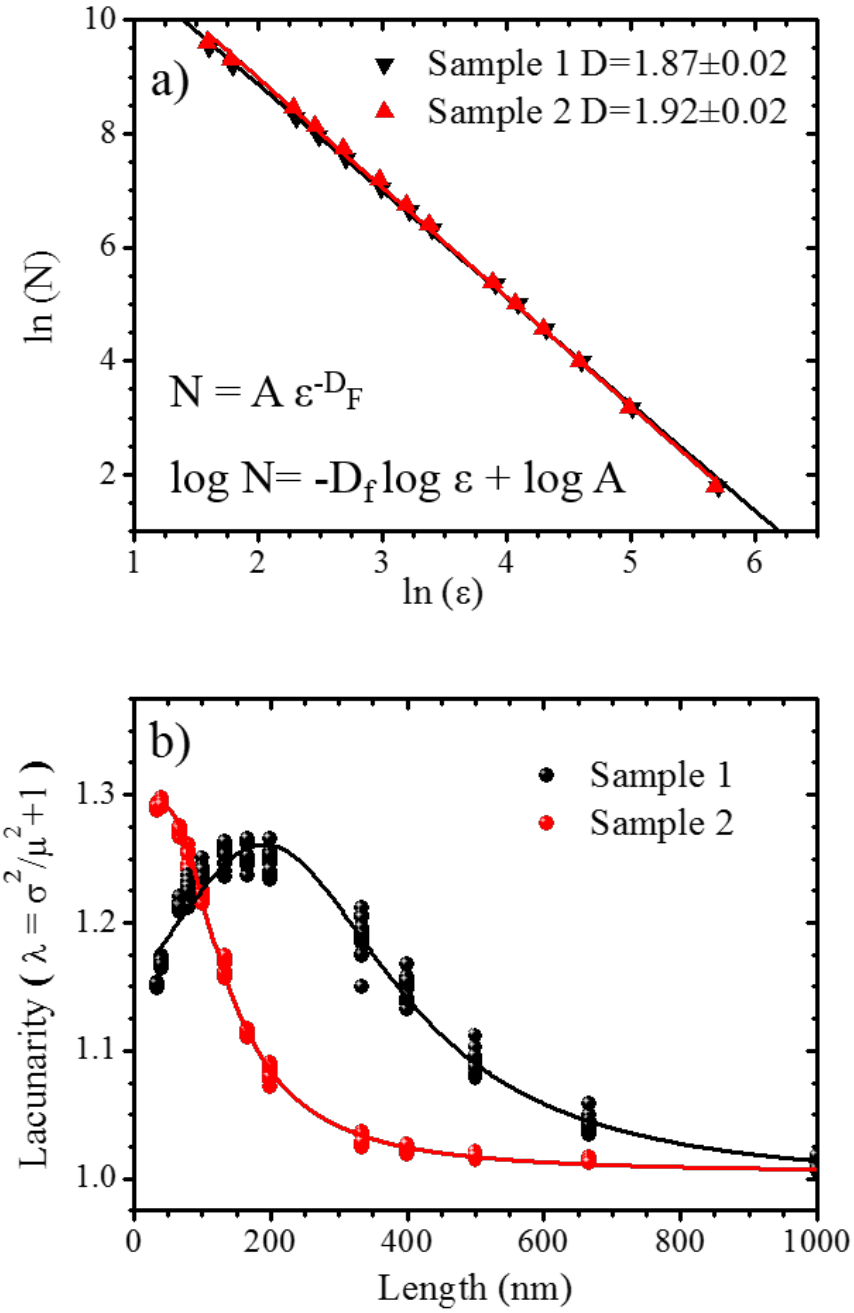

Figure 5.7: The fractal dimension (a) and lacunarity (b) plots obtained form the analysis of SEM images shown in figure 5.6. In a), the number of boxes N occupied by NWs (the dark pixels in the inset of figure 5.6 a) is plotted in a log-log scale as a function of the box size ϵ. Therefore, the slop of the linear fit gives the value D_F of fractal dimensions of the NW samples, according to equation 5.1. In b), the plot of the calculated values of lacunarity *vs* length $= \epsilon \times 6.67nm$. Note that the lacunarity analysis is halted at 33 nm [63].

5.3 Anti-reflection properties

The optical property of the two fractal samples of Si NWs are investigated by total transmission and reflection spectroscopy techniques, which are described in chapter 3.1. We expect a strong scattering strength in the visible and IR range, because of the fractal properties discussed in the previous section. To better appreciate the spectral features arising in our sample, we compare them with both the optically flat side and rough side of a Si wafer. The total diffused (integrated) reflectance is shown in figure 5.8. For the faces of Si wafer, the measured values is that expected from the average angle-dependent Fresnel coefficients at the Si–air interface. The total integrated reflectance of the Si NWs deviate from the single scattering (reflection)behaviour dropping to around 1% across the entire spectrum (visible-NIR range) of wavelengths below the Si bandgap ($\approx$ 1.1 μm). These experimental results evidence a broadband light-trapping by Si NW forest, which justifies the black appearance

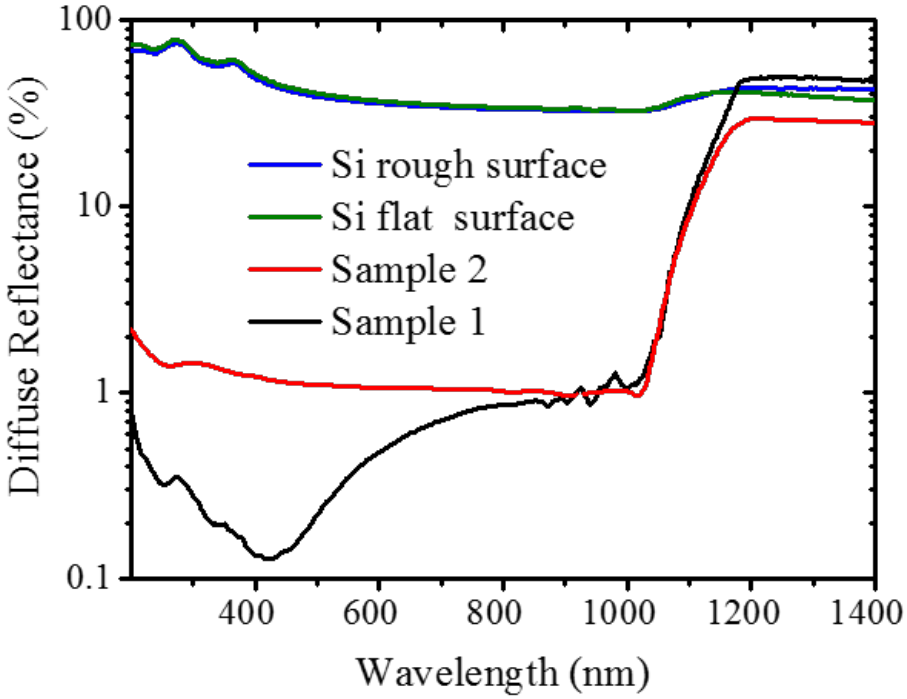

Figure 5.8: The total diffused reflectance of sample 1 (black lines) and sample 2 (red line) and of the flat surface and of the rough surface of c-Si wafer (green and blue lines, respectively) [63].

of sample surfaces. Notice, in many black silicon materials, a similar broadband antireflection behaviour is enabled by a graded index profile along the height of the NWs [91]. However, as shown in figure 5.4 a), the constant cross section and the perfect vertical alignment of our Si NWs should lead to a constant average index of the NW layer along the vertical direction. Moreover, the large reflectance observed just above the Si bandgap in the IR region and the sharp decrease in the absorbing visible range are incompatible with a graded index profile, which would give a very smooth and low reflectivity across the Si bandgap as reported for black Si [100].

To clarify the physical phenomena leading such strong light absorption in our samples, we measure the direct transmittance of our samples, reported in figure 5.9. A very strong suppression of the transmittance to values below 1% is observed for both Si NW samples at IR wavelength above the bandgap.

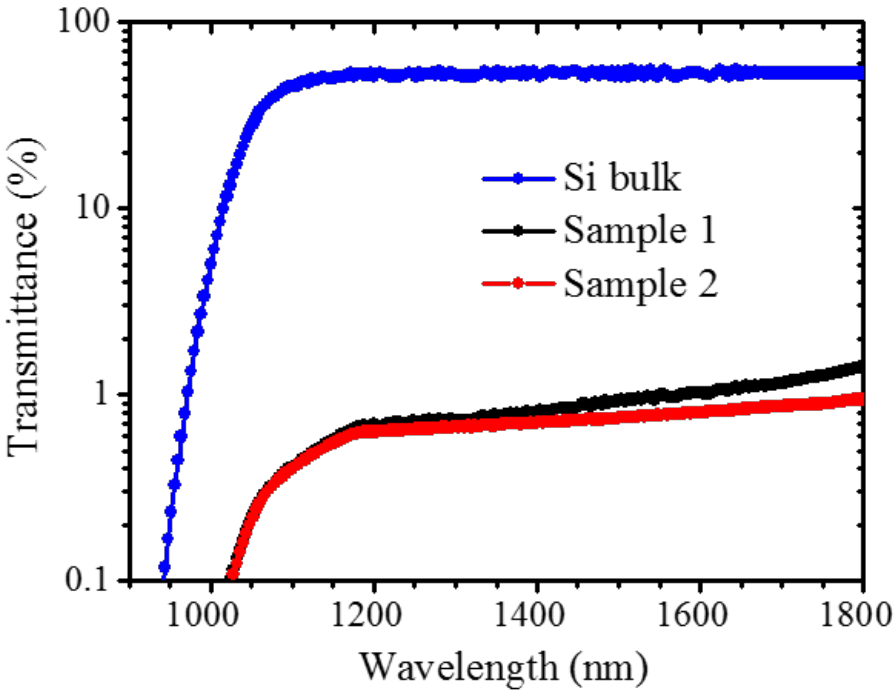

Figure 5.9: Direct transmittance, by excluding the diffuse component, of samples 1 and sample 2 obtained in a polished (optically flat) back surface (black and red dots, respectively) compared with that of a wafer bulk c-Si (blue dots). Note only the data in Si transparency range are shown, because the values drop to zero across the entire absorbing range [63].

That also is incompatible with an antireflection effect by the NW layer, which would increase the transmittance compared with bulk Si instead of suppressing it. According with these observations, we definitively reject the idea of radiation coupling in Si bulk by impedance gradient in our samples. However the visible light is neither reflected nor scattered out of the Si NW layer. We hypothesize that light is strongly diffused within the NW array and remains mostly trapped in the NW layer by multiple scattering processes until it is eventually absorbed. Indeed, the single NW could not efficiently scatter the visible light because of the ultra-small average diameter (a few nanometers) [92]. The key role is played by the particular 2D random fractal texture of our NW forest, whose the peculiar density variation of Si NWs and voids on the wavelength scale between 10 nm and 1 μm (as shown in figure 5.5) activates the light scattering processes. So the light propagation is preferentially in-plane, because the refractive index fluctuations are across the 2D planar structure of NW array. Moreover, observing in detail the reflectance spectra of sample 1 in figure 5.8, we notice a broad minimum approaching 0.1% around 428 nm of wavelength. That indicates an over-trapping of light in NW structure at an effective wavelength of $\lambda_{eff} = 192$ nm in the NW forest, with the refractive index $n_{eff} = 2.23$, as calculated by the Bruggeman mixing rule assuming a composition made of 40% air voids, of 40% silicon and of 20% native oxide on the Si NWs [101, 102]. This value of effective wavelength falls into the length range at which the lacunarity of sample 1 shows the maximum value (see figure 5.7), corroborating the hypothesis of strong scattering in-plane of NW array. The light should travel for much longer path than the thickness of the NW layer to reach the 99% extinction of intensity, because the photon absorption is by c-Si of NW core, which is just the 40% of the total volume of thin layer. Therefore, to reach the over-trapping of light, the photons should propagate for a relative long path into the thin plane by multiple scattering processes [103], which occur in strong scattering media folding the light propagation in a random walk (see section 2.3). That conclusion is confirmed also by the CBS experiments, which we have performed to assess the scattering strength of our samples 1 (see section 6). The analysis of this CBS cone gives a value of transport mean free path $l_t \approx 160$ nm, which is typical of very strong scattering materials [63, 104].

5.4 Raman enhancement

As discussed above, whatever the optical frequency propagates into the fractal array of Si NWs, its effective wavelength ever matches the fluctuation length of the refractive index. That causes inhomogeneous localizations of the electromagnetic field into the NW samples. For this reason, the intensity of the electromagnetic field is enhanced and strong scattering emissions arise from our samples. Our Si NW samples exhibit efficient room temperature photoluminescence (PL) due to quantum confinement effects, as reported recently [5, 92]. In particular, the PL emission in sample 1 is strongly evident, even by the naked eyes (see figure 5.4 d). Figure 5.10 shows the optical emission spectrum obtained by exciting the investigated sample with the 488 nm line of a laser. The PL band, peaking at 690 nm, is clearly visible. However, a further dominant feature is represented by an exceptionally strong first-order Si Raman peak at 500.7 nm (≈ 520 cm^{-1} of Raman shift).

To reveal the nature of this intense Raman signal, we excited samples 1 and 2 at different laser wavelengths and compared the spectra with those

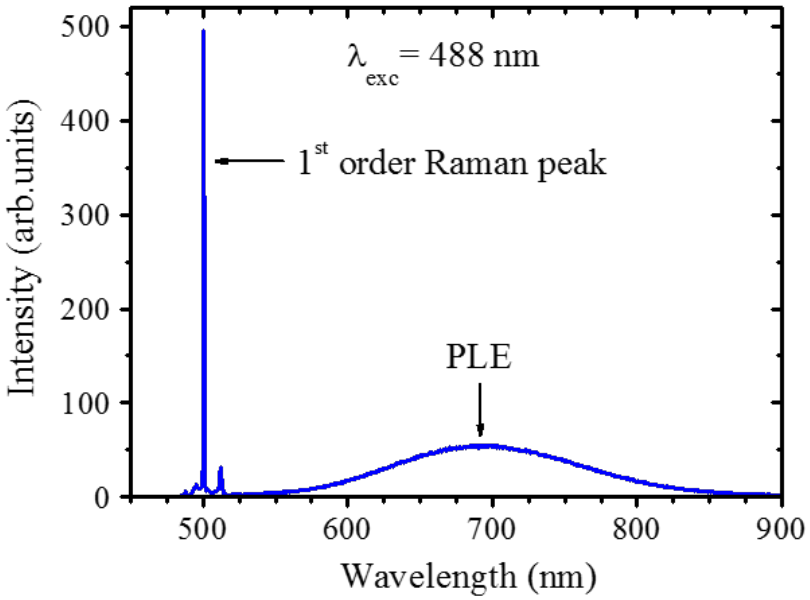

Figure 5.10: The backscattered Raman light and the PL emission from the Si NW fractal array of sample 1 at an incident laser wavelength of 488 nm with a power of 20 mW and and a spot diameter of 100 μm [63].

of a single crystalline Si (c-Si) sample identical to the one used to fabricate the NWs. The Raman spectra are acquired in back-scattering configuration by means of a *HR800 Horiba—Jobin Yvon* spectrometer equipped with an a 100× objective of 0.9 of numerical aperture in air, while the Rayleigh light is filtered by means of an optical density $OD = 5$. Figure 5.11 shows Raman signals from sample 1 (blue curve) and bulk silicon used to fabricate the NWs (red curve), which are reported in the same graph for the sake of comparison. The spectrum of Si NWs shows at same time a clear enhancement for first and second orders of Raman light and a reduction of the Rayleigh light. These further dominant scattering feature is already experimentally proved in similar structures by different groups [105, 106, 107].

The quantitative estimation of Raman enhancement (RE) comes from the ratio between the Raman peak integrated intensities of Si NWs and those of bulk silicon in the same experimental conditions. Notice that the amount of material excited by the laser spot is not the same for NWs and bulk silicon, because of the presence of the air voids between NWs and the silicon oxide shell around each NW (40% and 20% respectively). Therefore we have to normalize the RE to the probed volume of sample (REV) considering only 40% of silicon.

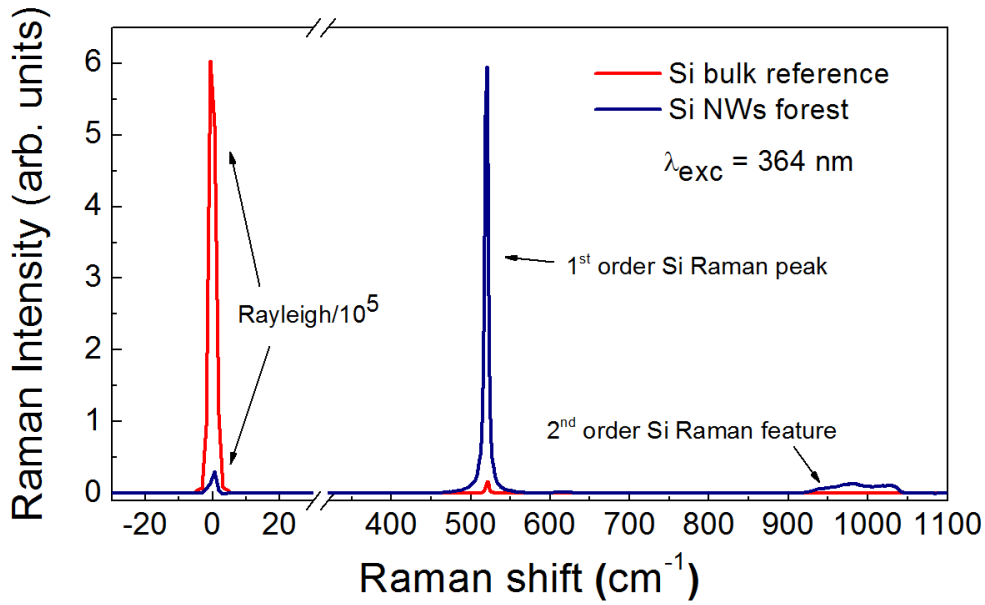

Figure 5.11: Raman spectrum of Si NW array (red line) and of bulk crystalline Si reference (blue line). The Raman signal of NWs is clearly enhanced for both first (at ~ 520 cm^{-1}) and second orders (at ~ 1000 cm^{-1}) [66].

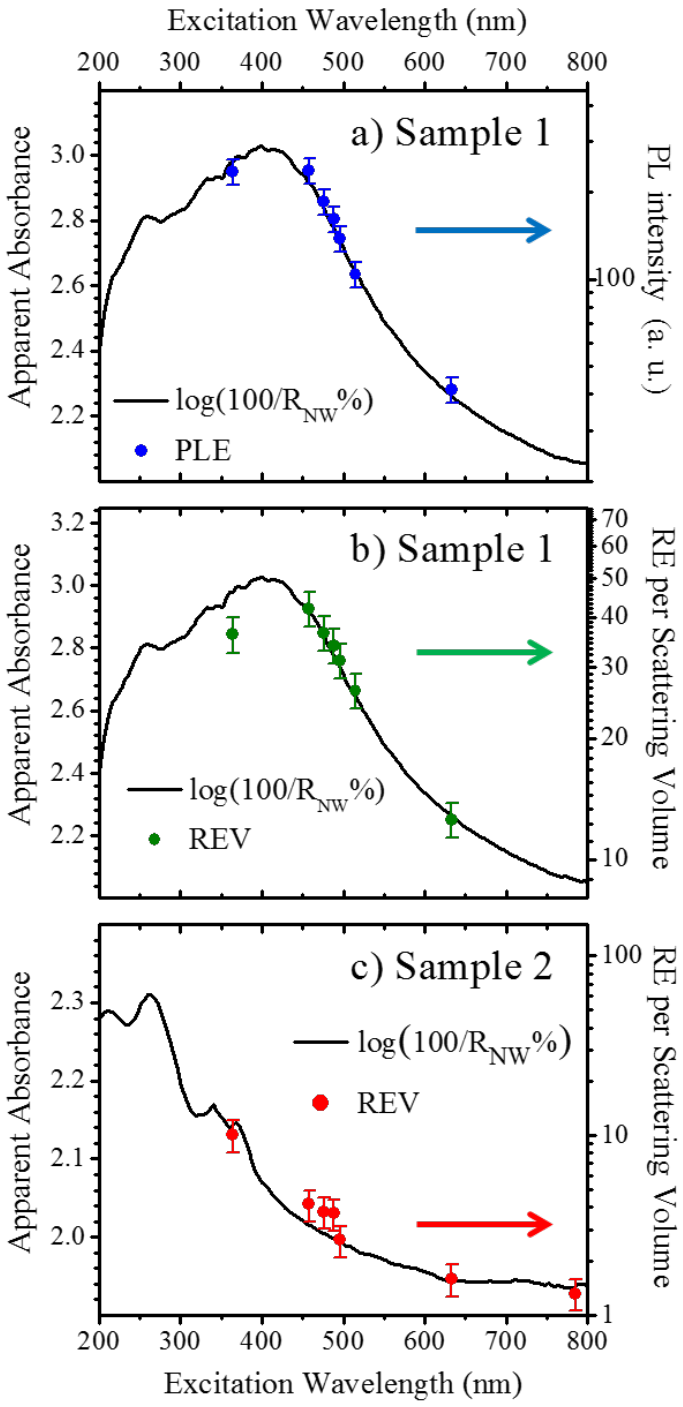

Figure 5.12: a) PL emission of sample 1 evaluated at 690 nm. b) e c), Raman enhancement with respect to the c-Si bare substrate for sample 1 and 2, respectively. All the trends are plotted as a function of the incident laser wavelength and compared to the apparent absorbance of the corresponding sample (black lines). The arrows indicate the y-axis corresponding to the plotted data having the same color [63]. Notice that the absorbance on the left y-scale represents a logarithmic quantity like the right y-scale.

However, this normalization underestimates the exact Raman enhancement in NW material, because the Raman radiation is also trapped and then strongly absorbed. To extract the actual absorption from the NW layer, we calculate the *apparent absorbance* as obtained from the reflectance RNW % measurements as $\log(100/RNW\%)$ after normalization to the reflectance of the silicon substrate. This curve, shown in figure 5.12, represents the extinction signal due to in-plane multiple scattering processes through the 2D fractal structure, showing a maximum when the effective wavelength λ_{eff} resonantly matches the maximum intensity of the refractive index fluctuations in the medium (peak of lacunarity). When this occurrence is fulfilled, the in-plane multiple scattering processes in the fractal array can become more relevant. In figure 5.12 a), we show the trend of PL intensity at 690 nm as excited by the different laser colors (PLE), while its REV of sample 1 as a function of the excitation laser wavelength λ is plotted in figure 5.12 b). Both trends of PLE and the REV closely follow the shape of apparent absorbance curve. Exactly the same procedure was applied to elaborate the data of sample 2, whose figure 5.12 c) shows the comparison between the corresponding apparent absorbance spectrum and REV. Therefore, we can state that increasing the dwell time of the pump inside the material leads to the direct consequence of the increment of emission cross sections. Figure 5.13 clearly confirms this scenario. Here, lacunarity curves for samples 1 and 2 are presented compared with the REV trends plotted as a function of λ_{eff}. The accord between two trends provides evidence regarding how the heterogeneities influence the scattering inside the sample structure. In particular, the results highlight how the Raman enhancement is correlated on the length scales, which are characteristic of the finite fractal structure. Note that lacunarity, which describes the refractive index fluctuations, is directly related to the scattering cross-section.

In conclusion, the results of our investigations show the way the disorder affects the transport of light in random Si NW array. We demonstrated the strong correlation between the optical properties and the fractal characteristics. In particular, we found evidences of light trapping due to the lacunarity of fractal textures. This localization causes strong light-matter interactions, which result in a nearly complete absorption of visible light and enhanced Raman emission. In fact, the fractal array promotes a high light-trapping efficiency

with total reflectance values down to the 0.1% when the incident wavelength matches the maximum heterogeneity size exhibited by the arrangement of Si NWs. Moreover, Raman emission is enhanced by multiple scattering processes and shows to depend on the effective wavelength [63]. However the magnification of Raman signal requires a *surface enhanced Raman spectroscopy* (SERS) techniques, which are usually based on the plasmonic effects to locally amplify the electromagnetic field. Actually, in our samples, the localization and the amplification of electromagnetic field are mediated by the coherent multiple scattering of radiative waves. The latter statement is further confirmed by coherent back scattering experiments, which we performed on the Si NWs and are showed in the next chapter.

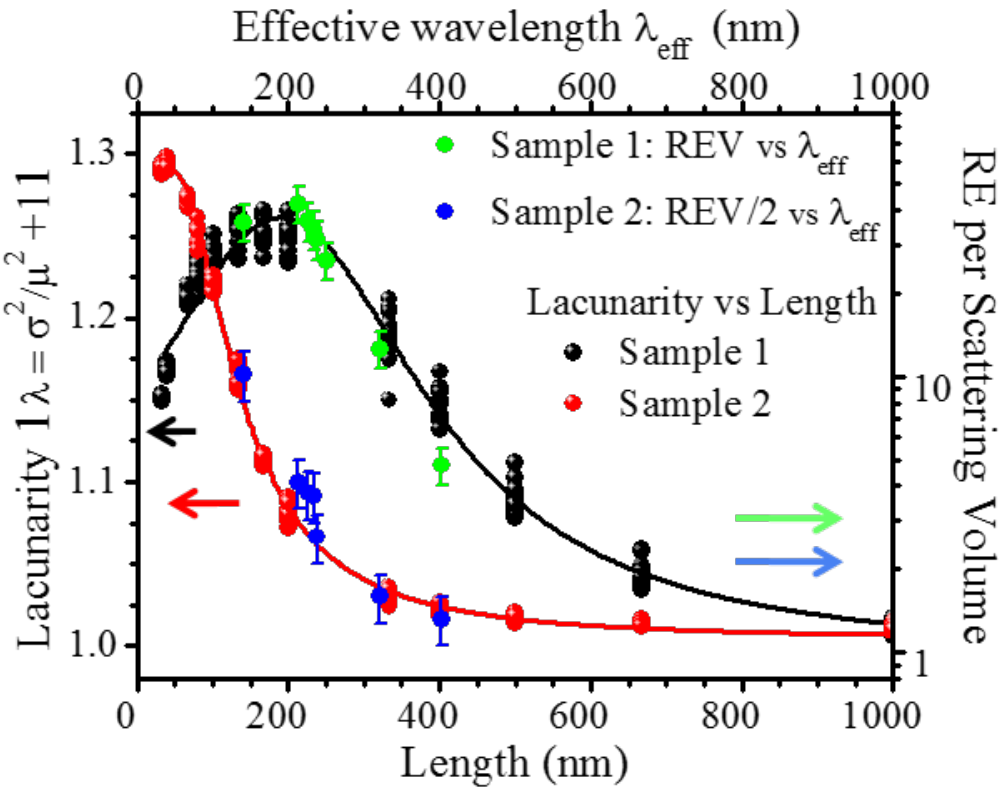

Figure 5.13: Comparison between lacunarity and Raman enhancement. The Raman enhancement of sample 1 (green dots) and sample 2 (blue dots) plotted as a function of the effective incident laser wavelength propagating in the medium λ_{eff} and compared with the corresponding lacunarity curves (black and red lines represent samples 1 and 2, respectively) [63].

Chapter 6

Coherent backscattering of light from Si NWs

The latter chapter shows the wonder optical property of vertically aligned Si NWs due to the strong elastic scattering of light taking place into the NW array. In particular we explained how the enhanced absorption of visible light is related to the fractal arrangement of the NWs, which promotes the in-plane light confinement. Actually fractals are known for forming hot-spot regions, where the light-matter interaction intensifies because of the confinement of electromagnetic field due to the coherent multiple scattering of radiative waves. The presence of this latter mechanism in our NW samples is confirmed by the theoretical simulations [63].

In light of these evidences, we explore the angular dependence of the scattered light from the Si NWs searching for coherence effects in backscattering intensity. To this end, we excite the NW samples with a circularly polarized laser beam at normally incidence to the sample surface and collect the scattering light as a function of the scattering angle both in helicity-conserving channel, i.e. by selecting the same circular polarization of the pump beam, and in the two linear polarization. The collected signals in these two latter polarization, i.e. the non-conserving channels for polarization, contains only the incoherent component for the backscattering light and their average is taken for normalizing the signal from the conserving channel (for detailed description of CBS technique see section 3.3).

In this chapter, we report on the CBS measurements performed on the fractal Si NW forest. We characterize the strength of light scattering taking place in Si NW samples by means of CBS cone, which results in the context of the weak localization interference effects (see section 2.3.2). Moreover we investigate how the coherent multiple scattering of light mediates the enhancement of the Raman backscattering. For this purpose, we performed also CBS experiments collecting the Raman light from our NWs. We analyse the angular shape of Raman CBS and put it in relation with the scattering strength of Si NW samples and the Stoke shift of the Raman light. In order to do that we have extended the theoretical explanation of CBS for the Rayleigh light to the Raman case. Therefore, we show that the coherent nature of spontaneous Raman scattering, typically occurring on a nanometer length scale, is beautifully unveiled also on a macroscopic scale through the appearance of an enhanced backscattering cone in a simple backscattering experiment. To our knowledge, this is the first experimental evidence of Raman coherent backscattering ever reported [64].

6.1 Coherent backscattering of Rayleigh light

We investigate the coherent backscattering of light on two different Si NW samples, which are here labelled with *sample 1* and *sample 2*. Both of them are prepared by maskless metal-assisted wet etching technique but using two different types of metal precursors. The morphologically characterization of them reveals the presence vertically aligned Si NWs arranged in a two-dimensional random organization (see figure 6.1). The SEM images in panels a) and b) of figure 6.1 belong to sample 1, which is the same of the chapter 5 and whose the metal precursor is a thin gold film deposited at percolation limit, according to fabrication process described in section 5.1. The NWs of sample 2 are shown in panels c) and d) of figure 6.1. Here the Si NWs have been synthesized by immersing directly a crystal silicon wafer in an aqueous solution containing silver nitrate ($AgNO_3$) as metal precursor and HF as etching agent at concentrations of 0.02 M and of 5 M, respectively. In solution the dissociated silver salt realizes a precipitation of silver nanoparticles randomly distribute on the silicon surface. Also in this fabrication process, the formation of NWs is due

to the HF erosion of the silicon oxide, which locally forms under the metal particles. The texture of the two samples is substantially different. Sample 1 displays a dense distribution of vertically aligned NWs with an average diameter of 7 nm and with a length of 2.6 μm, while the Si NWs on sample 2 are less dense distributed and much larger and longer with an average diameter of 100 nm a height of about 8 μm. The distribution of these latter is still random but their arrangement is no more fractal. In fact, we notice the presence of NW bunches each other well separated by air-voids.

The light transport in these systems is expected to be highly anisotropic, because of the strong vertical orientation of the Si NWs, as shown in figures 6.1 b) e d). Nevertheless, coherent backscattering can take place, and be observed, in systems with strong anisotropies in either direction [69, 108]. The mean free

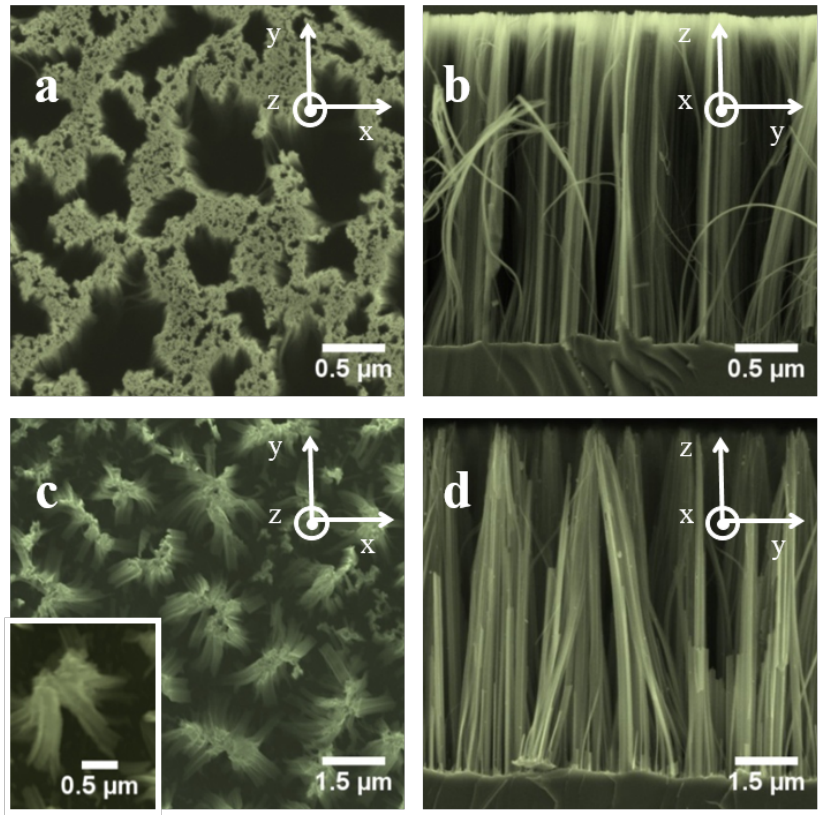

Figure 6.1: Plan view and cross section images of the Si NW array performed by using a field emission scanning electron microscope Zeiss Supra 25. In a) and b) the SEM images of the Si NWs on sample 1. c) and d) show the NWs obtained on sample 2. The inset in c) panel is a zoom to higher magnification to observe the NWs of two different samples on comparable dimensions [64].

paths in the x and y direction (in the sample plane) determine the width of the backscattering cone. The z direction comes into play with respect to the (optical) thickness of the sample L/l_z. The transport mean free path l_z in the vertical direction (parallel to the NWs) may be much larger than l_{xy} in the xy-plane (orthogonal to the NWs). However, some scattering in the z direction is of course required, otherwise the sample will appear transparent. The precise value of l_z is difficult to determine and the situation is further being complicated in our case by some roughness of the sample substrate (which also actively contributes to couple the scattered light from the z direction into the xy-plane). Needy of an efficacious way to quantify l_z, we define an effective sample thickness $L_{eff}/l_t = L/l_z$ accounting for the effect of the different value (larger or smaller) of mean free path along the z direction. This way allows to compare theory with experiments [64].

To assess the scattering strength of the Si NW samples in a quantitative way we have obtain the coherent backscattering cone by normalizing the he-

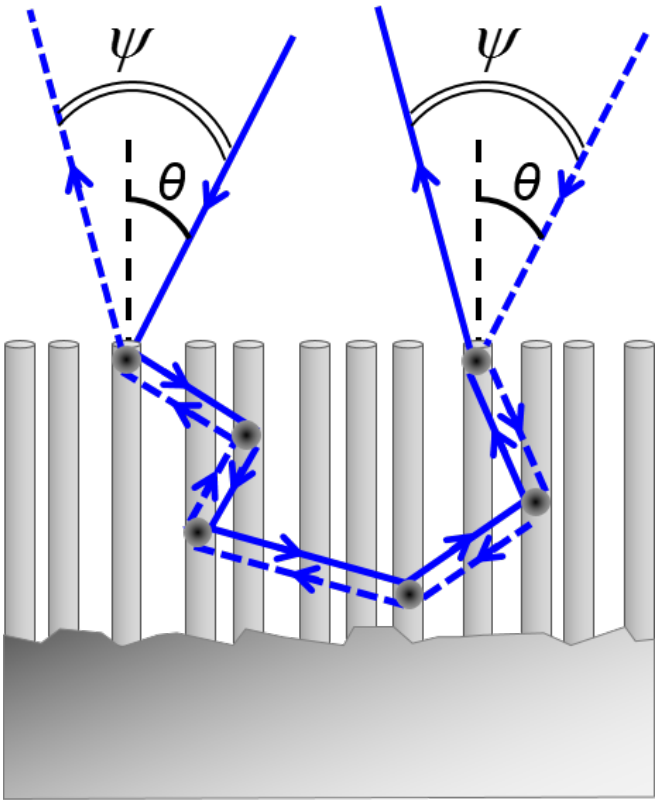

Figure 6.2: Sketch of coherent backscattering taking place in NWs [64].

licity conserving channel to the diffuse background. The angular dependence of backscattering light measured at $\lambda = 532$ nm of laser wavelength different polarization channels on sample 1 and 2 are shown in figures 6.3 a) and b), respectively. To acquire the conserving channel of light polarization (blue dots), we shine the sample with a circular polarized light and collect the backscattered light in the polarization conserving channel by excluding the non conserving channel of single scattering events and reflections from the optical set up, as described in section 3.3. The diffuse background (green dots) is detected averaging the linear polarization (non conserving channels) for s and p. CBS cones at wavelength $\lambda = 532$ nm for sample 1 and 2 are shown in figures 6.4 a) and b), respectively. In both samples the CBS cone shows a pronounced rounding of the tip due to the combined effect of light absorption and finite thickness of the Si NW layer, which strongly suppress the contribution of very long paths to the backscattering intensity. Therefore, we fit the data using the finite-slab model for the CBS intensity expressed by equations 3.18, 3.13 and 3.14. The experimental enhancement factor E_{exp} is the height of CBS cone, which deviates from its theoretical value 2 due to residual of single scattering and the stray light. The transport mean free path $l_t \equiv l_x = l_y$ and an effective optical thickness $L \equiv L_{eff}$ left are free fitting parameters. These two parameters have very different effects on the shape of the backscattering cone and lead to a rapid convergence of the fit towards reliable values of these parameters. The inelastic (absorption) mean free path l_i is also included in the fit function as a fixed parameter. In fact, we independently estimate the value of l_i for both samples by scaling the optical extinction length of bulk silicon to the effective Si fraction present in the NW layer. The latter is determined by combined SEM analyses and energy dispersive x-ray (EDX) spectroscopy [63]. The fits to the data are shown by the red lines in figure 6.4. The extrapolated values of transport mean free path are $l_t = 0.169\mu$m and $l_t = 0.483\mu$m for sample 1 and sample 2, respectively, resulting in very strong scattering media[1]. The values of effective optical thickness are relatively large with $L_{eff}/l_t = 17$ for sample 1 and $L_{eff}/l_t = 5$ for sample 2, pointing towards a strong effective scattering in the z direction despite the strong anisotropy of the NW material [104, 63].

[1]These values are in line with the typical mean free-paths obtained from CBS measurements in GaP NW arrays, confirming that our Si NWs are among the strongest scattering materials to date.

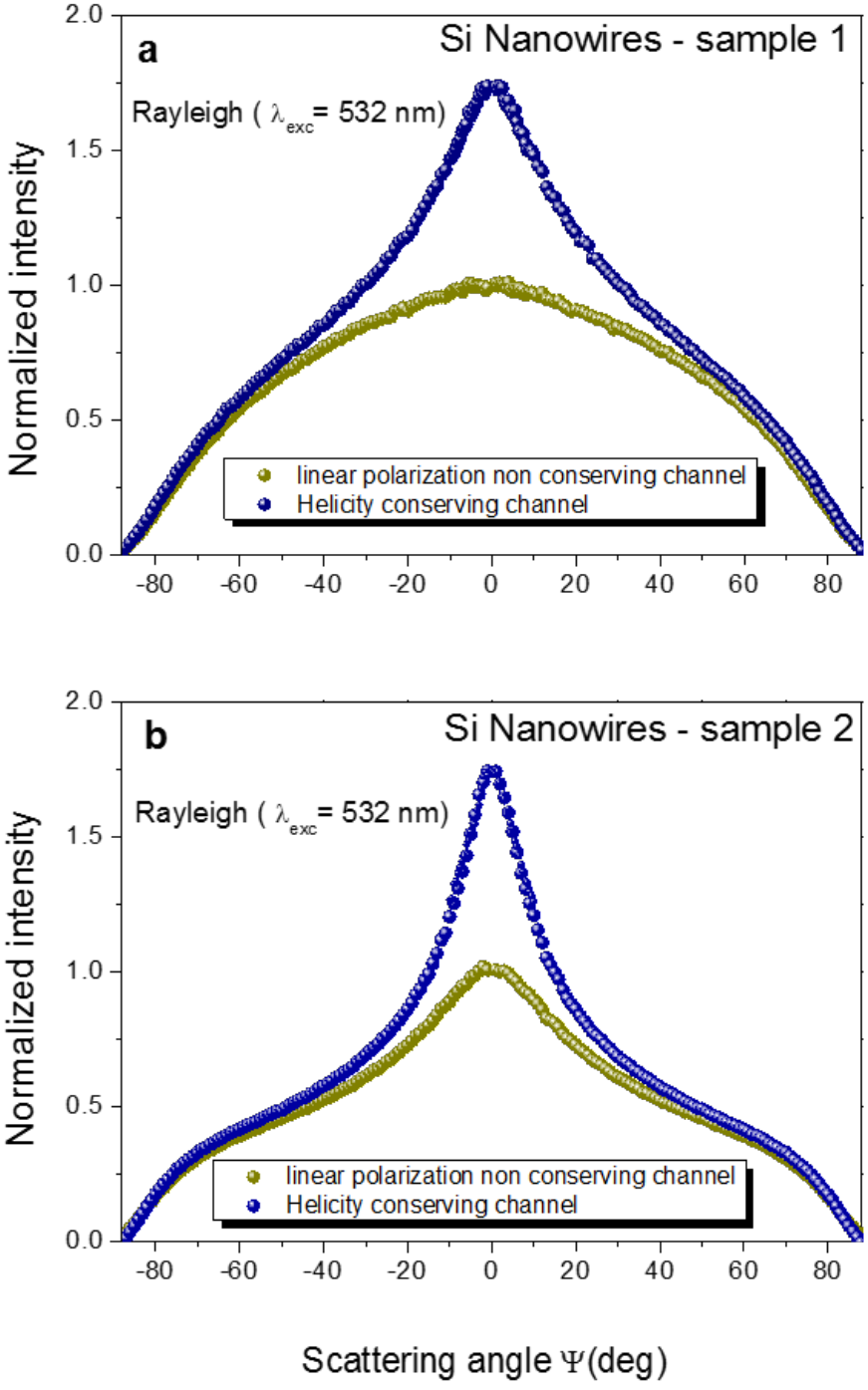

Figure 6.3: Coherent backscattering (blue dots) and the diffusive background (green dots) signals measured at $\lambda = 532$ nm on Si NW sample 1 and 2 (a and b respectively). Notice that the unusual shape in the angle-dependent scattering intensity of sample 2 is due to a scattering behaviour that deviates from the ideal Lambertian distribution.

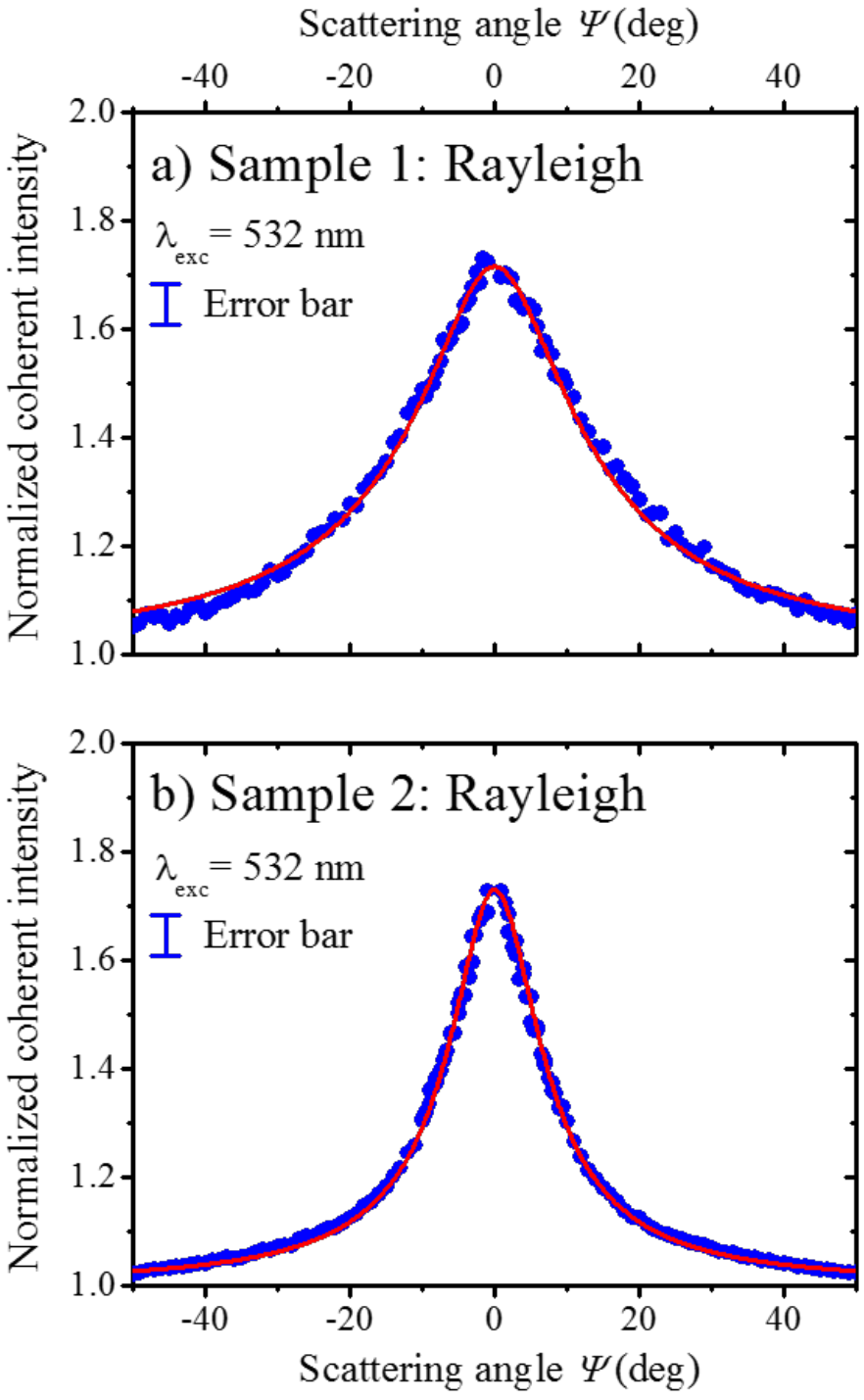

Figure 6.4: Coherent backscattering cones after normalization to the diffusive background signals referred to Si NW sample 1 and 2 (a and b respectively). The red continuous lines are the best fitting curves obtained by the finite slab model [64].

6.2 Coherent backscattering of Raman light

Once characterized the scattering strength of our samples and the fitting parameters of CBS for Rayleigh light, we explore also the angular intensity dependence of Raman scattered light from the Si NWs in both samples searching for the evidence of coherence effects in the backscattered intensity. Such investigations are motivated with the evidences of the mediating role played in the enhancement of Raman backscattered signal from Si NW samples by the multiple scattering of light, as we discus in the latter chapter. In particular, the Raman spectrum in figure 5.11 shows at same time an enhancement of first order Raman peak and a reduction of the Rayleigh light [63]. Such an effect is compatible with the simple model of multiple scattering that includes both Rayleigh and Raman photons, because the latter increases with the number of scattering events [109]. Moreover, we cite also the measurement of Raman spectrum performed on a Si NW sample infiltrated with silicone oil (a high index fluid, n $\simeq$ 1.6), which shows a lower enhancement of first order Raman peak. The oil filling the air voids of NW texture reduces the refractive index contrast with respect to that between the air and the silicon and lowers the scattering strength of the Si NW forest [66].

As for the CBS measurements of Rayleigh light, we excite the NW samples with a circularly polarized laser beam (wavelength of 532 nm) at normally incidence to the sample surface and collect the backscattered Stokes Raman peak as a function of the scattering angle both in helicity-conserving channel, i.e. by selecting the same circular polarization of the pump beam, and in the two linear polarizations (non-conserving channel). Again, the collected signals in the latter polarizations contain only the incoherent component for the backscattering light and their average is taken for normalizing the signal from the conserving channel, while the first polarization allows also to collect the coherent component of backscattered signal (for detailed description of CBS technique see section 3.3). The experimental data for samples 1 and 2 are shown in figures 6.5 a) and b), respectively. There is a clear enhancement around the backscattering direction (ψ = 0 deg) for the helicity-conserving channel on both samples, in contrast the linear polarization non-conserving channel follows a smooth Lambertian-like diffusing behaviour.

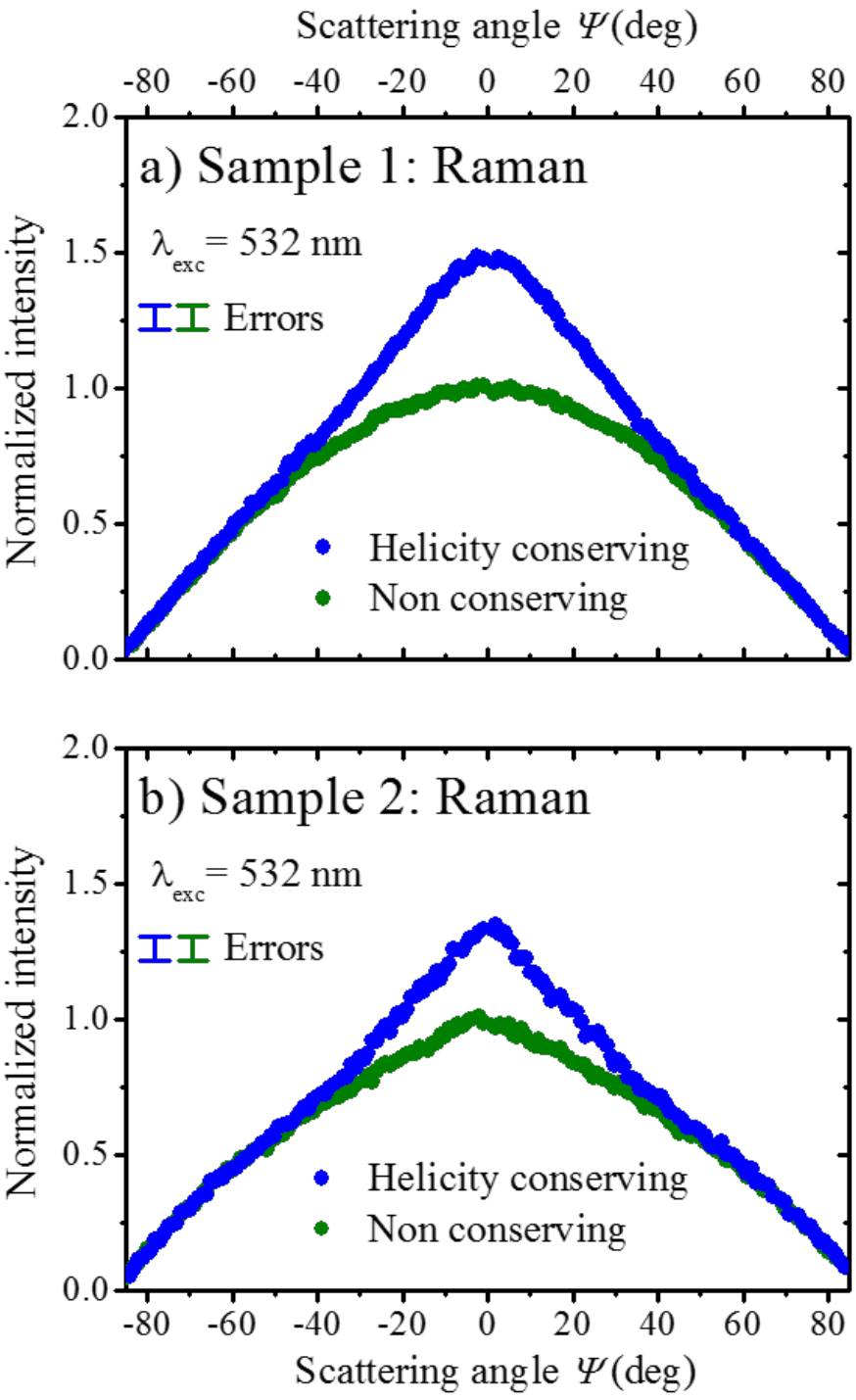

Figure 6.5: Raman backscattered intensities as a function of detection angle for sample 1 (a) and sample 2 (b). The helicity conserving channel and the linear polarization non conserving channel configurations are represented by blue and green dots, respectively [64].

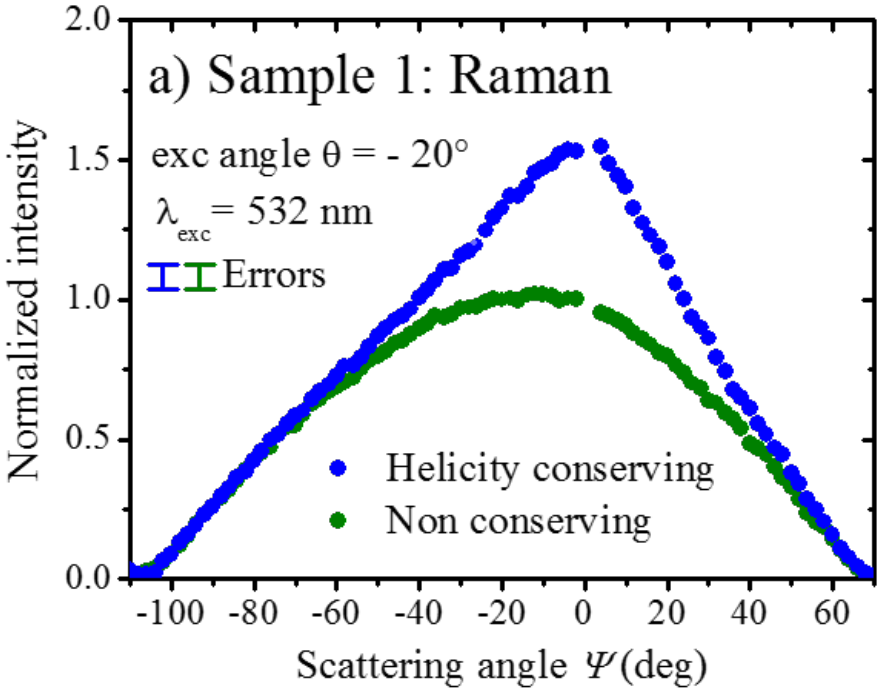

Figure 6.6: CBS of Raman light with excitation deviating of an angle θ from the normal to the sample surface, while the backscattering angle ψ is still defined with respect to the excitation beam direction [64].

We prove the CBS nature of the Raman enhancement by verifying that the observed peak in conserving channel arises exactly along the backscattering direction. For this purpose, we repeat the CBS experiment with an incident laser beam forming an angle of 20 deg with the normal to the sample surface. The experimental data reported in graph of figure 6.6 show the characteristic angular trend of the CBS enhancement around the tilted incidence direction. Therefore any doubt about geometrical artefacts of NW anisotropy is dispelled.

We recall that the spontaneous Raman scattering is usually considered as one of such incoherent processes. However, the Raman scattering consists in the inelastic scattering of an optical pump wave within a material by creation (or annihilation) of quanta of vibration (phonon) and the Stokes (or the anti-Stokes) wave, which is locked in phase with the pump wave through the phonon phase of lattice. Both the frequency and the phase of the phonons populating the vibration mode are equal to that of the beating due to the overlapping between the pump signal and Raman local field [110].

Therefore, there exists a fundamental difference between the incoherence of spontaneously emitted light (as for instance in the fluorescent light emission) and that of the spontaneous Raman scattering. The first process is incoherent because it comes from the quantum vacuum fluctuations of electromagnetic field, whose intrinsic randomness is reflected by the light incoherence. on the contrary, Raman scattering is coherent in origin but becomes quickly incoherent, since its coherence is fundamentally related to that of the phonon, which has a typical coherence time and coherence length of the order of picoseconds and of tens of nanometres, respectively, in solid-state materials. For that reason, the phonon-phase information becomes lost by overlapping of all Raman photon generated from a bulk sample and the Raman light is commonly considered an incoherent type of radiation when observed in far-field configuration [64], the typical configuration used in the Raman experiments. On the contrary, the Raman signal preserves its coherent nature when detected by a near-field technique, which restricts the collection of light into a sample region with a size $a \ll \lambda$. Up to now, the only known experimental way to put in evidence the coherence of spontaneous Raman scattering has been recently reported in near-field regime, where the Raman signal is probed by using very sharp tips on a length scale much smaller than λ and comparable to the phonon coherence length [111]. Therefore, we look for a strong confirmation of the new experimental observation of CBS enhancement for Raman light by comparing the first order Raman peak and the photo-luminescence (PL) emission angular profiles acquired under the same experimental conditions, shown in figure 6.7. That is possible since we perform the simultaneous measurement of both the backscattered Raman light and the PL emission. In fact, the latter is clearly visible in measured Raman spectra as a smooth decaying background extending well below the Raman Stokes wavelength (see figure 6.7 a). The backscattered intensities of the Raman and of the photo-luminescence (PL) signals evaluated by integrating the spectra over a narrow wavelength range just below the Raman peak (the coloured areas of graph in figure 6.7 a). Figure 6.7 b) shows the results of the data analysis of the two signals. Notice, here, that the Raman curve (blue dots) is enhanced around the backscattering direction with respect to the PL curve (red dots), whose the angular trend follows a cosine (Lambertian) law.

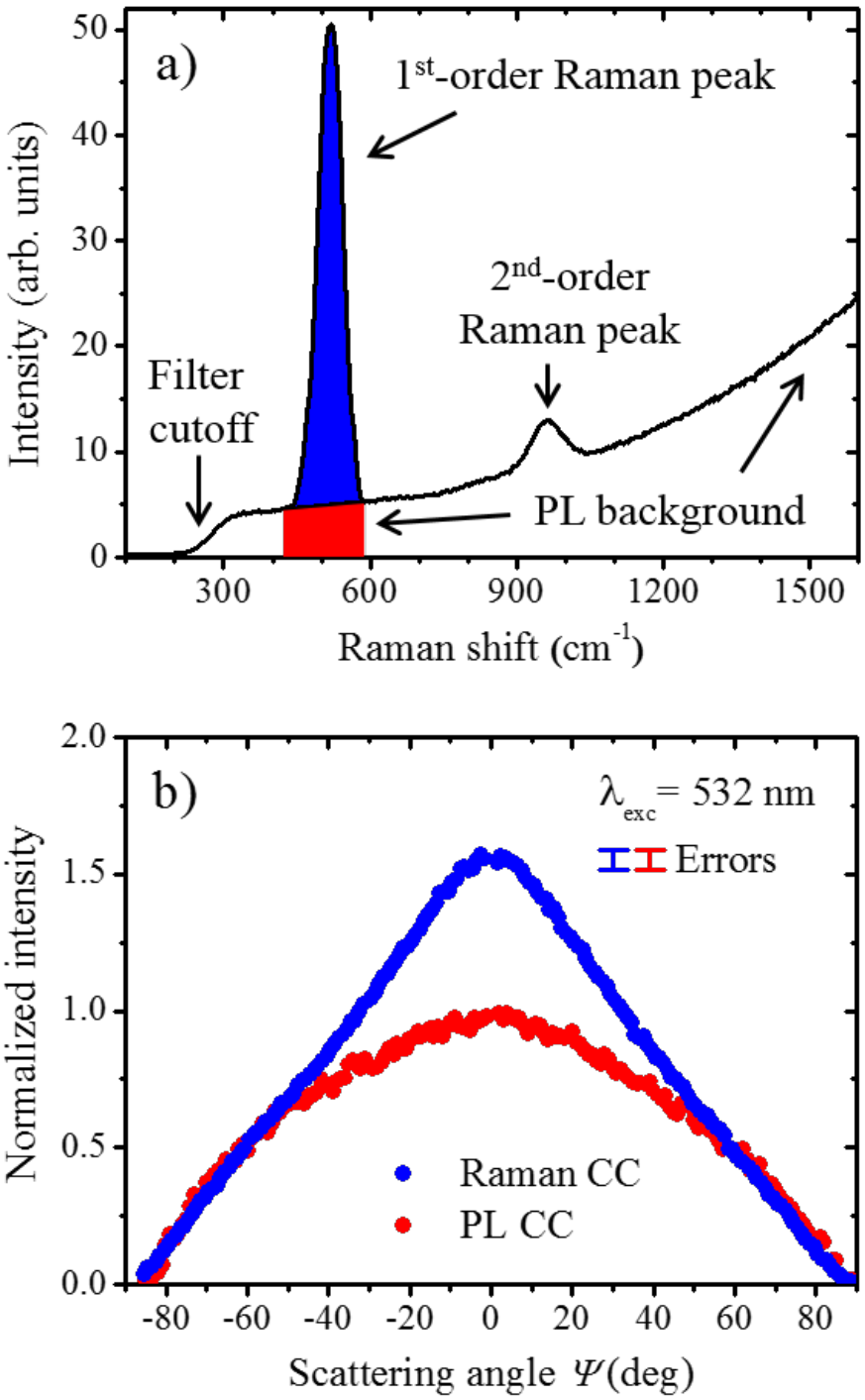

Figure 6.7: Comparison between the backscattered signals of the Raman light and of the PL emission from sample 1 obtained in helicity-conserving channel configuration by exciting with a laser line at 532 nm [64].

Hybrid Rayleigh-Raman path

The aforementioned experimental observations confirm clearly the occurrence of constructive interference for the Raman Stokes waves of Si NWs in the backscattering direction. However, the question about the coherence preservation of Raman radiation remains. In fact, differently to the established CBS for Rayleigh light, Raman waves are generated inside the material within a random walk of the pump beam, which has a length of about few microns (according to results of section 5.3). On the other hand, the coherence length of the lattice vibrations is much shorter than microns. Therefore the only way is that two reciprocal paths for the wave radiation have their Raman scattering event at the same scattering site. That is in agreement with the reciprocity hypothesis of optical paths, which underlies the coherent back scattering phenomena, confirming once more the true observation of coherent backscattering for Raman light (RCBS). Note that a single Raman scattering event is coherent for all photons generated within a coherence length meaning that there is a well-defined phase relation between the pump and Raman light (as opposed to spontaneous emission).

We clarify the situation by means of the scheme represented in figure 6.8. Here, the blue lines I and I' represent two reciprocal optical paths of the pump beam. This latter after some elastic scattering event gives rise to a Raman scattered wave at an arbitrary point r_j into the Si NW sample. The red lines S and S' represent the generated Stokes-shifted waves, which continue to propagate within the sample by multiply scattering till they exit as a Raman beam. Therefore we deal with couples of hybrid Rayleigh-Raman reciprocal paths. In general, these couples of hybrid paths should accumulate a random phase-difference, which makes the outgoing Raman beams to be incoherent. Moreover, polarization of these hybrid paths may also be not conserved, due to the presence of an inelastic scattering event. We show, however, that if the Stokes-shift introduced by Raman scattering is small compared to the Rayleigh wavelength, both polarization and phase coherence between the hybrid paths is actually preserved, thus restoring reciprocity and allowing the coherent superposition of the outgoing Raman fields in the backscattering direction. A detailed sketch of the Raman scattering event occurring at r_j is shown in figure 6.8, for both the direct (solid line) and reverse (dash line) hybrid paths.

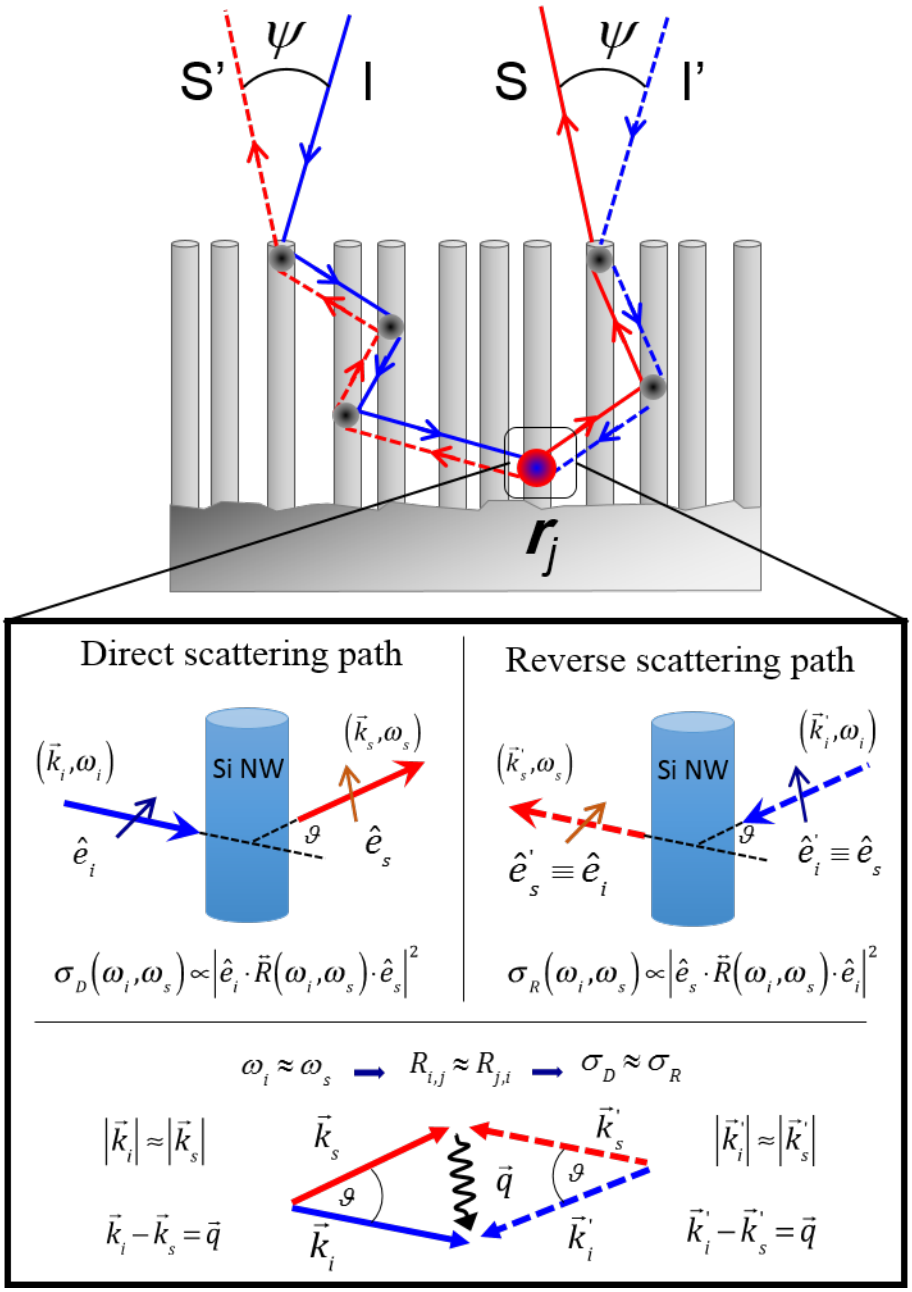

Figure 6.8: Illustration of basic concepts for the coherent Raman backscattering process. a) Schematic picture of light transport in mixed Rayleigh-Raman paths. b) Zoom on the depicted Raman scattering at r_j. In the *direct* Rayleigh-Raman scattering path, a photon of frequency ω_i and polarization e_i is Raman scattered by a Si nanowire with a cross-section σ_D, giving rise to a photon of frequency ω_s and polarization e_s. In the *reverse* path, the Rayleigh and Raman photons are exchanged and propagation directions reversed) a photon of frequency ω_i and polarization e_s is Raman scattered by the same Si nanowire with a cross-section σ_R, giving rise to a photon of frequency ω_s and polarization e_i. Assuming $\omega_i \approx \omega_s$, the Raman tensor $R(\omega_i, \omega_s)$ is symmetric with respect to exchange of e_i and e_s, yielding $\sigma_D = \sigma_R$ [64].

The corresponding scattering cross-sections for the two processes are also shown, where $R(\omega_i, \omega_s)$ denotes the second-rank Raman tensor. If we now assume $\omega_i \approx \omega_s$, as it is usually done in Raman theory, the $R(\omega_i, \omega_s)$ becomes symmetric with respect to exchange of the polarization versors $\hat{e}_i$ and $\hat{e}_s$ [112, 113, 114]. This condition is verified for the first order Raman scattering in crystals that probes phonon frequencies at $q \simeq 0$ (phonon wave vector), i.e. having very long wavelength compared to the lattice constant, while in the general case one has to consider the symmetry properties of the crystal. The condition of symmetry with respect to exchange $\hat{e}_i$ and $\hat{e}_s$ yields the same cross section for the two reciprocal scattering events and also ensures polarization conservation upon reversing the optical paths. Moreover, the assumption $\omega_i \approx \omega_s$ implies that $|\vec{k}_i| \approx |\vec{k}_s|$ (and $|\vec{k'}_i| \approx |\vec{k'}_s|$), thus making the same phonon mode (ω_q, $\vec{q}$) to be equally available for both scattering paths. This has the additional important consequence that the random phase-jump introduced by the creation/annihilation of a phonon is exactly cancelled out when considering the phase-difference between reciprocal paths [64]. We point out that this last statement is strictly true provided that the dwell time for the two reciprocal paths is much shorter than the phonon coherence time. In our case, due to the very short transport mean free path (deduced by CBS cones) and to the strong material absorption, we estimate an average dwell time of the order of few femtoseconds (corresponding to an average total scattering path of the order of few microns), which is far below the 1 picoseconds phonon coherence time in crystalline silicon [115, 116].

We can resume all these considerations asserting that:

i multiple Raman scattering within our Si NW material may be described by hybrid Rayleigh-Raman scattering paths, for which reciprocity holds true because of the relative little Stoke-shift;

ii the temporal coherence between reciprocal paths is held, since the values of l_t for our samples allow a mean dwell time of multiple scattering very small with respect to the coherence time of phonons in Si NWs.

Therefore the observed Raman enhanced cone is indeed due to the constructive interference in backscattering direction of Raman shifted waves that are coherently generated in a multiple scattering process.

6.2.1 Theoretical model of dephasing

The quantitative evaluation of this phenomenon require the extension of standard CBS theory (showed in section 2.3.2) to the case of Raman scattering by means of Green's function and its diagrammatic representation. In these latter the Raman scattering event is described by a new t-matrix $t_\omega\left(\vec{r}_j, \vec{r}_{j+1}; \omega_i, \omega_s\right)$, which obeys reciprocity since the relative little Raman shift $\left|\omega_i - \omega_s\right| / \omega_i \approx 0$; hence

$$t_\omega\left(\vec{r}_j, \vec{r}_{j+1}; \omega_i, \omega_s\right) = t_\omega\left(\vec{r}_{j+1}, \vec{r}_j; \omega_i, \omega_s\right). \tag{6.1}$$

Also the frequency dependence of the average Green's function $\langle G\left(\vec{r}_j, \vec{r}_{j+1}; \omega\right)\rangle$ is now taken in account by indicating the Rayleigh light and Raman signal propagators with $\langle G\left(\vec{r}_j, \vec{r}_{j+1}; \omega_i\right)\rangle$ and $\langle G\left(\vec{r}_j, \vec{r}_{j+1}; \omega_s\right)\rangle$, respectively. The diagrammatic expansion of Raman backscattered intensity, shown in figure 6.9, helps to understand that interference effects in backscattering take place only if the difference between $\langle G\left(\vec{r}_j, \vec{r}_{j+1}; \omega_i\right)\rangle$ and $\langle G\left(\vec{r}_j, \vec{r}_{j+1}; \omega_s\right)\rangle$ is small. This is true when $\left|\omega_i - \omega_s\right|$ is small enough to neglect the dispersion in the medium. Nevertheless, when the reciprocal waves propagate off the same scattering event $\left(\vec{r}_j - \vec{r}_{j+1}\right) = -\left(\vec{r}_{j+1} - \vec{r}_j\right)$ at different frequencies, for example $\omega = \omega_i$ and $\omega' = \omega_s$ (or, in the reciprocal path, $\omega' = \omega_i$ and $\omega = \omega_s$) as shown in C diagrams of figure 6.9, a phase difference

$$\Delta\phi_j = \frac{\left(\omega_j - \omega'_j\right)}{c} \left|\vec{r}_j - \vec{r}_{j+1}\right| \tag{6.2}$$

is developed with c the speed of light. At the end of whole scattering path, the two waves come out from the scattering system with a total dephasing $\Delta\Phi$ given by the sum on the all these phase difference $\Delta\phi_j$; that it is possible to express as:

$$\Delta\Phi = \left| \sum_j \frac{\left(\omega_j - \omega'_j\right)}{c} \left|\vec{r}_j - \vec{r}_{j+1}\right| \right| \tag{6.3}$$

Note also that the ω dependence of the t-matrix $t_\omega\left(r_j, r_{j+1}\right)$ can be neglected for the small frequency differences occurring in Raman scattering. The above argument shows that an interference contribution, and hence a coherent backscattering signal, can be expected for multiple Raman scattering, for those lights paths in which $\Delta\Phi$ remains significantly below π.

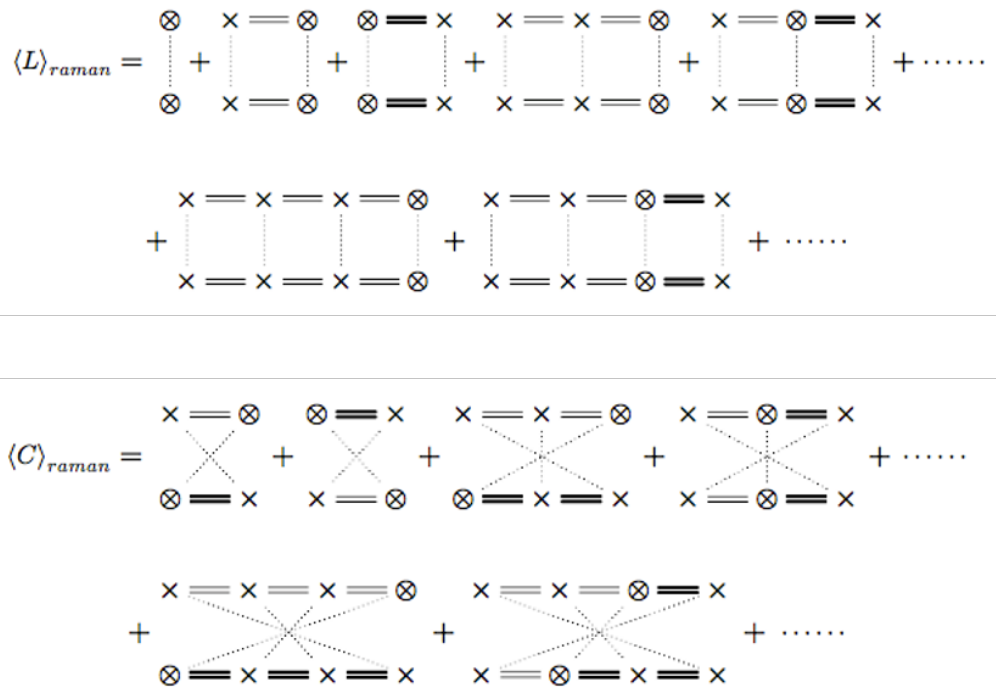

Figure 6.9: Diagrammatic representation of *ladder* L and *most-crossed* C diagrams. Here, the $\otimes$ stands for the Raman scattering event, while the propagator of the Raman signal and Rayleigh light propagators are represented by using thick double and regular double lines, respectivelly [64].

The presence of a dephasing mechanism in the coherent contribution to multiple Raman scattering is expected to alter significantly the probability of wave diffusion in the disordered material, hence leading to a modified backscattering cone in a way similar to what observed for multiple scattering from particles subject to Brownian motion or in the presence of a magnetic field [56]. In general, one can show that dephasing affects the intensity propagator $F(\vec{r}_1, \vec{r}_2; t)$ (proportional to the diffusion probability) by a global factor, so that upon summation over all multiple scattering sequences one obtains an expression of the form $F(\vec{r}_1, \vec{r}_2; t) \left\langle e^{i\Delta\Phi(t)} \right\rangle$, where $\Delta\Phi(t)$ is the phase difference between reciprocal scattering paths. This phase difference is a random variable whose statistical distribution depends on the specific mechanism at the origin of dephasing. Normally, the average over this distribution takes the form of a decaying function of time as $\left\langle e^{i\Delta\Phi(t)} \right\rangle = e^{-\frac{t}{\tau_d}}$, which provides a physical interpretation of a cut-off time τ_d (corresponding to a cut-off length

$L_d = \sqrt{D\tau_d}$) describing the loss of phase coherence. Once the temporal dependence of this average factor is determined, the relevant properties such as the diffused intensity may be simply obtained through a Laplace transform as

$$\gamma \propto \int_0^\infty F\left(\vec{r}_1, \vec{r}_2; t\right) e^{-\frac{t}{\tau_d}} dt \tag{6.4}$$

The problem of dephasing in coherent Raman backscattering is reduced to the evaluation of the average phase difference $\langle \Delta\Phi_N \rangle$ between any arbitrary Rayleigh-Raman reciprocal path involving N scattering steps. According to the sketch of figure 6.8, the total phase difference accumulated in any of these paths may be separated into the sum of two contributions as:

$$\begin{aligned} \Delta\Phi_N &= \textstyle\sum_{j=1}^{R-1} \Delta k \left|\vec{r}_j - \vec{r}_{j+1}\right| - \sum_{j=R}^{N-1} \Delta k \left|\vec{r}_j - \vec{r}_{j+1}\right| \\ &= \Delta k \textstyle\sum_{j=1}^{R-1} \Delta r_j - \Delta k \sum_{j=R}^{N-1} \Delta r_j \end{aligned} \tag{6.5}$$

where R denotes the (random) position of the Raman scattering event shared by the two reciprocal paths and Δk is the wavevector change in the Raman process. We first evaluate the average of this phase over the mean distance between two successive scattering events

$$\langle \Delta\Phi_N \rangle_{\Delta r_j} = \Delta k \sum_{j=1}^{R-1} \langle \Delta r_j \rangle - \Delta k \sum_{j=R}^{N-1} \langle \Delta r_j \rangle = \Delta k l_t (2R - N) \tag{6.6}$$

where $\langle \Delta r_j \rangle \equiv l_t$ is the transport mean free path. Next, we need to evaluate the average over the position of the Raman scattering event, i.e. the average of the quantity $2R-N$, which can assume either positive or negative values. However, since different R correspond to different paired scattering paths adding up incoherently to the backscattering cone (i.e. two different reciprocal paths with equal but opposite phases do not cancel out their phases), we must take the average over the absolute value of the quantity $2R - N$:

$$\langle \Delta\Phi_N \rangle_{\Delta r_j, R} = \Delta k l_t \left\langle |2R - N| \right\rangle = \Delta k l_t \frac{\sum_{R=1}^{N} |2R - N| \, \mathbf{P}(R)}{\sum_{R=1}^{N} \mathbf{P}(R)} \tag{6.7}$$

where $\mathbf{P}(R) = (1 - P_{Raman})^{R-1} P_{Raman}$ is the probability for a Raman scattering event to occur at position R. Since $P_{Raman} \approx 10^{-6}$ is very small, we can assume that each Raman scattering event can occur at site R-th with the same probability $\mathbf{P}(R) \approx P_{Raman}$. This yields

$$\langle \Delta\Phi_N \rangle_{\Delta r_j, R} = \Delta k l_t \frac{1}{N} \sum_{R=1}^{N} |2R - N| = \Delta k l_t \frac{N}{2} = \Delta k \frac{l}{2} \tag{6.8}$$

We see that the average of the phase difference between reciprocal hybrid paths assume the very simple expression:

$$\langle \Delta\Phi_N \rangle = \frac{\Delta k l}{2}$$

where $l = N l_t$ is the total length of the path. Now, we evaluate the variance $\langle \delta\Delta\Phi_N^2 \rangle$ of the function of the equation 6.5

$$\Delta\Phi_N = \Delta k \left(\sum_{j=1}^{R-1} \Delta r_j - \sum_{j=R}^{N-1} \Delta r_j \right)$$

Making use of the following well-known properties of the variance:

$$\begin{aligned} &Var\left(aX - bY\right) = a^2 Var\left(X\right) + b^2 Var\left(Y\right) \quad , \\ &Var\left(\textstyle\sum_i X_i\right) = \textstyle\sum_i Var\left(X_i\right) \end{aligned} \tag{6.9}$$

and considering that the following relation holds

$$Var\left(\Delta r_j\right) = \left\langle \delta\Delta r_j^2 \right\rangle = \int \left(r - \langle r_j \rangle\right)^2 \mathbf{p}(r) dr = l_t^2, \tag{6.10}$$

where the distribution $\mathbf{p}(r)$ describes the statistics of the path length r, which corresponds to the Beer-Lambert law for the case of multiple scattering,

we have

$$\begin{aligned} Var\left(\Delta\Phi_N\right) &= Var\left(\Delta k \sum_{j=1}^{R-1} \Delta r_j - \Delta k \sum_{j=R}^{N-1} \Delta r_j\right) \\ &= \Delta k^2 Var\left(\sum_{j=1}^{R-1} \Delta r_j\right) + \Delta k^2 Var\left(\sum_{j=R}^{N-1} \Delta r_j\right) \\ &= \Delta k^2 \sum_{j=1}^{R-1} Var\left(\Delta r_j\right) + \Delta k^2 \sum_{j=1}^{N-1} Var\left(\Delta r_j\right) \\ &= \Delta k^2 \sum_{j=1}^{N-1} Var\left(\Delta r_j\right) \\ &= \Delta k^2 l_t^2 (N-1) = \Delta k^2 l_t l \end{aligned} \tag{6.11}$$

The variance of the phase difference have also a very simple form:

$$\left\langle \delta\Delta\Phi_N^2 \right\rangle = \Delta k^2 l_t l \tag{6.12}$$

The average phase factor associated with each elementary step is then:

$$\left\langle e^{i\Delta\Phi(l)} \right\rangle = e^{i\Delta\Phi} \int \mathbf{P}(\Phi) e^{i(\Delta\Phi - \langle\Delta\Phi\rangle)} \cong e^{i\frac{\langle\Delta\Phi\rangle - \left\langle \delta\Delta\Phi^2 \right\rangle}{2}} = e^{i\frac{\Delta k l}{2}} e^{-\frac{\Delta k^2 l_t l}{2}} \tag{6.13}$$

The dependence of the mean scattering time and diffusion coefficient can be evidenced using the relation $D = \frac{c l_t}{3}$, which leads to the following final form for the average phase factor:

$$\left\langle e^{i\Delta\Phi(t)} \right\rangle = e^{i\frac{3D\Delta k t}{2 l_t}} e^{-\frac{3D\Delta k^2 t}{2}} \tag{6.14}$$

Once the temporal dependence of this average factor is determined, the relevant properties such as the diffused intensity may be simply obtained through a Laplace transform as

$$\gamma \propto \int_0^\infty F\left(\vec{r}_1, \vec{r}_2; t\right) \left\langle e^{i\Delta\Phi(t)} \right\rangle dt = \int_0^\infty F\left(\vec{r}_1, \vec{r}_2; t\right) e^{-\frac{t}{\tau_d}} dt. \tag{6.15}$$

From equation 6.14 we see that the average phase factor affecting the total vertex is a complex valued function characterized by two different contributions:

1) a fast oscillating term, with a characteristic time (length) period $\tau_{d1} = \frac{2l_t}{3D\Delta k}$ set by the average value $\langle \Delta\Phi \rangle$ of the dephasing;

2) a slow exponentially decaying term, with a characteristic time (length) constant $\tau_{d2} = \frac{2}{3D\Delta k^2}$ set by the mean square value (variance) $\langle \delta\Delta\Phi^2 \rangle$ of the dephasing.

The combination of these two terms constitutes the coherence function for the RCBS process, which allows us to define two linked dephasing lengths

$$l_{d1} = c\tau_{d1} = \frac{2}{\Delta k} \tag{6.16}$$

and

$$l_{d2} = c\tau_{d2} = \frac{2}{\Delta k^2 l_t} = \frac{l_{d1}^2}{2l_t} \tag{6.17}$$

as the characteristic lengths of the specific dephasing mechanisms. We notice that l_{d2} sets a cut-off for long scattering paths, for which coherence of the Raman signal is globally lost due to random fluctuations in the phase difference between hybrid paths. On the other hand, l_{d1} represents a sort of phase-matching length, allowing the coherent superposition of reciprocal hybrid paths with both constructive and destructive interference contributions, depending on their relative phase difference being close to $2n\pi$ (in-phase paths) or close to $(2n+1)\pi/2$ (out of phase paths). For $l_{d1} > l_t$ (a condition which is easily met in strongly scattering materials) we have $l_{d2} \gg l_{d1}$, and the resulting coherence function is a damped cosine. This peculiar behaviour is shown in figure 6.10 plotting the real part of the RCBS coherence function calculated for typical sample parameters used in this work.

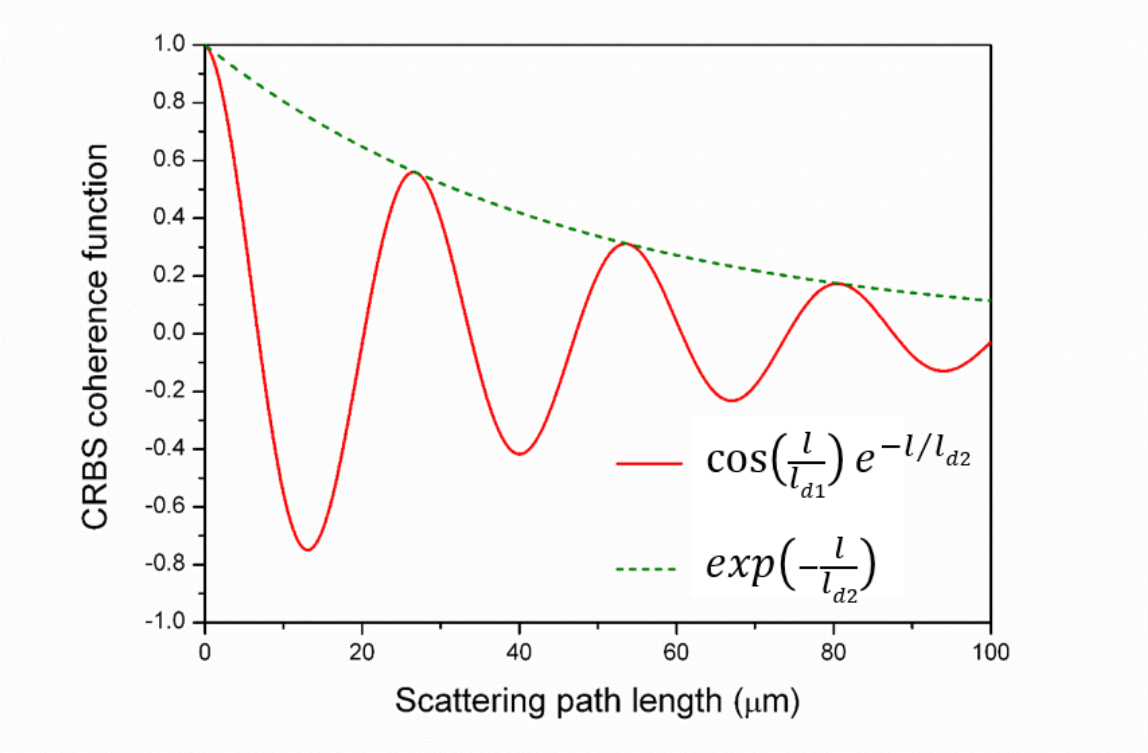

Figure 6.10: Plot of the real part of the global phase factor (coherence function) for the RCBS process, calculated with the following values of parameters $l_t = 0.2\,\mu m$, $\Delta k = 0.466\,\mu m^{-1}$, $l_{d1} = 4.3\,\mu m$, $l_{d2} = 46\,\mu m$.

6.2.2 Effect of dephasing on the enhancement factor

According the above discussion, we expect to observe the RCBS cone strongly influenced by dephasing, which modifies the most crossed term of the bistatic coefficient γ_c, describing the RCBS process, while leaves the ladder (incoherent) γ_l term unchanged. In particular, that leads to a reduced enhancement factor in the measured backscattered intensity.

Actually, the aforementioned effect of dephasing on the RCBS cone can be evaluated using the expressions for the time integrated diffusion probability (albedo) $\gamma = \gamma_c + \gamma_l$ and including the coherence function, described in the previous section, in the term γ_c only. If we include also the effect of the inelastic length we have the following expressions:

$$\gamma_l \propto \int_0^\infty t^{-\frac{3}{2}} e^{-\frac{t}{\tau_i}} \left(1 - e^{-\frac{t}{\tau_t}}\right) dt \tag{6.18}$$

$$\gamma_c \propto \int_0^\infty t^{-\frac{3}{2}} e^{-\frac{1}{3}(kl_t\psi)^2 \frac{t}{\tau_t}} e^{-3D\Delta k^2 \frac{t}{2}} \cos\left(\frac{3D\Delta k t}{2l_t}\right) e^{-\frac{t}{\tau_i}} \left(1 - e^{-\frac{t}{\tau_t}}\right) dt \quad (6.19)$$

where the term $\left(1 - e^{-\frac{t}{\tau_t}}\right)$ has been added to cut-off the integrals at small times. For convenience, we can express the integrals as a function of the scattering path length, which for $\psi = 0$ (i.e. in the exact backscattering direction) reads:

$$\gamma_l \propto \int_0^\infty l^{-\frac{3}{2}} e^{-\frac{l}{l_i}} \left(1 - e^{-\frac{l}{l_t}}\right) dl \quad (6.20)$$

$$\gamma_c \propto \int_0^\infty l^{-\frac{3}{2}} e^{-\frac{l}{d2}} \cos\left(\frac{l}{l_{d1}}\right) e^{-\frac{l}{l_i}} \left(1 - e^{\frac{l}{l_t}}\right) dl \quad (6.21)$$

The calculation of these integrals allows us to estimate the enhancement factor $\frac{\gamma_c+\gamma_l}{\gamma_l}$ as a function of the relevant parameters l_t, l_i and l_{d1}. Figure 6.11 shows the enhancement factor E_{Raman}, calculated using the above defined relations, as a function of both l_i and l_{d1}, normalized to the transport mean free path. As expected, for a given value of l_i, E_{Raman} increases by increasing the dephasing length l_{d1}. On the contrary, for a fixed value of l_{d1}, the dependence of E_{Raman} on l_i shows the opposite trend, leading to a lower enhancement for a longer l_i. This unusual behaviour is determined by the oscillating coherence function (see figure 6.10) entering the integral expression of the bistatic coefficient, which must be multiplied by the exponentially decaying function describing the absorption. Indeed, for large values of $l_i > l_{d1}$ this results in a strongly damped cosine function, whose average value may be significantly different from zero.

Searching for experimental confirmations, we pump sample 1 at three different laser wavelengths (488 nm, 532 nm and 785 nm). In this way, we span the range for which silicon nanowire material shows inelastic scattering lengths significantly different (between few microns and few tens of microns). Moreover, we further observe the RCBS enhancement (at 532 nm of wavelength) on sample 1 after the variation of its scattering strength by introducing a silicone oil (refractive index 1.46) into the interstices between Si NWs.

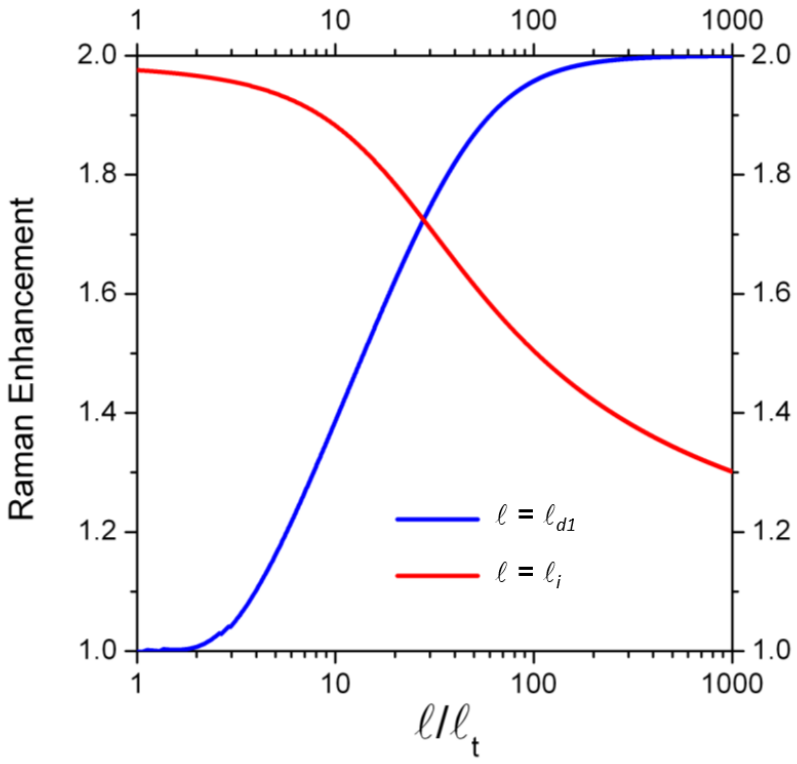

Figure 6.11: Theoretical Raman enhancement plotted versus the dephasing length l_{d1} (blue) and versus the inelastic length l_i (red), fixing $l_i = 8.1$ μm and $l_{d1} = 3.38$ μm, respectively [64].

All the experimental data are resumed and shown in figure 6.12, where the Raman backscattering signals (green dots) are compared to the corresponding Rayleigh CBS cones (blue dots). It strikes one immediately as the Raman cones display a more rounded tip and a lower enhancement factor, while a similar shape is found at large scattering angles. The best fits to the experimental data are indicated in figure 6.12 by the red lines, showing very good agreement in all cases. These are obtained by means of a modified fitting function (equations 3.18), in which we introduce the two linked characteristic lengths l_{d1} and l_{d2} to take in account of dephasing effects. Thus, the extinction coefficient becomes $\kappa_{ext\_C} = l_t^{-1} + l_i^{-1} - il_{d1}^{-1} + l_{d2}^{-1}$.

The introduction of these dephasing lengths implies a new expression for the coefficient α in γ_c (equation 3.13):

$$\alpha \equiv \sqrt{L_{abs}^{-2} + L_{d1}^{-2} + L_{d2}^{-2} + q_\perp^2} \tag{6.22}$$

where $L_{d1} = \sqrt{\frac{l_t i l_{d1}}{3}}$ and $L_{d2} = \sqrt{\frac{l_t l_{d2}}{3}}$ are the two new additional diffusion lengths. On the other hand, there is no variation in the expression of γ_l (equation 3.14), since it is evaluated at $q_\perp = 0$ and contains only the incoherent background of CBS signal. Even the theoretical enhancement factor $E = 1 + \frac{\gamma_c}{\gamma_l}$ is set $E = E_{Raman} < 2$ since $\frac{\gamma_c}{\gamma_l} < 1$ in the Raman case. This expression for the fitting function is particularly useful for RCBS because it allows us to extract the value of the enhancement factor $E = E_{Raman}$ as a fitting parameter for the backscattering cone excluding any spurious effect, which may reduce the measured intensity.

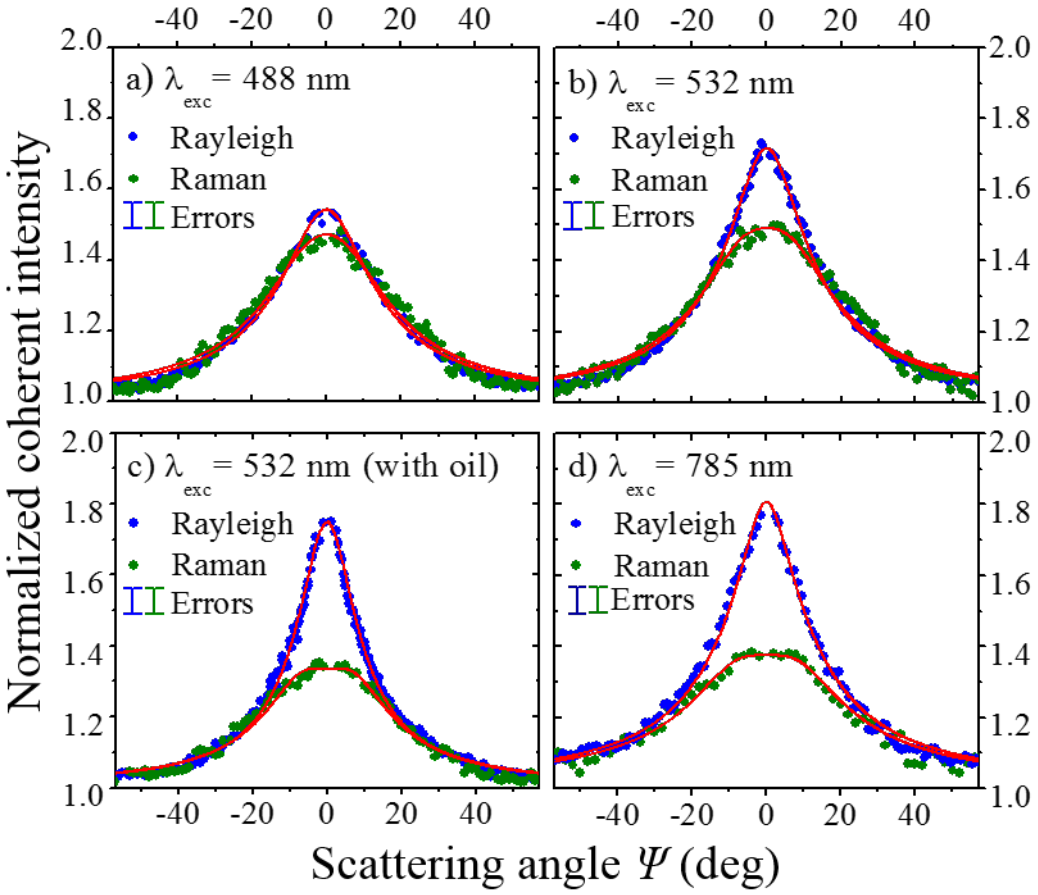

Figure 6.12: CBS cones for Rayleigh (blue dots) and Raman (green dots) scattering in sample 1 at different excitation wavelength: 488 nm (a), 532 nm, without (b) and with silicone oil filling (c), and 785 nm (d). The continuous red lines represents the best fitting curves [64].

Therefore the free fitting parameters for Raman cones are l_{d1} and E_{Raman}, while l_t and L_{eff} are fixed to the values found in the Rayleigh case, whose the fitting function is even defined as in equation 3.18. Note that $l_{d2} = l_{d1}^2/2l_t$ is not a free parameter. Finally the inelastic scattering length l_i is maintained fixed as in the case of Rayleigh CBS. The values of the relevant parameters obtained for sample 1 and sample 2 in different experimental conditions are summarizes in the table of figure 6.13. Here, we see that the values of l_{d1} determined from the best-fit are of the order of a few microns, while those of l_{d2} are in the range of a few tens of microns, in agreement with the predicted dephasing lengths calculated from Δk and l_t values in each case.

Sample	Fixed parameters CBS and CRBS				Fitting parameter				
					CBS		CRBS (l_t fixed)		
	$\lambda_{exc}(\mu m)$	n_{eff}	$a=z_0/l_t$	l_i (μm)	l_t (μm)	L_{eff}/l_t	E_{Raman}	$l_{d1}(\mu m)$	l_{d2} (μm)
1	0.488	1.40 ± 0.14	1.6	4.5	0.15 ± 0.02	18 ± 6	1.75 ± 0.08	3.9 ± 0.4	50 ± 10
	0.532	1.36 ± 0.14	1.5	8.1	0.17 ± 0.02	17 ± 5	1.62 ± 0.08	3.4 ± 0.3	34 ± 7
	0.785	1.32 ± 0.13	1.4	86.5	0.19 ± 0.02	13 ± 0.5	1.44 ± 0.07	5.6 ± 0.5	81 ± 13
1 + oil	0.532	1.72 ± 0.17	2.3	8.1	0.22 ±0.02	9 ± 0.5	1.45 ± 0.07	2.9 ± 0.3	19 ± 4
2	0.532	1.73 ± 0.25	2.3	3.8	0.48 ± 0.02	5 ± 0.2	1.28 ± 0.07	2.0 ± 0.4	4.0 ± 1.6

Figure 6.13: Table of parameters used in fitting procedures for respective CBS and RCBS cones. Here are listed the parameters values used in the fitting procedures for all measurement sets. In order, we fixed the excitation wavelength, the refractive index, the parameter a taking into account the internal reflection at the boundaries and the inelastic mean free path. The refractive index and the inelastic scattering length have been estimated by morphological analysis (SEM) and EDX spectroscopy. We fit the Rayleigh cones by using the transport mean free path and the effective thickness L_{eff} as free parameters, while we fixed them in the fitting procedures of Raman cones at the values obtained in CBS case. We adopted the dephasing length l_{d1} and the theoretical Raman enhancement E_{Raman} as fitting parameters of RCBS cones, while we evaluated the values of l_{d2} with the respective propagated errors [64].

Moreover we observe that lower enhancement factors E_{Raman} correspond to lower dephasing lengths. However, a direct relationship between l_{d1} and E_{Raman} cannot be established without considering the effect of the inelastic length l_i. Taking into account the effect of optical absorption, we can finally make a quantitative comparison of our experimental RCBS data with the theoretically predicted values of the Raman enhancement in the presence of dephasing, calculated by means of the model of section 6.2.2. This is reported in figure 6.14, where an almost perfect agreement between theoretical and experimental values of is found for all the measured samples. Notice that significant Raman enhancement factors are only possible when $l_{d1} > l_i$, which implies l_i values of the order of a few microns for typical vibrational frequencies in solid-state materials (we recall that $l_{d1} = 2\Delta k = 2c\Delta\omega$). The reason for this unexpected behaviour must be found in the peculiar coherence function governing the interference of multiply scattered Raman waves. Indeed, due to its fast oscillations as a function of the scattering path length, the coherence function would rapidly average out to zero in absence of optical absorption, thus yielding a vanishing contribution to the coherent term of the backscattered intensity with respect to the diffused (incoherent) one. On the contrary, the presence of absorption leads to a cut-off of the integral at long scattering paths for both the coherent and diffused contribution, thus making the coherent part of the backscattered intensity to emerge over the diffused one.

In conclusion, our findings state the first strong experimental evidence for a coherent Raman backscattering phenomenon, in close analogy with the coherent Rayleigh backscattering process, in strongly scattering materials. Here, the coherent nature of the Raman scattering processes manifests for the first time macroscopically in a bulk material through the observation of the coherent backscattering intensity in the angle-dependent Raman emission [64]. This occurrence establishes both the robustness of the coherent backscattering phenomenon and a new sound starting point towards unexplored phenomena in Raman scattering by disordered materials and non linear Raman effects that could lead to random Raman gain evidences.

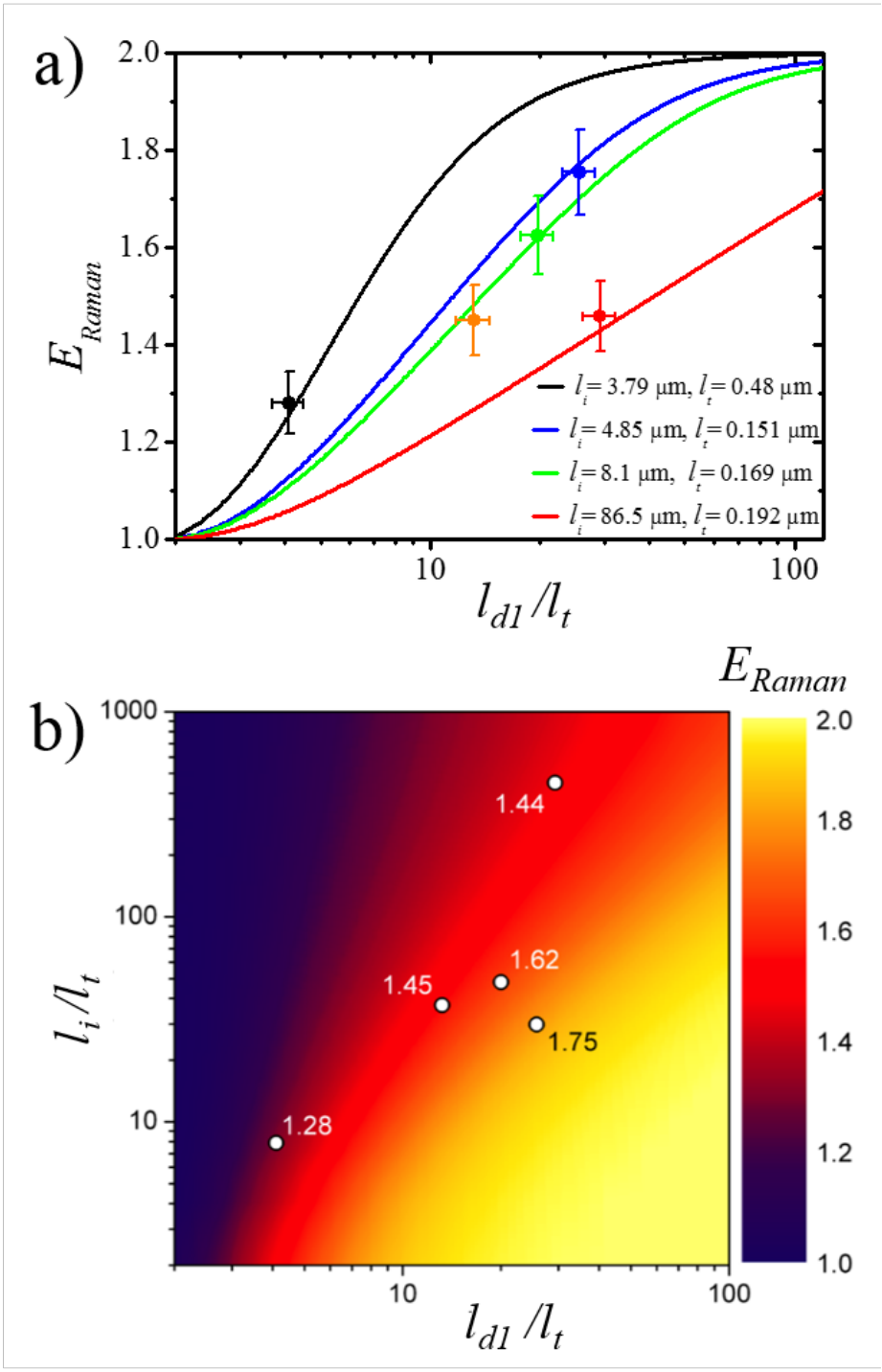

Figure 6.14: a) The Raman enhancement E_{Raman} as a function of the dephasing length l_{d1} (in units of l_t) for different inelastic lengths l_i. The dots represent the experimental data: sample 1 excited at 488, 532 and 785 nm (blue, green and red dots, respectively), sample 1 filled with silicone oil and excited at 532 nm (orange dot) and sample 2 excited at 532 nm (black dot). b) Contour plot of the theoretical E_{Raman} as a function of l_{d1} and l_i, both represented in units of l_t on logarithmic scales. White dots indicate experimental values [64].

Chapter 7

Conclusions and future perspectives

This thesis reports on the studies of the light scattering from disordered textures with high aspect ratio of roughness profile, that I carried out during my PhD in the *Photonics and Nanostructures group* at the Physics Department of the University of Pavia. The underlying theme of my research has been the enhancement of light scattering by coherent propagation of light into deep textured surfaces fabricated by auto-organized lithography processes, which are in principle scalable to large areas and make the optical properties of textures very robust against fabrication imperfections. In this thesis, I discuss how the optical properties, which these textures show in the whole visible range of the electromagnetic spectrum, are enhanced by strong light scattering. Indeed, I argue that such scattering is activated by the coexistence of order and disorder, which characterizes texture morphologies realized by means of auto-organized fabrication processes.

The aforementioned reasons motivate the research interests for auto-organized textured substrates. In fact, such substrates provide enhanced light-matter interactions on large areas, which are required in devices for sensing and photovoltaic applications. This point of view is elaborated in chapter 1.

The general goal of this thesis is to relate the enhanced of light scattering to the surface morphology of investigated samples. For this reason, chapter 2 presents a theoretical overview of elastic scattering of light, highlighting how the relative length scale of scatterers determines the scattering regime.

In my investigations, particular attention has been paid to experimental characterization of the angle resolved scattering (ARS) and to the anti-reflection properties of textures. To perform angle-resolved measurements we have used a home-made setup, described in chapter 3, which I contributed to build during the first year of my PhD.

Some results emerging from our experimental investigations have a wider breath than the initial aims, as it often happens in fundamental research. In particular, this is the case of the new fascinating phenomena emerging from the experimental investigations of coherent backscattering of light.
The main results of this thesis are summarized below.

Chapter 4 reports on experimental investigations of light scattering properties of a nanotextured substrate fabricated at the University of Genova in the group of F. Buatier de Mongeot by a self-organized procedure based on defocused Ion-Beam Sputtering (IBS). The sample surface characterized by means of statistical analysis of the texture profile shows a complex surface morphology, which combines a sub-micrometric random roughness with a deep and elongated pseudo-periodic pattern. Since we aimed to demonstrate the remarkable optical properties of this new substrate especially applied to thin-film SCs technology, we performed a comparison between our substrate and the Asahi-U glass, which is a textured substrate commonly employed for the fabrication of thin-film SCs.

We characterized the optical properties by means of both integrating sphere and ARS measurements of scattered light in transmission. The results of these experiments show a strongly improved Haze (ratio of diffused light on the total one) for the proposed self-organized texture with respect to that of the Asahi-U glass, which is remarkable considering that our texture is 1D while the Asahi-U texture is 2D. In principle, a more complete investigation should be done by measuring scattering at all angles of incidence and for all orientations of the incidence plane, although the conclusions given above are not expected to be modified. Both wavelength- and angular- dependence of the ARS are explained in terms of the morphological nature of the investigated substrate, finding agreement with that expected for Mie (Tyndall) scattering from a rough substrate. In fact, the ARS measured on our sample is

broadly similar to those of an isotropic (Lambertian) scatterer, but in addition it displays angular peaks that we call *super-Lambertian*. These peaks are a consequence of the pseudo-periodic nature of ripples, as derived from the height-height correlation function. Therefore, the angular distribution of the scattering has a diffusive part related to the roughness and a diffractive part that follows from the pseudo-periodic nature of the nanotextured surface. The scattering properties of this nanotextured substrate follow from the complex nature of the surface morphology, which includes random roughness with submicrometric correlation length as well as some degree of 1-dimensional periodic ordering. That is a good example of how the combination of randomness and order in a texture gives rise to peculiar features in the light scattering, which have interesting applications for the light-trapping in thin-film SCs.

More generally, the enhancement of a photon-to-electron conversion in the active medium is an appealing goal also for crystalline SCs. This is achievable by means of a light-trapping strategy, among which the surface texturing of SC is one of the most effective. In this case it is possible to realize the texture directly on the absorbing layer. For this scope, the IBS technique is also suited despite the hardness of the crystalline nature of layers.

In chapter 5 we have investigated a different light-trapping scheme, which is based on multiple scattering of light. Here the texture consists in an array of vertically aligned densely packed silicon nanowires (Si NWs) realized at the CNR-IMM institute in Messina and Catania (group of A. Irrera and F. Priolo) by means of a metal-assisted wet etching process. The latter is an inexpensive and industrially-compatible fabrication method, in which gold or silver nanoparticles act as precursors in the erosion of silicon. The resulting textures have a novel planar random geometry, whose fractal characteristics determine the fascinating optical properties we have investigated. The NW samples show total reflectance values around 1% in whole visible spectrum, which goes down to 0.1% when the incident wavelength matches the maximum heterogeneity size exhibited by the arrangement of Si NWs. We relate this high light-trapping efficiency to multiple scattering propagation of radiation in the array plane, which is promoted by a dense fractal arrangement of the NWs. The very low measured reflectance values place the investigated structures among the

most appropriate silicon-based architectures for applications in which a strong light-matter interaction is required (like photonic sensing, photovoltaic and photo-catalysis devices). Moreover, the internal multiple scattering processes are also responsible for a strong photoluminescence scattering from the Si NW array. This could open the way towards a number of new photonic applications of silicon as a light source. Furthermore, these samples have an enhancement of Raman emission due to multiple scattering processes. We have demonstrated the dependence of this Raman enhancement on the lacunarity of the fractal morphology of the samples.

Chapter 6 reports on investigations of coherent backscattering of light (CBS), which we have performed on Si NW samples. In fact, we expected the occurrence of CBS of light in Si NW samples because of the strong scattering properties of Si NWs and the multiple scattering of light established in the NW array. The enhancement of the Rayleigh light in backscattering direction results from the typical conical shape of the angle resolved scattering. Therefore we have explored the angular dependence of backscattered light from two Si NW samples, which differ in morphology. Actually the CBS cones of our NW samples show a much larger FWHM than that observed in common turbid media. Such a result indicates that light travels a mean distance into NW arrays, which is much shorter than the length of the mean optical path. The experimental data have been fitted by the *finite slab* model for the CBS of light, whose parameters characterize the phenomenon. The latter observation is a further confirmation of the strength of light scattering in our Si NWs and, moreover, it provides an estimation of light trapping taking place into our samples.

Furthermore, we have provided the first experimental observation for the coherent nature of spontaneous Raman scattering at a macroscopic length scale in a bulk material (whereas it typically occurs on a nanometer length scale). In fact, because of the aforementioned evidences of Raman enhancement mediated by multiple scattering of light, we characterized the angular dependence of the Raman emission intensity searching for coherent back scattering evidences in analogy to that of Rayleigh light. In the second part of chapter 6, we theoretically explain the appearance of a CBS cone for Raman

light by means of a reciprocal *hybrid Rayleigh-Raman* paths model, for which optical coherence is provided by both the symmetry of the Raman tensor and the short dwell time of light inside the material. Actually the Raman CBS cones appear lower and flatter than Rayleigh ones. In order to account for this phenomenon in a quantitative way, we have extended the classical theory of CBS to the case of Raman light, considering the Stokes shift in the diagrammatic expansions of Green functions. In fact a certain dephasing is accumulated between wave functions of the reciprocal paths, which are now generally asymmetric because of the scattering event of Raman light generation. We have statistically treated the dephasing for all possible combinations of reciprocal paths in order to obtain a single dephasing factor, which globally affects the bistatic factor determining the CBS enhancement. We highlight that this global dephasing factor presents an oscillating exponential in addition to classical damping. This new theory, developed in collaboration with the group of D. Wiersma in Florence, perfectly matches our experimental observations as demonstrated by the very good agreement between the data and the modified finite slab model used for fitting. In this model, the effects of the global dephasing factor are described by introducing two new characteristic (dephasing) lengths, which depend on the Stokes shift. Finally, we have studied the trend of this new model with the characteristic lengths of the system. Surprisingly, an appreciable enhancement of Raman CBS is determined by the presence of absorption in the system, whose associated characteristic (inelastic) length has be comparable to the shorter of two dephasing lengths. Otherwise the oscillating nature of the global dephasing factor averages the enhancement of Raman CBS to zero.

I am going to conclude my thesis talking about feature perspectives of the aforementioned research, whose themes encompass the study of texture morphologies and optical properties, as well as the theoretical correlation between these two.

From the point of view of texture morphology, we highlight that the presented light scattering performances are obtained in spite of the low dimensionality of the textures, i.e., one-dimensional for the textured glass and two-dimensional for the Si NW arrays. Therefore we believe that scattering strength

of textures could be further improved by developing fabrication techniques, which enable a three-dimensional shaping of textures. Nowadays the fabrication of similar complex photonic structures needs several lithographic stages to merge random and periodic patterns. We stress that the self-organized nanopatterning approaches, described in this thesis, are potentially scalable to larger scales employing conventional industrial equipment. The use of such substrates can prove useful for light trapping applications in which strong and broadband light-matter interaction is required.

Particularly the IBS textured glass allows the growth of transparent electrodes to be employed in solar water splitting applications or in the superstrate configuration growth of thin-film SCs [78]. An even greater improvement of J_{sc} is expected using crystalline or micro-crystalline silicon, as their lower band gap allows for a higher enhancement of absorption in the near-infrared spectral range. More in general, the ability to form high aspect ratio textured patterns at the interfaces of low cost materials will prove of interest in a broad range of applications involving e.g. the confinement of metallic nanostructures for plasmonics, controlled wettability and adhesion, etc. Unfortunately the realization of deep roughness is difficult because of the concomitance of hardness (and, when applicable, amorphous nature) of silicon. A breakthrough may come from the metal-assisted wet etching technique, which allows to realize a very high aspect ratio texture in silicon.

Finally, we remark that such deep textures have demonstrated enhanced optical properties due to the very strong scattering strength, which is typically considered a prerequisite for light localization. However the observation of such a subtle phenomenon needs further investigations. For this purpose we envisage the implementation of a Monte Carlo model to theoretically treat the light propagation into our samples and to compare it with ad-hoc experiments.

Bibliography

[1] Randolph Kirchain and Lionel Kimerling. A roadmap for nanophotonics. *Nature Photonics*, 1(6):303–305, 2007.

[2] John D Joannopoulos, Pierre R Villeneuve, Shanhui Fan, et al. Photonic crystals: putting a new twist on light. *Nature*, 386(6621):143–149, 1997.

[3] Eli Yablonovitch. Inhibited spontaneous emission in solid-state physics and electronics. *Phys. Rev. Lett.*, 58:2059–2062, May 1987.

[4] Sajeev John. Strong localization of photons in certain disordered dielectric superlattices. *Phys. Rev. Lett.*, 58:2486–2489, Jun 1987.

[5] Francesco Priolo, Tom Gregorkiewicz, Matteo Galli, and Thomas F Krauss. Silicon nanostructures for photonics and photovoltaics. *Nature Nanotechnology*, 9(1):19–32, 2014.

[6] Diederik S Wiersma. Disordered photonics. *Nature Photonics*, 7(3):188–196, 2013.

[7] Filippo Alpeggiani, Lucio Claudio Andreani, and Dario Gerace. Effective bichromatic potential for ultra-high q-factor photonic crystal slab cavities. *Applied Physics Letters*, 107(26), 2015.

[8] Hiroshi Sekoguchi, Yasushi Takahashi, Takashi Asano, and Susumu Noda. Photonic crystal nanocavity with a q-factor of 9 million. *Opt. Express*, 22(1):916–924, Jan 2014.

[9] Yuta Ooka, Tomohiro Tetsumoto, Akihiro Fushimi, Wataru Yoshiki, and Takasumi Tanabe. Cmos compatible high-q photonic crystal nanocavity

fabricated with photolithography on silicon photonic platform. *Sci. Rep.*, 5, 2015.

[10] Zhi-Yuan Li and Zhao-Qing Zhang. Fragility of photonic band gaps in inverse-opal photonic crystals. *Phys. Rev. B*, 62:1516–1519, Jul 2000.

[11] Zhi-Yuan Li, Xiangdong Zhang, and Zhao-Qing Zhang. Disordered photonic crystals understood by a perturbation formalism. *Phys. Rev. B*, 61:15738–15748, Jun 2000.

[12] Mehmet Bayindir, E Cubukcu, I Bulu, T Tut, E Ozbay, and C M Soukoulis. Photonic band gaps, defect characteristics, and waveguiding in two-dimensional disordered dielectric and metallic photonic crystals. *Phys. Rev. B*, 64:195113, Oct 2001.

[13] Vincenzo Savona. Electromagnetic modes of a disordered photonic crystal. *Phys. Rev. B*, 83:085301, Feb 2011.

[14] Luis Guillermo Villanueva, Oscar Vazquez-Mena, Cristina Martin-Olmos, Veronica Savu, Katrin Sidler, and Juergen Brugger. Resistless fabrication of nanoimprint lithography (nil) stamps using nano-stencil lithography. *Micromachines*, 4(4):370, 2013.

[15] Sameh Tawfick, Michael De Volder, Davor Copic, Sei Jin Park, C Ryan Oliver, Erik S Polsen, Megan J Roberts, and A John Hart. Engineering of micro- and nanostructured surfaces with anisotropic geometries and properties. *Advanced Materials*, 24(13):1628–1674, 2012.

[16] Alan Goodrich, Peter Hacke, Qi Wang, Bhushan Sopori, Robert Margolis, Ted L James, and Michael Woodhouse. A wafer-based monocrystalline silicon photovoltaics road map: Utilizing known technology improvement opportunities for further reductions in manufacturing costs. *Solar Energy Materials and Solar Cells*, 114:110–135, 2013.

[17] Corsin Battaglia, Ching-Mei Hsu, Karin Söderström, Jordi Escarre, Franz-Josef Haug, Mathieu Charriére, Mathieu Boccard, Matthieu Despeisse, Duncan TL Alexander, Marco Cantoni, et al. Light trapping in solar cells: can periodic beat random? *ACS Nano*, 6(3):2790–2797, 2012.

[18] Simone Zanotto, Marco Liscidini, and Lucio Claudio Andreani. Light trapping regimes in thin-film silicon solar cells with a photonic pattern. *Opt. Express*, 18(5):4260–4272, Mar 2010.

[19] Angelo Bozzola, Marco Liscidini, and Lucio Claudio Andreani. Photonic light-trapping versus lambertian limits in thin film silicon solar cells with 1d and 2d periodic patterns. *Opt. Express*, 20(S2):A224–A244, Mar 2012.

[20] F J Haug, K Söderström, A Naqavi, and C Ballif. Resonances and absorption enhancement in thin film silicon solar cells with periodic interface texture. *Journal of Applied Physics*, 109(8), 2011.

[21] Andrej Čampa, Olindo Isabella, Rob van Erven, Patrick Peeters, Herman Borg, Janez Krč, Marko Topič, and Miro Zeman. Optimal design of periodic surface texture for thin-film a-si:h solar cells. *Progress in Photovoltaics: Research and Applications*, 18(3):160–167, 2010.

[22] Angelo Bozzola, Marco Liscidini, and Lucio Claudio Andreani. Broadband light trapping with disordered photonic structures in thin-film silicon solar cells. *Progress in Photovoltaics: Research and Applications*, 22(12):1237–1245, 2014.

[23] E Fornies, C Zaldo, and JM Albella. Control of random texture of monocrystalline silicon cells by angle-resolved optical reflectance. *Solar Energy Materials and Solar Cells*, 87(1):583–593, 2005.

[24] Lucia V Mercaldo, Paola Delli Veneri, Iurie Usatii, and Tiziana Polichetti. Broadband near-field effects for improved thin film si solar cells on randomly textured substrates. *Solar Energy Materials and Solar Cells*, 112:163–167, 2013.

[25] Piotr Kowalczewski, Marco Liscidini, and Lucio Claudio Andreani. Engineering gaussian disorder at rough interfaces for light trapping in thin-film solar cells. *Opt. Lett.*, 37(23):4868–4870, Dec 2012.

[26] Piotr Kowalczewski, Marco Liscidini, and Lucio Claudio Andreani. Light trapping in thin-film solar cells with randomly rough and hybrid textures. *Opt. Express*, 21(S5):A808–A820, Sep 2013.

[27] Samuel Wiesendanger, Mathias Zilk, Thomas Pertsch, Carsten Rockstuhl, and Falk Lederer. Combining randomly textured surfaces and photonic crystals for the photon management in thin film microcrystalline silicon solar cells. *Optics Express*, 21(103):A450–A459, 2013.

[28] Filippo Pratesi, Matteo Burresi, Francesco Riboli, Kevin Vynck, and Diederik S Wiersma. Disordered photonic structures for light harvesting in solar cells. *Opt. Express*, 21(S3):A460–A468, May 2013.

[29] Z Valy Vardeny, Ajay Nahata, and Amit Agrawal. Optics of photonic quasicrystals. *Nature Photonics*, 7(3):177–187, 2013.

[30] Juan F Galisteo-López, Marta Ibisate, Riccardo Sapienza, Luis S Froufe-Pérez, Álvaro Blanco, and Cefe López. Self-assembled photonic structures. *Advanced Materials*, 23(1):30–69, 2011.

[31] Marian Florescu, Salvatore Torquato, and Paul J Steinhardt. Designer disordered materials with large, complete photonic band gaps. *Proceedings of the National Academy of Sciences*, 106(49):20658–20663, 2009.

[32] Ping Sheng. *Introduction to wave scattering, localization and mesoscopic phenomena*, volume 88. Springer Science & Business Media, 2006.

[33] A Yariv and P Yeh. *Optical waves in crystal propagation and control of laser radiation*. John Wiley and Sons, Inc.,New York, NY, Jan 1983.

[34] E Yablonovitch, T J Gmitter, R D Meade, A M Rappe, K D Brommer, and J D Joannopoulos. Donor and acceptor modes in photonic band structure. *Phys. Rev. Lett.*, 67:3380–3383, Dec 1991.

[35] P W Anderson. Absence of diffusion in certain random lattices. *Phys. Rev.*, 109:1492–1505, Mar 1958.

[36] Eugene Hecht and Alfred Zajac. *Optics*. Addison-Wesley Publishing Company, 1974.

[37] G Mie and P Debye Ann. Physik, 25 (1908). *Ann. Physik*, 30:57, 1909.

[38] Max Born and Emil Wolf. *Principles of Optics, seventh expanded edition*. Cambridge, England, 1999.

[39] John D Jackson. *Classical Electrodynamics, 3rd ed.*, volume 67. American Journal of Physics, 1999.

[40] Alexander V Tikhonravov, Michael K Trubetskov, Andrei A Tikhonravov, and Angela Duparré. Effects of interface roughness on the spectral properties of thin films and multilayers. *Appl. Opt.*, 42(25):5140–5148, Sep 2003.

[41] H E Bennett and J O Porteus. Relation between surface roughness and specular reflectance at normal incidence. *J. Opt. Soc. Am.*, 51(2):123–129, Feb 1961.

[42] Alexei A Maradudin. *Light scattering and nanoscale surface roughness*. Springer Science & Business Media, 2010.

[43] Wei-Lun Min, Bin Jiang, and Peng Jiang. Bioinspired self-cleaning antireflection coatings. *Advanced Materials*, 20(20):3914–3918, 2008.

[44] Pete Vukusic and J Roy Sambles. Photonic structures in biology. *Nature*, 424(6950):852–855, 2003.

[45] Ralf Lenke and Georg Maret. Multiple scattering of light: Coherent backscattering and transmission. In Wyn Brown, editor, *Scattering in polymeric and colloidal systems*, pages 1–71. Gordon & Breach, Amsterdam, 2000.

[46] Diederik S Wiersma. Light in strongly scattering and amplifying random media. *PhD Thesis University of Amsterdam*, 1995.

[47] Sajeev John. Localization and absorption of waves in a weakly dissipative disordered medium. *Phys. Rev. B*, 31:304–309, Jan 1985.

[48] Diederik S Wiersma, Paolo Bartolini, Ad Lagendijk, and Roberto Righini. Localization of light in a disordered medium. *Nature*, 390(6661):671–673, 1997.

[49] Mordechai Segev, Yaron Silberberg, and Demetrios N Christodoulides. Anderson localization of light. *Nature Photonics*, 7(3):197–204, 2013.

[50] Diederik S Wiersma. The physics and applications of random lasers. *Nature physics*, 4(5):359–367, 2008.

[51] Yasuo Kuga and Akira Ishimaru. Retroreflectance from a dense distribution of spherical particles. *J. Opt. Soc. Am. A*, 1(8):831–835, Aug 1984.

[52] Meint P Van Albada and Ad Lagendijk. Observation of weak localization of light in a random medium. *Phys. Rev. Lett.*, 55:2692–2695, Dec 1985.

[53] Costanza Toninelli. Light transport in photonic structures: interplay between order and disorder. *PhD Thesis University of Florence*, 2007.

[54] E Larose, L Margerin, B A van Tiggelen, and M Campillo. Weak localization of seismic waves. *Phys. Rev. Lett.*, 93:048501, Jul 2004.

[55] C Fort, L Fallani, V Guarrera, J E Lye, M Modugno, D S Wiersma, and M Inguscio. Effect of optical disorder and single defects on the expansion of a bose-einstein condensate in a one-dimensional waveguide. *Phys. Rev. Lett.*, 95:170410, Oct 2005.

[56] Eric Akkermans and Gilles Montambaux. *Mesoscopic physics of electrons and photons*. Cambridge University Press, 2007.

[57] D Vollhardt and P Wölfle. Diagrammatic, self-consistent treatment of the anderson localization problem in $d \leq 2$ dimensions. *Phys. Rev. B*, 22:4666–4679, Nov 1980.

[58] Erik Garnett and Peidong Yang. Light trapping in silicon nanowire solar cells. *Nano Letters*, 10(3):1082–1087, 2010.

[59] Klaus Jäger. *On the Scalar Scattering Theory for Thin-Film Solar Cells*. TU Delft, Delft University of Technology, 2012.

[60] Sven Schröder, Tobias Herffurth, Holger Blaschke, and Angela Duparré. Angle-resolved scattering: an effective method for characterizing thin-film coatings. *Appl. Opt.*, 50(9):C164–C171, 2011.

[61] D Dominé, F J Haug, Corsin Battaglia, and Christophe Ballif. Modeling of light scattering from micro-and nanotextured surfaces. *Journal of Applied Physics*, 107(4):044504, 2010.

[62] J Krč, M Zeman, F Smole, and M Topič. Optical modeling of a-si: H solar cells deposited on textured glass/sno2 substrates. *Journal of Applied Physics*, 92(2):749–755, 2002.

[63] Barbara Fazio, Pietro Artoni, Maria Antonia Iatì, Cristiano D'andrea, Maria Josè Lo Faro, Salvatore Del Sorbo, Stefano Pirotta, Pietro Giuseppe Gucciardi, Paolo Musumeci, Cirino Salvatore Vasi, et al. Strongly enhanced light trapping in a two-dimensional silicon nanowire random fractal array. *Light: Science & Applications*, 5(4):e16062, 2016.

[64] Barbara Fazio, Alessia Irrera, Stefano Pirotta, Cristiano D'Andrea, Salvatore Del Sorbo, Maria Josè Lo Faro, Pietro Giuseppe Gucciardi, Maria Antonia Iatì, Rosalba Saija, Maddalena Patrini, et al. Coherent backscattering of raman light. *Nature Photonics*, 11(3):170–176, 2017.

[65] O L Muskens and A Lagendijk. Broadband enhanced backscattering spectroscopy of strongly scattering media. *Opt. Express*, 16(2):1222–1231, Jan 2008.

[66] Stefano Pirotta. Enhanced light-matter interaction in photonic nanostructures. *PhD Thesis University of Pavia*, 2015.

[67] HC van de Hulst and R Stark. Accurate eigenvalues and exact extrapolation lengths in radiative transfer. *Astronomy and Astrophysics*, 235:511–520, 1990.

[68] Martin B van der Mark, Meint P van Albada, and Ad Lagendijk. Light scattering in strongly scattering media: Multiple scattering and weak localization. *Phys. Rev. B*, 37:3575–3592, Mar 1988.

[69] Akkermans, E, Wolf, P E, Maynard, R, and Maret, G. Theoretical study of the coherent backscattering of light by disordered media. *J. Phys. France*, 49(1):77–98, 1988.

[70] Ad Lagendijk, Rob Vreeker, and Pedro De Vries. Influence of internal reflection on diffusive transport in strongly scattering media. *Physics Letters A*, 136(1):81 – 88, 1989.

[71] J X Zhu, D J Pine, and D A Weitz. Internal reflection of diffusive light in random media. *Phys. Rev. A*, 44:3948–3959, Sep 1991.

[72] Eli Yablonovitch and George D Cody. Intensity enhancement in textured optical sheets for solar cells. *IEEE Transactions on Electron Devices*, 29(2):300–305, 1982.

[73] Hiroomi Shimomura, Zekeriyya Gemici, Robert E Cohen, and Michael F Rubner. Layer-by-layer-assembled high-performance broadband antireflection coatings. *ACS Applied Materials & Interfaces*, 2(3):813–820, 2010.

[74] Karin So¨ derstro¨ m, Franz-Josef Haug, Jordi Escarre, Oscar Cubero, and Christophe Ballif. Photocurrent increase in nip thin film silicon solar cells by guided mode excitation via grating coupler. *Applied Physics Letters*, 96(21):213508, 2010.

[75] K Jäger, M Fischer, RACMM Van Swaaij, and M Zeman. A scattering model for nano-textured interfaces and its application in opto-electrical simulations of thin-film silicon solar cells. *Journal of Applied Physics*, 111(8):083108, 2012.

[76] D Chiappe, A Toma, Z Zhang, C Boragno, and F Buatier de Mongeot. Amplified nanopatterning by self-organized shadow mask ion lithography. *Applied Physics Letters*, 97(5):053102, 2010.

[77] ZQ Zhang, D Chiappe, A Toma, C Boragno, JD Guo, EG Wang, and F Buatier de Mongeot. Gaas nanostructuring by self-organized stencil mask ion lithography. *Journal of Applied Physics*, 110(11):114321, 2011.

[78] C Martella, D Chiappe, P Delli Veneri, LV Mercaldo, I Usatii, and F Buatier de Mongeot. Self-organized broadband light trapping in thin film amorphous silicon solar cells. *Nanotechnology*, 24(22):225201, 2013.

[79] A Toma, D Chiappe, B Šetina Batič, M Godec, M Jenko, and F Buatier de Mongeot. Erosive versus shadowing instabilities in the self-organized ion patterning of polycrystalline metal films. *Physical Review B*, 78(15):153406, 2008.

[80] A Toma, B Šetina Batič, D Chiappe, C Boragno, U Valbusa, M Godec, M Jenko, and F Buatier de Mongeot. Patterning polycrystalline thin films by defocused ion beam: the influence of initial morphology on the evolution of self-organized nanostructures. *Journal of Applied Physics*, 104(10):104313, 2008.

[81] C Deumié, Hugues Giovannini, and Claude Amra. Ellipsometry of light scattering from multilayer coatings. *Applied Optics*, 35(28):5600–5608, 1996.

[82] I Horcas, Rs Fernández, JM Gomez-Rodriguez, J Colchero, JWSXM Gómez-Herrero, and AM Baro. Wsxm: a software for scanning probe microscopy and a tool for nanotechnology. *Review of Scientific Instruments*, 78(1):013705, 2007.

[83] Rodolfo Cuerno and Albert-László Barabási. Dynamic scaling of ion-sputtered surfaces. *Physical Review Letters*, 74(23):4746, 1995.

[84] A-L Barabási and Harry Eugene Stanley. *Fractal concepts in surface growth*. Cambridge university press, 1995.

[85] William M Tong and R Stanley Williams. Kinetics of surface growth: phenomenology, scaling, and mechanisms of smoothening and roughening. *Annual Review of Physical Chemistry*, 45(1):401–438, 1994.

[86] Elliott A Eklund, R Bruinsma, J Rudnick, and R Stanley Williams. Submicron-scale surface roughening induced by ion bombardment. *Physical Review Letters*, 67(13):1759, 1991.

[87] Christopher C Umbach, Randall L Headrick, and Kee-Chul Chang. Spontaneous nanoscale corrugation of ion-eroded sio 2: the role of ion-irradiation-enhanced viscous flow. *Physical Review Letters*, 87(24):246104, 2001.

[88] Matthew M Braun and Laurent Pilon. Effective optical properties of non-absorbing nanoporous thin films. *Thin Solid Films*, 496(2):505–514, 2006.

[89] Erik C Garnett, Mark L Brongersma, Yi Cui, and Michael D McGehee. Nanowire solar cells. *Annual Review of Materials Research*, 41:269–295, 2011.

[90] Kohei Mizuno, Juntaro Ishii, Hideo Kishida, Yuhei Hayamizu, Satoshi Yasuda, Don N Futaba, Motoo Yumura, and Kenji Hata. A black body absorber from vertically aligned single-walled carbon nanotubes. *Proceedings of the National Academy of Sciences*, 106(15):6044–6047, 2009.

[91] LL Ma, YC Zhou, N Jiang, X Lu, J Shao, W Lu, J Ge, XM Ding, and XY Hou. Wide-band "black silicon" based on porous silicon. *Applied Physics Letters*, 88(17):171907, 2006.

[92] A Irrera, P Artoni, F Iacona, E F Pecora, G Franzò, M Galli, B Fazio, S Boninelli, and F Priolo. Quantum confinement and electroluminescence in ultrathin silicon nanowires fabricated by a maskless etching technique. *Nanotechnology*, 23(7):075204, 2012.

[93] Armin Bunde and Shlomo Havlin. *Fractals and disordered systems*. Springer Science & Business Media, 2012.

[94] V Krachmalnicoff, E Castanié, Y De Wilde, and R Carminati. Fluctuations of the local density of states probe localized surface plasmons on disordered metal films. *Phys. Rev. Lett.*, 105:183901, Oct 2010.

[95] Mark I Stockman. Inhomogeneous eigenmode localization, chaos, and correlations in large disordered clusters. *Phys. Rev. E*, 56:6494–6507, Dec 1997.

[96] VA Podolskiy and VM Shalaev. Giant optical responses in microcavity-fractal composites. *LASER PHYSICS-LAWRENCE-*, 11(1):26–30, 2001.

[97] K Foroutan-pour, P Dutilleul, and D.L Smith. Advances in the implementation of the box-counting method of fractal dimension estimation. *Applied Mathematics and Computation*, 105(2):195 – 210, 1999.

[98] A Karperien. Fraclac is for digital image analysis 1999–2013. http://rsb.info.nih.gov/ij/plugins/fraclac/FLHelp/Introduction.htm.

[99] RF Voss, RB Laibowitz, and EI Alessandrini. Percolation and fractal properties of thin gold films. In *The Mathematics and Physics of Disordered Media: Percolation, Random Walk, Modeling, and Simulation*, pages 153–168. Springer, 1983.

[100] Yi-Fan Huang, Surojit Chattopadhyay, Yi-Jun Jen, Cheng-Yu Peng, Tze-An Liu, Yu-Kuei Hsu, Ci-Ling Pan, Hung-Chun Lo, Chih-Hsun Hsu, Yuan-Huei Chang, et al. Improved broadband and quasi-omnidirectional anti-reflection properties with biomimetic silicon nanostructures. *Nature Nanotechnology*, 2(12):770–774, 2007.

[101] DE Aspnes and AA Studna. Dielectric functions and optical parameters of si, ge, gap, gaas, gasb, inp, inas, and insb from 1.5 to 6.0 ev. *Physical Review B*, 27(2):985, 1983.

[102] Von DAG Bruggeman. Berechnung verschiedener physikalischer konstanten von heterogenen substanzen. i. dielektrizitätskonstanten und leitfähigkeiten der mischkörper aus isotropen substanzen. *Annalen der Physik*, 416(7):636–664, 1935.

[103] Vincent C Holmberg, Timothy D Bogart, Aaron M Chockla, Colin M Hessel, and Brian A Korgel. Optical properties of silicon and germanium nanowire fabric. *The Journal of Physical Chemistry C*, 116(42):22486–22491, 2012.

[104] Otto L Muskens, Silke L Diedenhofen, Bernard C Kaas, Rienk E Algra, Erik PAM Bakkers, Jaime Gomez Rivas, and Ad Lagendijk. Large photonic strength of highly tunable resonant nanowire materials. *Nano Letters*, 9(3):930–934, 2009.

[105] Vladimir Poborchii, Tetsuya Tada, Yukinori Morita, Toshihiko Kanayama, and Pavel I Geshev. High near-ultraviolet raman efficiency of silicon nanowires with small cross sections. *Phys. Rev. B*, 83:153412, Apr 2011.

[106] Jian-An Huang, Ying-Qi Zhao, Xue-Jin Zhang, Lin-Bao Luo, Yan-Kuan Liu, Juan Antonio Zapien, Charles Surya, and Shuit-Tong Lee. Enhanced

raman scattering from vertical silicon nanowires array. *Applied Physics Letters*, 98(18):183108, 2011.

[107] M Khorasaninejad, N Dhindsa, J Walia, S Patchett, and SS Saini. Highly enhanced raman scattering from coupled vertical silicon nanowire arrays. *Applied Physics Letters*, 101(17):173114, 2012.

[108] R Sapienza, S Mujumdar, C Cheung, A G Yodh, and D Wiersma. Anisotropic weak localization of light. *Phys. Rev. Lett.*, 92:033903, Jan 2004.

[109] A Kastler. The raman effect and multiple scattering of light. *Proceedings of the Indian Academy of Sciences - Section A*, 8(5):476–482, 1938.

[110] Andreas Otto. Theory of first layer and single molecule surface enhanced raman scattering. *Phys. Stat. Sol. A*, 188(4):1455–1470, 2001.

[111] Ryan Beams, Luiz Gustavo Cançado, Sang-Hyun Oh, Ado Jorio, and Lukas Novotny. Spatial coherence in near-field raman scattering. *Phys. Rev. Lett.*, 113:186101, Oct 2014.

[112] R Loudon. Theory of the first-order raman effect in crystals. *Proceedings of the Royal Society of London A: Mathematical, Physical and Engineering Sciences*, 275(1361):218–232, 1963.

[113] YU Peter and M Cardona. *Fundamentals of semiconductors: physics and materials properties*. Springer Science & Business Media, 2010.

[114] R Loudon. The raman effect in crystals. *Advances in Physics*, 13(52):423–482, 1964.

[115] Jeffrey J Letcher, Kwangu Kang, David G Cahill, and Dana D Dlott. Effects of high carrier densities on phonon and carrier lifetimes in si by time-resolved anti-stokes raman scattering. *Applied Physics Letters*, 90(25):252104, 2007.

[116] Asegun S Henry and Gang Chen. Spectral phonon transport properties of silicon based on molecular dynamics simulations and lattice dynamics. *Journal of Computational and Theoretical Nanoscience*, 5(2):141–152, 2008.

List of publications

This thesis is based on the following works:

Coherent backscattering of Raman light,
B. Fazio, A. Irrera, S. Pirotta, C. D'Andrea, S. Del Sorbo, M. J. Lo Faro, P. G. Gucciardi, M. A. Iatì, R. Saija, M. Patrini, P. Musumeci, C. S. Vasi, D. S. Wiersma, M. Galli and F. Priolo,
Nature Photonics 11 (3): 170–176, 2017.
Paper DOI: 10.1038/NPHOTON.2016.278
Abstract: Coherent backscattering of light is observed when electromagnetic waves undergo multiple scattering within a disordered optical medium. So far, coherent backscattering of light has been studied extensively for elastic (or Rayleigh) light scattering. The occurrence of inelastic scattering affects the visibility of the backscattering effect by reducing the degree of optical coherence in the diffusion process. Here, we discuss the first experimental observation of a constructive interference effect in the inelastically backscattered Raman radiation from strongly diffusing silicon nanowire random media. The observed phenomenon originates from the coherent nature of the Raman scattering process, which typically occurs on a scale given by the phonon coherence length. We interpret our results in the context of a theoretical model of mixed Rayleigh–Raman random walks to shed light on the role of phase coherence in multiple scattering phenomena.

Light scattering properties of self-organized nanostructured substrates for thin-film solar cells
S. Del Sorbo, S. Pirotta, M. Galli, L. C. Andreani, C. Mennucci, C. Martella, M. C. Giordano and F. Buatier de Mongeot,
Nanotechnology, revised manuscript in preparation after a first round of review.
Abstract: We investigate the scattering properties of a novel kind of nano-textured substrates, fabricated in a self-organized fashion by defocused ion beam sputtering. These substrates provide strong and broadband scattering of light and can be useful for application in thin-film solar cells. In particular, we characterize the transmitted light in terms of Haze and Angle-Resolved Scattering, and we compare our results with those obtained for the commonly employed Asahi-U texture. The results indicate that the novel substrate has better scattering properties compared to reference Asahi-U substrates. We observe a super-Lambertian light scattering behavior in selected spectral and angular regions due to the peculiar morphology of the nano-textured interface, which combines high aspect ratio pseudo random structures with cumbers a 1-dimensional periodic pattern.

Strongly enhanced light trapping in a two-dimensional silicon nanowire random fractal array,
B. Fazio, P. Artoni, M. A. Iatì, C. D'Andrea, M. J. Lo Faro, S. Del Sorbo, S. Pirotta, P. G. Gucciardi, P. Musumeci, C. S. Vasi, R. Saija, M. Galli, F. Priolo and A. Irrera.
Light: Science & Applications 5 (4): e16062, 2016.
Paper DOI: 10.1038/lsa.2016.62.
Abstract: We report on the unconventional optical properties exhibited by a two-dimensional array of thin Si nanowires arranged in a random fractal geometry and fabricated using an inexpensive, fast and maskless process compatible with Si technology. The structure allows for a high light-trapping efficiency across the entire visible range, attaining total reflectance values as low as 0.1% when the wavelength in the medium matches the length scale of maximum heterogeneity in the system. We show that the random fractal structure of our nanowire array is responsible for a strong in-plane multiple scattering,

which is related to the material refractive index fluctuations and leads to a greatly enhanced Raman scattering and a bright photoluminescence. These strong emissions are correlated on all length scales according to the refractive index fluctuations. The relevance and the perspectives of the reported results are discussed as promising for Si-based photovoltaic and photonic applications.

Engineered substrates for thin-film solar cells: scattering properties of 1D roughness,
S. Del Sorbo, P. Kowalczewski, S. Pirotta, M. Galli, L.C. Andreani, C. Mennucci, C. Martella, M.Giordano, F. Buatier de Mongeot, L.V. Mercaldo, P. Delli Veneri,
Proceeding of 29th European Photovoltaic Solar Energy Conference and Exhibition, 1BV.6.24, p. 123 – 126,
ISBN: 3-936338-34-5; Paper DOI: 10.4229/EUPVSEC20142014-1BV.6.24.
Abstract: The key advantage of a thin absorbing layer in solar cells is related to reduced electrical transport losses. Yet, decreasing the absorber thickness significantly reduces absorption of sunlight. In this regard, engineering the geometry of substrate allows one to trap the light within a physically thin layer and to maximize the absorption. In this work, we experimentally investigate the scattering properties of one-dimensional rough substrates that provide strong and broad-band absorption enhancement. We demonstrate that these substrates have superior scattering properties with respect to the commonly used Asahi-U textures. In particular, we focus on Angular Resolved Scattering (ARS) and haze of the light transmitted through the rough texture.

Other publications of mine:

Graphene/Silicon Heterojunction for Photovoltaic Applications,
L. Lancellotti, E. Bobeico, A. Capasso, M. Della Noce, P. Delli Veneri, S. Del Sorbo, T. Dikonimos, G. Di Francia, N. Lisi, A. Mittiga, T. Polichetti, F. Ricciardella,
Proceeding of 28th European Photovoltaic Solar Energy Conference and Exhibition, 1AV.2.31, p. 340 – 343
ISBN: 3-936338-33-7; Paper DOI: 10.4229/28thEUPVSEC2013-1AV.2.31.

Acknowledgements

I think back to the last four years of my life, spent as PhD student in Photonics and Nanostructures group at the Physics Department of University of Pavia, and I must thank some of met persons.

Above all, I wish to express my gratitude to Prof Lucio Claudio Andreani and Prof Matteo Galli for supervising me and stimulate my professional growth during this first stage of scientific career.

Also, I am grateful to Prof Francesco Buatier de Mongeot from the University of Genova and Dr Barbara Fazio from CNR in Messina, and to their colleagues, for the fruitful collaboration, which allowed to achieve the results discussed in this thesis.

I acknowledge the useful comments and suggestions of Prof Isodiana Crupi from the University of Palermo and Dr Kevin Vynck from the University of Bordeaux in improving my thesis. I thank them for accepting to be my referee.

I thank Dr Sthy Warren Flores Daorta and Dr Angelo Bozzola for introducing fluorescent solar concentrators to me. I am particularly grateful to Dr Stefano Pirotta, who was optical-bench mate and introduced the town to me.

Finally, I warmly thank all the other peoples of our Department, whom I got in touch. Among these, I wish to remember Matteo, Daniele, Angelica, Saeid, Filippo, Giulia, Francesco, Piotr, Davide and Lee for their friendship with me.

This work was funded by MIUR (the Italian ministry for research, university and education).